

Poroelastic Modelling of Wavefields in Heterogeneous Media

Poroelastische Modellierung von Wellenfeldern in Heterogenen Medien

Zur Erlangung des akademischen Grades eines
DOKTORS DER NATURWISSENSCHAFTEN
von der Fakultät für Physik der Universität (TH)
Karlsruhe

genehmigte

DISSERTATION

von

Dipl.-Ing. Fabian Wenzlau
aus Berlin

Tag der mündlichen Prüfung:	6. Februar 2009
Referent:	Prof. Dr. Friedemann Wenzel
Korreferent:	Prof. Dr. Serge A. Shapiro

Universität Karlsruhe (TH)
Geophysikalisches Institut
Kaiserstraße 12
76128 Karlsruhe
Germany

Abstract

Numerical modelling of seismic waves in heterogeneous, porous reservoir rocks is an important tool for the interpretation of seismic surveys in reservoir engineering. Computer simulations allow the assessment of seismic scattering estimates in heterogeneous environments as well as acoustic attenuation caused by wave-induced flow of pore fluids. Furthermore, there are various theoretical studies that derive effective elastic moduli and seismic attributes from complex rock properties, involving patchy saturation and fractured media. In order to confirm and further develop rock physics theories for reservoir rocks, accurate numerical modelling tools are required.

In this thesis, a 2-D velocity-stress finite-differences (FD) scheme is presented that allows to simulate waves within poroelastic media as described by Biot theory. The scheme is second-order in time, contains higher-order spatial derivative operators and is parallelised using the domain decomposition technique. Numerical stability and dispersion relations of explicit poroelastic FD methods are reviewed and these relations are exemplified by a series of numerical tests that are compared to exact analytical solutions. The focus of several numerical applications is on accurate modelling of scattering and wave-induced flow in the vicinity of mesoscopic heterogeneities such as cracks and gas inclusions. In order to extract seismic attenuation and dispersion from quasistatic experiments, the FD experiments are complemented by numerical experiments based on the finite-element method.

The results confirm that finite-difference and finite-element modelling are valuable tools to simulate wave propagation and coupled diffusion in heterogeneous poroelastic media, provided that the temporal and spatial scales not only of the propagating waves but also of the induced fluid diffusion processes are resolved properly.

Zusammenfassung

Die numerische Modellierung von seismischen Wellen in porösen Reservoirgesteinen ist ein wichtiges Werkzeug für die Interpretation von seismischen Daten und von gesteinsphysikalischen Labormessungen. Mit Hilfe von Computerberechnungen lassen sich für komplexe, heterogene Gesteine die seismische Streudämpfung ebenso ermitteln wie Abschätzungen der akustischen Dämpfung infolge von welleninduzierten Fluidbewegungen. Zudem gibt es eine Vielzahl an theoretischen Modellen, die effektive elastische Eigenschaften und seismische Attribute heterogener Gesteine quantifizieren, beispielsweise im Falle von teilsaturierten oder geklüfteten Medien. Um theoretischen Modelle zu überprüfen, weiterzuentwickeln und um die Grenzen ihrer Anwendbarkeit zu untersuchen, sind genaue Computermodelle notwendig.

Ziel und Motivation dieser Arbeit ist es, einen Überblick zu geben über theoretische, gesteinsphysikalische Modelle, die die Wellenausbreitung in porösen Medien beschreiben. Zudem wird ein neues 2-D Finite-Differenzen-Verfahren (FD) entwickelt, das die Simulation der Wellenausbreitung in poroelastischen Medien ermöglicht. Dem Verfahren liegt die Biot-Theorie zu Grunde, die neben der Wellenausbreitung auch quasistatische Konsolidierungsprozesse beschreibt. Diese stehen in engem Zusammenhang mit der Dispersion und Dämpfung seismischer Wellen infolge von mesoskopischen Prozessen an internen Heterogenitäten, etwa Klüften oder Gaseinschlüssen. Für solche quasistatischen Prozesse werden die FD Berechnungen durch numerische Experimente ergänzt, die auf der Methode der Finiten Elemente (FE) basieren.

Einleitung

Reservoirgesteine sind poröse Medien, die aus einem Korngerüst mit fluidgefüllten Porenräumen bestehen. Ihre gesteinsphysikalischen Eigenschaften ergeben sich folglich aus der Eigenschaften des Porenfluides und der Gesteinskörner, sowie deren Anordnung auf Porenskala. Diese sogenannte Mikrostruktur wird üblicherweise mit Hilfe von petrologischen Parameter wie der Porosität ϕ , der Permeabilität κ oder der Porenraumtortuosität ν charakterisiert. Neben mikroskaligen Hetero-

genitäten weisen Gesteinsformationen jedoch auch großräumige Strukturen auf, die etwa als Schichtgrenzen in seismischen Messungen sichtbar werden. Strukturen, die von seismischen Wellen aufgelöst werden, bezeichnet man als makroskalig. Eine dritte Skala, die Mesoskala, umfasst hingegen all jene Strukturen, die zwar kleiner sind als die seismische Wellenlänge, jedoch deutlich größer als die Porenraumskala. Der Umstand, dass verschiedene geophysikalische Effekte auf allen beschriebenen Skalen stattfinden, erklärt die Komplexität des Materialverhaltens von Reservoirgesteinen.

Für die Dispersion und Dämpfung seismischer Wellen im Frequenzbereich von 10 bis 100Hz sind besonders die Wellenstreuung an Mediumsheterogenitäten relevant, sowie mikro- und mesoskopische Porenfluidströmungen, welche durch die einfallenden Wellen induziert werden können. Letztere führen durch viskose Reibung zwischen Porenfluid und Korngerüst zur Energiedissipation und damit zu einer charakteristischen Wellendämpfung, die in Feldmessungen beobachtbar ist.

Bei akustischen Labormessungen im Ultraschallbereich ($>20\text{kHz}$) bestimmen neben der viskosen Reibung auch Trägheitseffekte die Porenfluidströmungen, so dass in porösen Medien neben den für elastischen Materialien bekannten Kompressions- und Scherwellen eine zweite, langsame Kompressionswelle auftreten kann. Diese von Biot (1956a) theoretisch vorausgesagte langsame Wellenmode wurde von Plona (1980) anhand von Ultraschallmessungen in einem künstlichen porösen Material hoher Porosität experimentell bestätigt. Aktuellere Forschung im Bereich der experimentellen Gesteinsphysik widmet sich zunehmend der Quantifizierung von mesoskopischen Effekten, wobei neben Ultraschallmessungen auch bildgebende Verfahren der Computertomografie Anwendung finden. Dabei motivieren die immer detaillierteren Laborergebnisse neben der Weiterentwicklung von theoretischen Erklärungsmodellen auch den stärkeren Einsatz numerischer Verfahren zur Simulation und Interpretation der im Labor gemessenen Daten.

Mathematische Modelle der Wellenausbreitung in porösen Medien

Die erste vollständige Theorie der dynamischen Poroelastizität wurde von Maurice Biot (1956a,b) entwickelt. Sie beschreibt die Wellenausbreitung elastischer Wellen in porösen Medien in der Form von zwei gekoppelten Wellengleichungen

$$\begin{aligned}\rho^b \ddot{\mathbf{u}} + \rho^f \ddot{\mathbf{w}} &= \nabla[(\lambda_u + \mu) \nabla \cdot \mathbf{u} + \alpha M \nabla \cdot \mathbf{w}] + \mu \nabla^2 \mathbf{u}, & (1) \\ \rho^f \ddot{\mathbf{u}} + Y * \dot{\mathbf{w}} &= \nabla[\alpha M \nabla \cdot \mathbf{u} + M \nabla \cdot \mathbf{w}] & (2)\end{aligned}$$

für die zwei Verschiebungsfelder \mathbf{u} und \mathbf{w} . Hierbei bezeichnen ρ^b und ρ^f die Gesamt- bzw. die Fluiddichte, λ_u , μ , α und M sind poroelastische Materialpa-

parameter. Reibungseffekte zwischen Fluid und Matrix werden durch den viskodynamischen Operator Y erfasst. Fundamentallösungen der Biot-Gleichungen sind drei ebene Wellenmoden, von denen zwei den aus der Elastomechanik bekannten Kompressions- und Scherwellen entsprechen. In porösen Medien sind diese Wellen leicht dispersiv mit einer charakteristischen Übergangsfrequenz ω_B , der Biot-Frequenz. Diese liegt typischerweise im Bereich von 100kHz bis 1MHz, so dass der Dispersionseffekt bei seismischen Messungen nicht in Erscheinung tritt.

Die dritte Wellenmode, langsame Kompressionswelle oder P_{II} -Welle genannt, ist im seismischen Frequenzbereich sehr stark gedämpft und verhält sich praktisch rein diffusiv. Mithilfe der quasistatischen Approximation lässt sich die langsame P -Welle daher näherungsweise als Diffusionswelle beschreiben. Erst bei hohen Frequenzen im Bereich der Biot-Frequenz zeigt sie den Charakter einer propagierenden Welle.

Obwohl das Verhalten homogener poroelastischer Medien gut verstanden ist, ist der Einfluss von Heterogenitäten auf das effektive Materialverhalten aktuell Gegenstand intensiver gesteinsphysikalischer Forschung. Dabei besteht ein besonderes Interesse an der mechanischen Beschreibung teilsaturierter und/oder geklüfteter Gesteine. Zu den klassischen Ansätzen zählt z. B. das Modell von White et al. (1975), mit dem der Einfluss von Gasinklusionen definierter Geometrie (Kugel, Schicht) auf die Dispersion und Dämpfung von seismischen Wellen beschrieben wird. In neueren Modellen wird hingegen die Heterogenität des Medium nicht durch eine bestimmte Geometrie charakterisiert, sondern durch eine statistische Verteilungsfunktion der Materialparameter (Gurevich and Lopatnikov, 1995; Müller and Gurevich, 2005a). Die effektive Wellenzahl des heterogenen Mediums wird dabei durch die Methode der statistischen Glättung (engl. *method of statistical smoothing*) der zufallsverteilten Materialparameter gewonnen.

Ein neuer Aspekt, der in dieser Arbeit behandelt wird, ist die Anwendung zufallsbasierter Modelle auf den Fall der von Kármán Verteilungsfunktion. Mit dem Modell lassen sich teilsaturierte Medien beschreiben, deren Fluidphasen fraktal verteilt sind.

Numerische Methoden

Falls ein poroelastisches Problem analytisch nicht lösbar ist, so kann mit Hilfe numerischer Verfahren eine Näherungslösung bestimmt werden. Im Kontext dieser Arbeit werden zwei Verfahren verwendet: das Finite-Differenzen-Verfahren zur Lösung der dynamischen Biot-Gleichungen sowie die Methode der Finiten Elemente für rein quasistatische Fragestellungen. Der Schwerpunkt liegt dabei auf dem FD Verfahren, da es im Rahmen dieser Arbeit entwickelt wurde, während für die FE Berechnungen das kommerzielle Softwarepaket Abaqus verwendet wird.

Zur Entwicklung des FD Verfahrens werden zunächst die gekoppelten Wellengleichungen 1 und 2 in Form von vier Entwicklungsgleichungen erster Ordnung formuliert, wobei die verwendeten Feldgrößen die Partikelgeschwindigkeit des porösen Mediums, die Filtrationsgeschwindigkeit des Porenfluides, der Gesamtspannungstensor sowie der Porendruck sind. Die zeitliche Diskretisierung erfolgt durch das Ersetzen der zeitlichen Ableitungsoperatoren durch zentrale finite Differenzen. Durch zeitliche Staffelung der Diskretisierung von Geschwindigkeiten und Spannungen wird ein Verfahrensfehler zweiter Ordnung erreicht. Analog zur zeitlichen Diskretisierung erfolgt auch die räumliche Diskretisierung mit Hilfe zentraler FD-Operatoren. Dabei kommen räumliche Operatoren höherer Ordnung zum Einsatz, wahlweise in klassischer Form oder auf einem gedrehten Gitter (Saenger et al., 2000). Da ein expliziter Zeitschrittoperator verwendet wird, liefert das poroelastischen FD-Verfahren nur unter der Bedingung eines ausreichend kleinen Zeitschrittes stabile Ergebnisse, wobei die Stabilitätseigenschaften vergleichbar sind mit denen konventioneller Verfahren für elastische Wellenausbreitung. Allerdings muss, um stabile Ergebnisse zu erhalten, als zusätzliche Bedingung $\nu/\phi > \rho^f/\rho^b$ gewährleistet sein. Für die Berechnung großer Modelle ist es schließlich vorteilhaft, das FD-Verfahren parallel auf einem Großrechner durchzuführen, was durch die Technik der Gebietszerlegung (engl. *domain decomposition*) erreicht wird.

In einem zweiten Abschnitt dieses Kapitels über numerische Methoden wird eine Übersicht über die Methode der Finiten Elemente für poroelastische Fragestellungen gegeben. Im Unterschied zum FD-Verfahren werden hierfür nicht die Differenzialoperatoren diskretisiert sondern der zu Grunde liegende Lösungsraum. Dieser wird bei der FE Methode durch Polynom-Ansatzfunktionen mit örtlich begrenztem Träger dargestellt. Durch Multiplikation mit den Ansatzfunktionen und Integration über den Lösungsraum gehen die Grundgleichungen in ein lineares algebraisches System über, das mit Hilfe eines Gradientenabstiegsverfahren gelöst wird. Zu beachten ist, dass die Implementation des Abaqus FE Programms lediglich die quasistatischen Biot-Gleichungen löst und somit dynamische Effekte wie Wellenausbreitung nicht modelliert werden können.

Genauigkeits- und Skalierungstests

Ein entscheidender Aspekt bei der Berechnung der Wellenausbreitung mit dem FD-Verfahren ist die Genauigkeit der numerischen Näherungslösung. Durch den Vergleich von numerischen Ergebnissen mit exakten, analytischen Lösungen kann die Genauigkeit des FD-Verfahrens untersucht werden, was Gegenstand dieses Kapitels ist.

Ebenso wie bei Modellierung elastischer Wellen ist es im poroelastischen Fall

notwendig, die Wellenlängen zeitlich und räumlich ausreichend genau aufzulösen, um den numerische Dispersionsfehler zu begrenzen. Dabei ist die langsamste Wellenmode entscheidend, d. h. es muss die Diffusionswellenlänge aufgelöst werden, um genaue Ergebnisse zu erzielen. Der Umstand, dass bei Frequenzen weit unterhalb der Biot-Frequenz die Skala des Diffusionsprozesses weitaus kleiner ist als die Wellenlänge der schnellen Kompressionswelle, wird als numerische Steifigkeit (engl. *numerical stiffness*) bezeichnet. Diese führt insbesondere bei der Berechnung von poroelastischen Wellen im seismischen Frequenzbereich zu erheblichem Rechenaufwand, was anhand des Beispiels einer Reflektion von einer poroelastischen Grenzfläche gezeigt wird.

Ferner behandelt dieses Kapitel auch die konsistente Modellierung von freien Fluiden im Rahmen der Poroelastizitätstheorie sowie einen Test zur Bestimmung der Skalierbarkeit des parallelen Codes. Dabei stellt sich heraus, dass die Effizienz des Programms mit steigender Anzahl von bearbeitenden Prozessen abnimmt, jedoch bei 64 parallelen Prozessen noch 91% der Effizienz eines seriellen Prozesses erreicht wird.

Anwendungen

Ziel dieses Kapitels ist es, anhand numerischer Beispiele zu zeigen, wie poroelastische Modellierung einen Beitrag zur Lösung aktueller gesteinsphysikalischer Forschung leisten kann. Beginnend mit FD-Experimenten der Wellenstreuung an einfachen poroelastischen Inklusionen lässt sich die unterschiedliche Wellenkonversion an internen Grenzflächen veranschaulichen. Es werden Ergebnisse gezeigt für ein teilsaturiertes Medium sowie für einen elliptischen Riss. Wenn die Wellenlänge sehr groß ist im Verhältnis zur untersuchten Inklusion, findet hauptsächlich Konversion von schnellen Wellen zur langsamen Diffusionswelle statt, so dass das Gesamtverhalten mit der quasistatischen Approximation beschrieben werden kann. Dies ermöglicht die Verwendung der FE-Methode zur Durchführung von quasistatischen Relaxationsexperimenten, mittels derer effektive Materialeigenschaften eines heterogenen, poroelastischen Mediums bestimmt werden können. Falls die Geometrie des untersuchten Modells effektiv vertikal transversale Isotropie (VTI) aufweist, genügen drei Experimente, um den vollständigen Tensor der Relaxationsrate zu bestimmen. Durch Fouriertransformation erhält man ferner den komplexen, frequenzabhängigen Elastizitätstensor, aus dem sich Dispersion und Dämpfung aller VTI-Wellenmoden berechnet lassen. Numerische Lösungen werden für ein geschichtetes Medium gewonnen sowie für ein 3-D Medium mit einer elliptischen Inklusion.

In zufallsverteilten Medien mit makroskopischen Heterogenitäten findet bei Wellen im seismischen Frequenzbereich hauptsächlich elastische Streuung statt.

Eine Möglichkeit, diese numerisch zu quantifizieren, bieten elastische FD Propagationsexperimente. Zu diesem Zweck wird die relative Amplitudenänderung einer ebenen Kompressionswelle entlang ihres Laufweges durch ein zufallsverteiltes Medium statistisch ausgewertet. Die elastische Streudämpfung ist dabei proportional zur Varianz dieser Amplitudenänderung. Konkret wird anhand einer Serie von numerischen Experimenten ein anisotrop korreliertes Medium in Abhängigkeit des Welleneinfallswinkels untersucht. Die Ergebnisse werden anschließend interpretiert auf der Grundlage von analytischen Abschätzungen der elastischen Streudämpfung.

Im Unterschied zur rein elastischen Streuung gibt es in zufallsverteilten poroelastischen Medien die Möglichkeit, dass in Abhängigkeit vom Frequenzbereich, quasistatische Dämpfung infolge welleninduzierter Fluidströmungen stattfindet in Kombination mit poroelastischer Streuung. Dieser Übergang wird anhand eines teilsaturierten Mediums untersucht, wobei die Fluidphasen zufallsverteilt sind und einer fraktalen Verteilungsfunktion unterliegen. Abschließend zeigt ein Beispiel die erfolgreiche Anwendung des FD-Verfahrens zur Simulation einer im Labor durchgeführten Ultraschallmessung an einem teilsaturierten Sandstein.

Schlussfolgerungen und Ausblick

Wellenstreuung und durch Wellen induzierte Porenfluidströmungen sind zwei Hauptursachen für seismische Dämpfung in geologischen Reservoiren. In dieser Arbeit wird ein Überblick gegeben über die mathematischen Modelle zur Beschreibung der genannten Effekte auf die Wellenausbreitung in porösen Gesteinen, wobei insbesondere auch ein neuer Ansatz vorgestellt wird, mit Hilfe dessen welleninduzierte Strömungen in zufallsverteilten Fraktalen quantifiziert werden.

Das Hauptergebnis der vorliegenden Arbeit umfasst die Entwicklung, Implementierung und Validierung eines neuen Finite-Differenzen-Verfahrens zur Lösung der dynamischen Biot-Gleichungen. Das Verfahren erlaubt die Simulation der Wellenausbreitung in heterogenen, poroelastischen Strukturen in einem breiten Frequenzbereich. Da die dynamischen Biot-Gleichungen bei niedrigen Frequenzen eine hohe numerische Steifigkeit aufweisen, ergibt sich für die Simulation seismischer Wellen ein hoher Diskretisierungsaufwand, um gleichzeitig makroskopisch propagierende Wellen und kleinskalige Diffusionsprozesse aufzulösen. Zur Untersuchung mesoskopischer Prozesse ist es daher vorteilhaft, einen quasistatischen Finite-Elemente-Löser zu verwenden.

Anhand mehrerer Anwendungsbeispiele wird gezeigt, dass poroelastische Modellierung einen wertvollen Beitrag leisten kann zur Untersuchung von Wellenausbreitung und gekoppelten Diffusionsprozessen in heterogenen, poroelastischen Medien.

Danksagungen

Ich danke Prof. Friedemann Wenzel für seine Bereitschaft, diese Arbeit als Hauptreferent zu begleiten und Prof. Serge Shapiro für die Übernahme des Korreferats. Für die ausgezeichnete Betreuung gilt zudem mein besonderer Dank Tobias Müller, der mir während der gesamten drei Jahre am GPI stets mit motivierendem Interesse und vielen Hinweisen hilfreich zur Seite gestanden hat.

Für eine gute Zusammenarbeit und Gedankenaustausch während zahlreicher Kaffeepausen bin ich all meinen Kollegen sehr verbunden, in besonderer Weise Johannes, Markus, Nico, Tian, Tatiana sowie Gerardo und Miro.

Schließlich möchte ich auch Sophie danken, die mit liebevoller Unterstützung und ermutigenden Worten sehr zum Gelingen dieser Arbeit beigetragen hat.

Contents

<i>List of Figures</i>	xii
<i>List of Tables</i>	xiii
<i>Nomenclature</i>	xv
1 Introduction	1
1.1 Scales in porous media	2
1.2 Seismic attenuation in fluid-saturated rocks	4
1.3 Experimental laboratory results	9
1.4 Motivation and overview of this thesis	12
2 Mathematical models for wave propagation in porous media	15
2.1 Notation	16
2.2 Momentum equations	18
2.3 Constitutive relations	19
2.4 Plane wave solutions	22
2.5 Boundary conditions	24
2.6 Quasistatic behaviour of porous media	26
2.7 Heterogeneous porous media	29
2.8 Wave-induced fluid flow	32
2.8.1 White’s model for partial saturation	33
2.8.2 Continuous random media models	35
2.9 Discussion	38
3 Numerical methods	41
3.1 Modelling poroelastic wave propagation using the FD method	42
3.1.1 Time discretisation	43
3.1.2 Calculation of spatial derivatives	45
3.1.3 Boundaries and sources	48
3.1.4 Stability	49
3.1.5 Accuracy	51
3.1.6 Parallelisation	52
3.2 Modelling quasistatic consolidation using the FE method	53
3.2.1 Spatial discretisation by the Galerkin method	54

3.2.2	Boundaries and sources	56
3.2.3	Time integration and solution of the linear system	56
3.3	Discussion	57
4	Accuracy and scalability tests	59
4.1	Numerical dispersion	59
4.2	Intertial and diffusive regimes	60
4.3	Resolution of the diffusion boundary layer	62
4.4	Modelling free fluids	64
4.5	Parallel performance	66
4.6	Discussion	67
5	Applications	69
5.1	Scattering from porous inclusions	70
5.2	Quasistatic relaxation experiments	73
5.3	Elastic scattering in random media	81
5.4	Wave-induced flow in random media	88
5.5	Simulation of ultrasonic laboratory experiments	96
5.6	Discussion	98
6	Conclusions and outlook	101
A	Viscoelasticity and quality factor	105
B	Statistical characterisation of random media	109
C	Supplementary rock physics formulas	113
C.1	High frequency correction for the Biot equations	113
C.2	Poroelastic Backus average	114
C.3	Extended theory of wave-induced flow in layered porous media	117
C.4	White's model for partial saturation	118
C.5	Complement on the random fractal media model	120
D	Abaqus porous elastic model	123
	<i>Bibliography</i>	127
	<i>Author index</i>	136
	<i>Subject index</i>	138

List of Figures

1.1	Pore spaces of four different natural carbonate rocks.	2
1.2	Scales of reservoir characterisation.	3
1.3	Classification of different attenuation mechanisms.	4
1.4	Intrinsic P -wave attenuation $1/Q$ of rocks at one test site.	5
1.5	Characteristic frequencies of five relaxation mechanisms	7
1.6	Classification of scattering phenomena.	8
1.7	Sketch of Plona's experimental setup.	10
1.8	Seismograms proving the existence the slow P -wave mode.	10
1.9	Attenuation measurements in partially saturated sandstone.	11
1.10	Computer tomography scans of limestone during gas injection.	12
1.11	Ultrasonic velocities in a partially saturated rock sample.	13
2.1	Overview of theoretical descriptions of porous media	16
2.2	Sketches of three deformation experiments	21
2.3	Biot theory: dispersion and attenuation	24
2.4	Biot theory: quasistatic pore pressure response	28
2.5	Biot theory: quasistatic dispersion and attenuation	29
2.6	Gassmann-Hill and Gassmann-Wood bounds	31
2.7	Propagation velocities in an effectively anisotropic porous medium	32
2.8	Comparison of three theories of partial saturation	35
2.9	Realisations of random media and correlation functions.	37
2.10	Continuous random media model for partial saturation	38
3.1	Finite-difference operators and their amplitude spectra	47
3.2	Stencils of standard and rotated FD operators.	47
3.3	Examples of boundary conditions for poroelastic wave simulation.	49
3.4	Domain of stability, limited by two conditions.	51
3.5	System eigenvalues of fast and slow P -waves.	52
3.6	Sketch of the parallelisation by domain decomposition.	53
3.7	Example of a finite-element mesh.	54
3.8	Linear basis functions for a triangular element.	55
4.1	Numerical dispersion in a 2-D frictionless, porous medium.	60

4.2	Synthetic velocity and pore pressure seismograms.	61
4.3	Pore pressure profiles for a “step” loading at $x = 0$	62
4.4	Frequency-dependent reflection from a gas-water contact.	63
4.5	Frequency-dependent reflection from a fluid-porous interface.	65
4.6	Seismograms of wave scattering from a fluid-porous interface	66
4.7	Scalability test of the poroelastic FD scheme.	68
5.1	Scattering of a plane compressional wave from an elliptic crack.	71
5.2	Same as figure 5.1, but for a circular gas inclusion.	72
5.3	Dispersion, attenuation in patchy-saturated rock (1-D model).	75
5.4	Three deformation states used to obtain all 5 effective moduli.	76
5.5	Two model geometries for double porosity relaxation experiments.	77
5.6	Attenuation derived from double porosity relaxation experiments.	78
5.7	Relaxation functions obtained from double porosity experiments.	79
5.8	Maximum wave attenuation as a function of incidence angle.	80
5.9	Backscattering and random diffraction in 1-D and 2-D media.	82
5.10	Velocity models used for numerical scattering experiments.	84
5.11	Synthetic seismograms of scattered plane compressional waves.	84
5.12	Amplitude spectra of scattered wavefields in isotropic media.	85
5.13	Log-amplitude variance of different angles of incidence ϕ	86
5.14	Log-amplitude variance for large propagation distances.	87
5.15	Synthetic saturation maps with fractal pore fluid distributions.	89
5.16	Pore pressure snapshots of wave propagation in the BRM model.	90
5.17	Same as 5.16 but for the CRM model. (Clipping also as in 5.16)	90
5.18	Quasistatic pore pressure relaxation in the BRM model.	92
5.19	Same as 5.18 but for the CRM model. (Clipping also as in 5.18)	92
5.20	Dispersion, attenuation in fractal media derived from FD exp.	93
5.21	Same as 5.20 but for the CRM model.	93
5.22	CT images of the Casino Otway Basin sandstone.	96
5.23	Velocity-saturation relation for a rock with partial saturation.	97
5.24	Unrelaxed pore pressure distributions in the 3-D FE model.	100
A.1	Relaxation and creep test for the evaluation of $\tilde{M}(\omega)$	107
B.1	Procedure of creating random media realisations.	111
C.1	Backus averaging and corresponding maximum attenuation.	118
C.2	Values of the Gaussian hypergeometric function ${}_2F_1(a, b; c; x)$	121
C.3	Fractal CRM realisations for different Hurst exponents.	122
C.4	CRM model for partial saturation with fractal geometry.	122
D.1	Stress-strain relation of the Abaqus FE model.	124

D.2	Triangular, quadrangular and tetrahedral linear elements.	125
-----	---	-----

List of Tables

2.1	Typical material properties of sandstone	26
2.2	Material properties of fluids typically found in reservoirs	26
2.3	Overview of rock physics theories for wave-induced fluid flow.	34
3.1	Finite-differences coefficients	46
4.1	Elapsed wall clock time for two sets of test simulations.	67
5.1	Material properties used in the numerical applications.	70
5.2	Petrophysical properties of the dry Casino Otway sandstone	97

Nomenclature

Roman

a	correlation lengthscale in random media	m
b	friction coefficient	Pa s / m ²
c	also v , wave propagation velocity	m/s
c_{ijkl}	(short notation c_{IJ}) elasticity tensor	Pa
f	frequency	Hz
i	imaginary unit $\sqrt{-1}$	
k	wave number	1/m
n_i	normal unit vector	
p	pore pressure	Pa
p^s	confining pressure ($-\sigma_{ii}/3$)	Pa
q_i	filtration velocity	m/s
u_i	total particle displacement	m
v_i	total particle velocity	m/s
w_i	relative displacement (Eq. 2.13)	m
B	correlation function in random media	
C	$= \alpha M$, poroelastic modulus	Pa
D	wave parameter in seismic scattering (Eq. 1.5)	
D	hydraulic diffusivity (Eq. 2.75)	m ² /s
G	shear modulus	Pa
H	$= P_u$, undrained P -wave modulus	Pa
K	bulk modulus	Pa
L	$= P_d$, drained P -wave modulus	Pa
L	characteristic lengthscale of heterogeneous media	m
L	length of wave propagation path	m
M	pore space modulus (Eq. 2.40)	Pa
N	inverse uniaxial storage	Pa
P	P -wave modulus	Pa
Q	quality factor	

Greek

α	attenuation coefficient in viscoelasticity	1/m
α	Biot coefficient of effective stress (Eq. 2.39)	
δ	Dirac distribution (Eq. 2.10)	
δ_{ij}	Kronecker symbol (Eq. 2.9)	
ϵ_{ijk}	Levi-Civita symbol (Eq. 2.8)	
ϵ	volumetric strain (Eq. 2.15)	
ϵ_{ij}	strain tensor (Eq. 2.14)	
ζ	local increment of fluid content (Eq. 2.16)	
η	fluid viscosity	Pa s
κ	hydraulic permeability	m ²
λ	Lamé parameter	Pa
λ	wave length	m
λ_D	diffusion length (Eq. 2.83)	m
μ	Lamé parameter, shear modulus	Pa
ν	tortuosity	
ν	Hurst exponent in van Kármán correlation function	
ρ	mass density	kg/m ³
ρ^m	effective fluid mass density (Eq. 2.23)	kg/m ³
τ_{ij}	stress tensor	Pa
ϕ	porosity	
ϕ	creep function for anelastic materials (see appendix A)	
χ	logarithmic amplitude relation (Eq. 5.26)	
ψ	relaxation function (see appendix A)	
ψ_{ijkl}	relaxation tensor	
ω	circular frequency	1/s
ω_B	Biot frequency (Eq. 2.21)	1/s
ω_c	characteristic frequency of mesoscopic flow (Eq. 2.87)	1/s

Indices / superscripts

b	bulk property
d	drained
eff	effective
f	fluid
g	grain
r	relaxed
u	undrained or unrelaxed, respectively

Operators

$\langle \phi \rangle$	spatial mean of ϕ (Eq. 2.82)	
$\dot{\phi}$	time derivative of quantity ϕ	1/s
$\phi_{i,i}$	divergence of vector field ϕ_i	1/m
$\phi_{i,j}$	gradient of ϕ_i	1/m
$\partial_t \phi$	time differential operator	1/s
$\partial_i \phi$	spatial differential operator	1/m
$D_i \phi$	discrete spatial differential operator	1/m
$\mathcal{F}\{\phi\}$	Fourier transform	
$Y * \phi$	viscodynamic operator	Pa s / m ²

Abbreviations

AVO	Amplitude versus offset
BRM	Binary random medium
CRM	Continuous random medium
CT	X-ray computer tomography
FD	Finite differences
FE	Finite elements
REV	Representative elementary volume
VSP	Vertical seismic profile

Chapter 1

Introduction

Seismic surveys and acoustic borehole measurements are routinely used in the hydrocarbon exploration industry in order to obtain information about subsurface geology. The first aim of seismic processing techniques is to construct images of velocity and reflectivity distributions from recorded elastic wave fields. In a second step, from the seismic data mechanical and petrophysical properties are derived such as rock compressibility, porosity and information about the presence or absence of fluids in the pore space. It is the domain of seismic rock physics to establish physical relationships between these rock properties and the seismic response (Dewar and Pickford, 2001).

In particular, the influence of pore fluids on seismic velocity and attenuation has attracted increasing attention in the past, since wave-induced fluid flow is considered to contribute mainly to measured signatures in porous reservoirs, e. g. an interesting question in current rock physics research is concerned with the estimation of permeability from seismic data. Based on the pioneering work of Maurice A. Biot on wave propagation in porous media in the 1950's, a large number of publications has appeared in the literature dealing with the theoretical and experimental description of porous media acoustics. With the general availability of computers, in the 1990s first attempts were made to solve numerically the equations governing wave propagation and coupled flow processes and this field of numerical rock physics is becoming more and more important for the interpretation of experimental observations and for testing the validity and applicability of new theoretical models.

It is the purpose of this thesis to present a new numerical scheme for solving the dynamically coupled wave equations in porous media and to demonstrate how numerical tools are successfully applied to current problems in rock physics research.

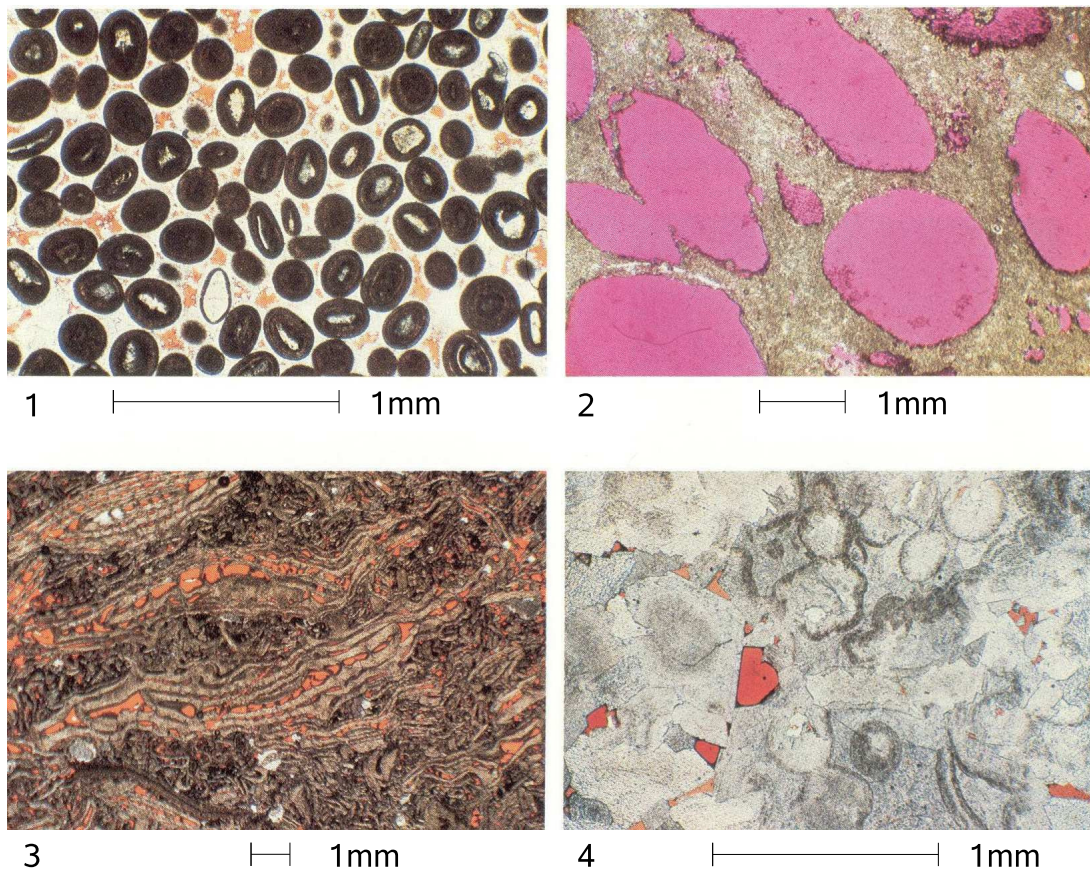


Figure 1.1: Pore spaces of four different natural carbonate rocks. Photographs of thin sections show an oolitic limestone (1), a sample with large pores due to the dissolution of microfossils (2), a nummulite limestone (3) and a totally dolomised oolitic limestone (4). From Bourbié et al. (1987).

1.1 Scales in porous media

Hydrocarbon reservoir rocks such as sandstones, shales and carbonates are porous media with fluids filling the pore space between mineral grains. Physical properties of reservoir rocks are therefore determined by the properties of its constituents and in as much by the distribution of porespace and grain matrix, referred to as the rock microstructure. The sub-millimetre scale microstructure of four limestones is depicted in Figure 1.1, showing the large variability of natural porespace geometries. If for one particular rock, one had all information about the the distribution of the pore space and about the properties of grains and fluid, in principle one could infer the overall mechanical and hydraulic behaviour of the composition (Guéguen and Palciauskas, 1994). Obviously, this information is usually not available in practice and it is convenient to describe microstructure and associate

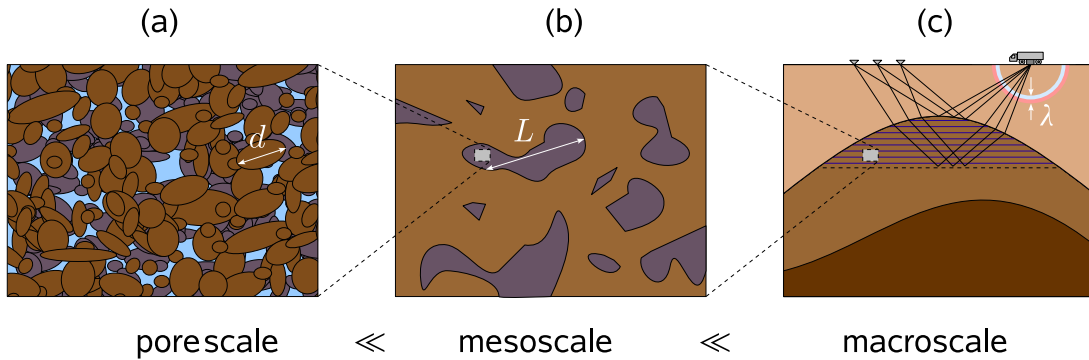


Figure 1.2: Scales of reservoir characterisation ranging from microscopic grain sizes (a) via several centimetres for mesoscale heterogeneities (b) up to seismic wavelengths that are tens of metres (c).

microscale effects using measurable quantities, among the most important are porosity ϕ (the volume fraction of the pore space), hydraulic permeability κ (the ability the conduct fluids) and overall elastic moduli of the rock matrix. Another parameter is the pore space tortuosity ν , describing the ratio of average flow path length inside the pore channels of a given rock sample and the total sample dimension.

Besides the complexity of the porespace, rocks are typically heterogeneous on various scales, as shown in Figure 1.2. The scale that is resolved by seismic waves is that of geological layers and reservoir structures. Typically this so-called macroscale ranges from several centimetres at 10kHz sonic logging frequency up to tens of metres at 100Hz surface seismic records.

Finally, a third intermediate spatial scale can be defined that is due to heterogeneity of the porous medium properties. These so-called mesoscale heterogeneities are smaller than the seismic wavelength but still much larger than the dimensions of the microscopic pore space. Actually rocks always contain to some extent heterogeneity that is not due to the grains and porespace but to other features such as fractures, soft inclusion, embedded thin layers or different fluids distributed on various scales.

It is the multiscale nature of Earth materials that explains their complexity and the high variability of their physical properties. Seismic measurements that are carried out using a particular frequency always contain information about a specific scale. If for example results from sonic logging are interpreted on a larger scale, one has to take into account scaling effects that are simply not included in the measurement. This is done by upscaling techniques. From the modelling point of view, the reasonable and successful application of theoretical models and numerical rock physics tools requires a good understanding of the physical processes on the various scales.

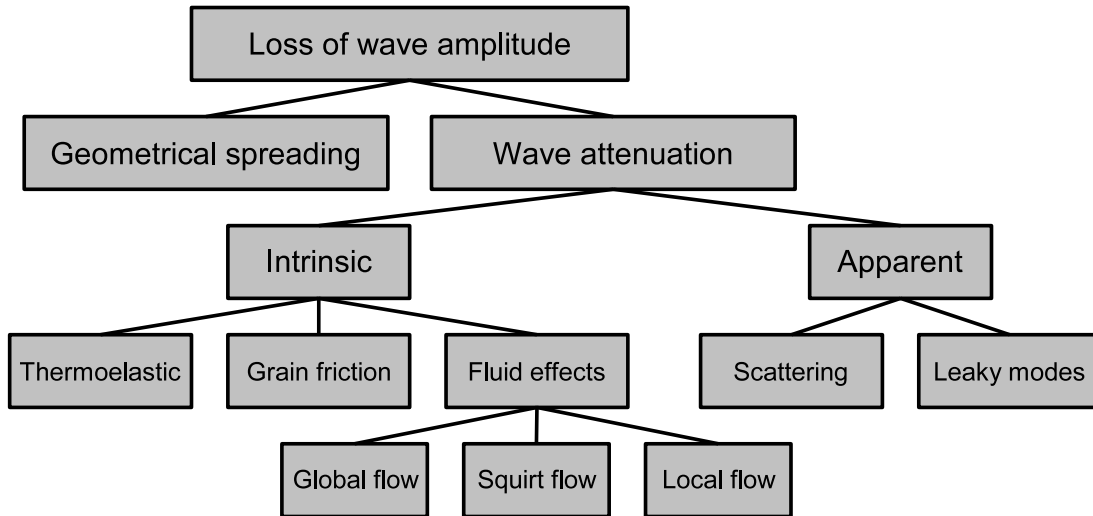


Figure 1.3: Classification of different attenuation mechanisms.

1.2 Seismic attenuation in fluid-saturated rocks

If an initially dry rock sample is fully saturated with water, its compressibility is reduced while shear stiffness is practically not affected. This static effect has been quantified by Fritz Gassmann’s work “On elasticity of porous media” (Gassmann, 1951) and is widely applied for fluid substitution calculations. Another fundamental effect is time-dependent consolidation of geomaterials under a given loading. Terzaghi and Fröhlich (1936) found that the consolidation of clay is governed by a diffusive pore pressure relaxation process. His results were later generalised by Biot (1941) for the three-dimensional case. Biot further developed his theory in order to include wave propagation effects Biot (1956a,b) and brought up the idea that pore pressure relaxation may lead to dispersion and attenuation of seismic waves.

Attenuation denotes all processes leading to a loss in seismic wave amplitude except for geometrical spreading effects. In general, two classes of wave attenuation can be distinguished (see Figure 1.3). On the one hand, intrinsic attenuation is caused by non-elastic energy losses, meaning that a part of the wave energy is transferred to heat by internal friction. Apparent attenuation, on the other hand, occurs when the wave amplitude is reduced by the redistribution of wave-field energy (e. g. due to elastic scattering). It is well-known that the attenuation is a frequency-dependent effect and that it is linked to velocity dispersion by the causality principle. An introduction to viscoelastic material behaviour and to the quantitative description of attenuation is given in appendix A. Figure 1.4 gives an example of a broad frequency-range measurement of seismic intrinsic attenuation at the Imperial College test site, combining ultrasonic core measurements with

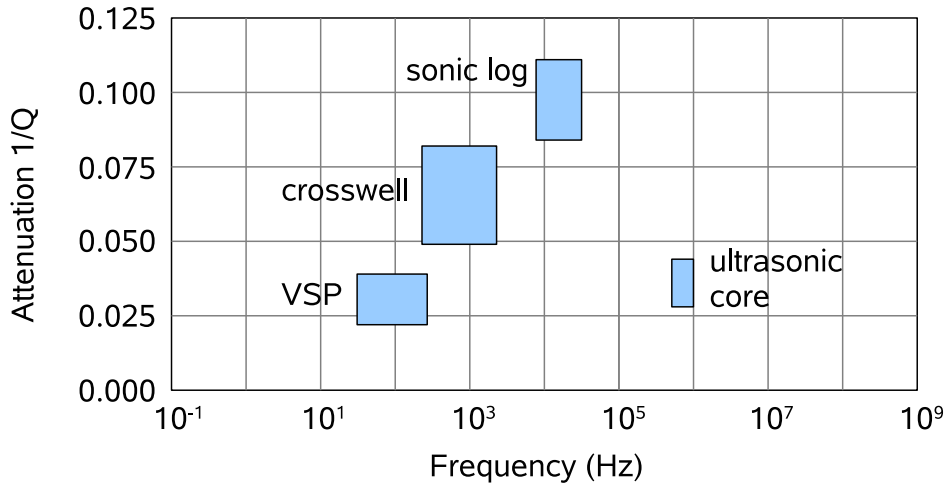


Figure 1.4: Intrinsic P -wave attenuation $1/Q$ as determined by Sams et al. (1997) on rocks at the Imperial College test site at various depths. VSP and sonic log estimates have been corrected for scattering attenuation. After Pride et al. (2003).

sonic logs, crosswell and VSP data (Sams et al., 1997). The measured values of the inverse quality factor $1/Q$ attain 0.1 and higher for the sonic logs and more than 0.02 for all the measurements, thus indicating that on all scales, a significant amount of energy loss is observed. In the following, mechanisms causing attenuation of seismic waves in reservoirs are discussed in more detail.

In a *homogeneous* porous medium, pore pressure differences may appear between the peaks and the troughs of a propagating compressional wave. The relaxation associated with pressure equilibration between these extrema is the global flow mechanism described by Biot (1956a). Since the scale of the Biot global flow is that of the wavelength, it is a macroscopic effect. The characteristic relaxation frequency of the process is given by

$$\omega_B = \frac{\eta \phi}{\kappa \nu \rho^f}, \quad (1.1)$$

where η is the dynamic fluid viscosity, ϕ is porosity, κ the hydraulic permeability, ν the pore space tortuosity and ρ^f the fluid density. Its values are typically of the order of 100 kHz up to the MHz range and therefore, at seismic frequencies (usually much below 1kHz) pore pressure is always unrelaxed with respect to global flow effects and Biot attenuation is negligible. By the way, an analogy exists between the theory of poroelasticity and thermoelasticity, where unrelaxed processes are called adiabatic (Norris, 1992). The Biot frequency ω_B will be discussed later in more detail since it separates two regimes that are characterised

by friction-dominated diffusive fluid flow on the one hand and inertially driven fluid flow on the other hand, see chapter 2.

A second, very efficient attenuation mechanism occurs if a porous medium is *heterogeneous* on mesoscopic scales, i. e. on scales larger than the pore scale but still smaller than the seismic wavelength. In this case, pore pressure differences appear not only on macroscopic scales, but also locally across each internal interface. Therefore, the relaxation may occur due to local flow effects and its characteristic frequency depends explicitly on the scale of the heterogeneity as

$$\omega_c = \frac{\kappa N}{\eta L^2}. \quad (1.2)$$

Here, N is a poroelastic modulus, introduced later in section 2.6 and L is a characteristic spatial scale of the medium heterogeneity. The local flow mechanism is often referred to as wave-induced fluid flow (e. g. Müller and Gurevich, 2005b). It is important to note that while the characteristic frequency ω_B decreases with increasing permeability, the characteristic local flow frequency ω_c shows the opposite behaviour. A second remarkable point is that because of the presence of multiscale heterogeneities in porous rocks, seismic attenuation due to wave-induced flow affect a large frequency range and play a major role at seismic frequencies. In this context, note the spatial scale dependence of equation 1.2. Finally, from a modelling point of view it is important to mention that local flow effects are completely described by the Biot theory.

An attenuation effect that is not included in Biot's description of seismic wave propagation, that is, however, considered to be very efficient is the squirt flow first described by Mavko and Jizba (1991). The squirt flow is very similar to the local flow described above, but it emphasises grain-scale heterogeneities and can therefore be classified as a microscopic effect. Actually, reservoir rocks practically always have microcracks, loose grain contacts or defects that are often subsumed as soft porosity. During wave propagation, the soft pore space is squeezed and since the fluid in the pores is viscous, this leads to energy dissipation and wave attenuation. The frequency-dependence of the squirt flow has been quantified by Dvorkin et al. (1995). In their model, the characteristic frequency depends on microscopic crack scale R and its aperture h such that according to Pride et al. (2003) one can write

$$\omega_{\text{squirt}} = \frac{\beta K_f}{\eta}, \quad (1.3)$$

where K_f denote the fluid bulk modulus and $\beta = (h/R)^2$. Interestingly, ω_{squirt} depends on the fluid viscosity η but not on the permeability κ , unlike in the case of local flow. The reason for this is that squirt relaxation process occurs on lengthscales not exceeding the grain size. The characteristic squirt-flow length

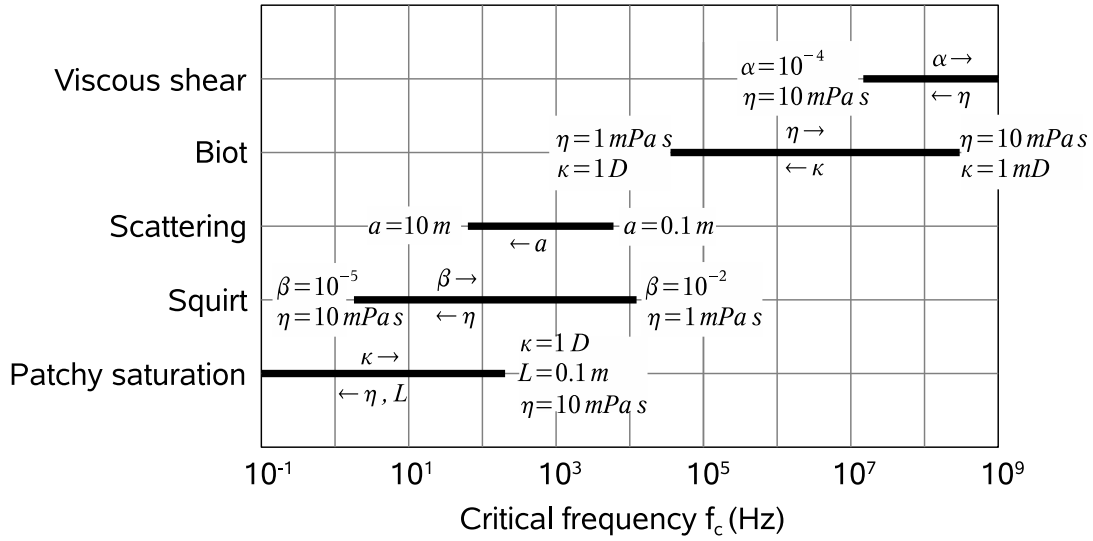


Figure 1.5: Comparison of characteristic relaxation frequencies as predicted by rock physics theories for typical rock and fluid parameters. Arrows show the direction of change as the labeled parameter increases. Adapted from Mavko et al. (1998).

is an additional parameter that is not related to material properties appearing in the theoretical Biot model. In subsequent chapters, the squirt flow effect will not be considered, but the focus will be on global and local flow effects that are directly described by the Biot theory.

Figure 1.5 gives an overview of the frequency ranges on which the previously discussed relaxation processes may occur. As can be seen from this figure, the Biot global flow occurs typically at ultrasonic frequencies, while squirt flow and wave-induced local flow may very well affect the seismic frequency range. Typical frequencies where wave scattering occurs are shown in Figure 1.5, as well. Scattering and the corresponding apparent attenuation is briefly discussed.

In contrast to the aforementioned intrinsic attenuation mechanisms, the scattering of seismic waves in an elastic medium is not based on absorption but on the redistribution of wavefield energy. It is therefore called apparent attenuation. The scattering of seismic waves is most efficient when the seismic wavelength λ approximately equals the characteristic size of the elastic scatterer, a , and the effects of scattering become increasingly important with increasing propagation distance L . According to Aki and Richards (1980), scattering phenomena can be classified using the dimensionless quantities ka and kL , where $k = 2\pi/\lambda$ is the wavenumber. An overview of the different scattering regimes is given in Figure 1.6. If ka is very small, the wavelength is much larger than the scale of the hetero-

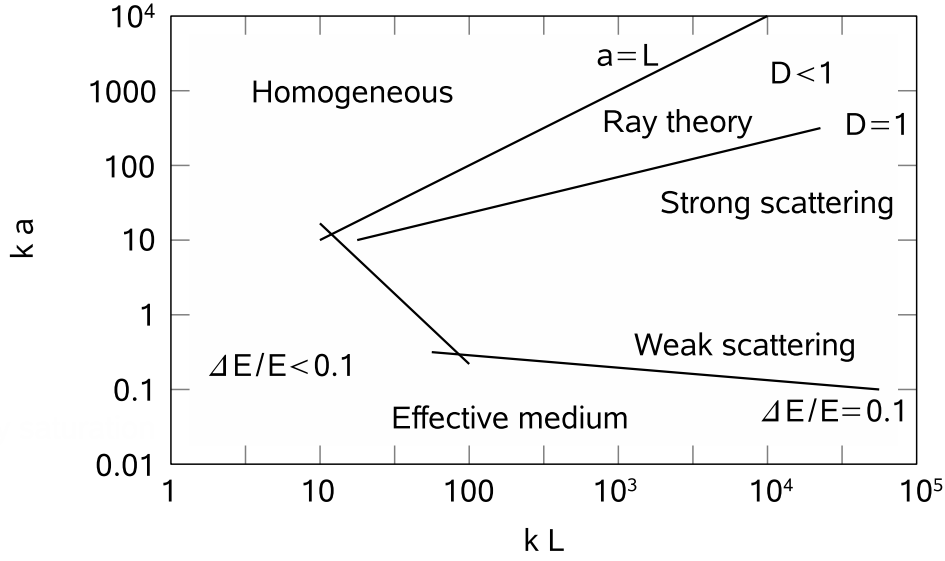


Figure 1.6: Scattering regimes classified by the products of wavenumber k , and characteristic scale a or propagation path L , respectively. From Mavko et al. (1998).

genities and the medium behaves like an effective homogeneous medium where scattering is negligible. The effective medium theory requires that the fractional energy loss $\Delta E/E$ is small, as well. On the other hand, if ka is large, the wave propagates through a piecewise homogeneous medium. A critical frequency for scattering processes is given by $ka = 1$ or alternatively

$$\omega_s = \frac{c}{a} = \frac{\sqrt{H/\rho}}{a}, \quad (1.4)$$

where H is the elastic modulus and ρ the density. The wave parameter D defined as

$$D = \frac{2L}{ka^2} \quad (1.5)$$

is another dimensionless number parameter characterising the scattering regime. It is used as indicator whether diffraction has a significant impact on the scattered wavefield. For $D < 1$ wave diffraction is small and ray theory can be applied for the wavefield description. The diffraction regime $D > 1$ is then furthermore subdivided into the weak and strong scattering regimes, depending on whether forward scattering is dominant (weak) or multiple scattering occurs (strong). Depending on the scattering regime, different theoretical wavefield approximations are available (Wu and Aki, 1988; Sato and Fehler, 1998; O'Doherty and Anstey,

1971; Shapiro and Hubral, 1999; Müller and Shapiro, 2001). A more detailed description of weak wave scattering in random elastic media is given in section 5.3 together with a corresponding numerical experiment.

1.3 Experimental laboratory results

One of the main results of Biot theory is the existence of a second compressional wave mode – the slow P -wave – in porous media. To put it simply, this slow wave mode is associated with an out-of-phase movement of the fluid and the solid phases, while fluid and solid move in phase during fast P -wave propagation. This theoretically predicted wave mode has been first experimentally observed by Plona (1980), who carried out ultrasonic laboratory measurements on a synthetic highly-porous medium consisting of sintered glass beads.

Synthetic samples with 7–28.3% porosity were placed into water and signals were recorded after transmission through the samples (see Figure 1.7). Plona was able to directly identify the slow P -wave, reporting propagation velocities around 1000 m/s. Seismograms of recorded signals for varying angle of incidence θ are shown in Figure 1.8. For normal incidence ($\theta = 0^\circ$, Figure 1.8a), no P -to- S -conversion occurs and only fast and slow P -waves and multiples are recorded. For non-normal incidence, an additional converted S -wave is observed. If the angle of incidence exceeds the critical angles of fast P - and S -waves ($\theta > \theta_c^S$, Figure 1.8d), the seismogram is dominated by the signal of the converted slow P -wave.

In natural rocks, the slow P -wave has not been directly observed due to their low porosity and strong microscale heterogeneities. This leads to a strong attenuation of the slow P -wave and makes its direct detection impossible. There is, however, indirect evidence for the existence of the effects caused by the Biot slow P -wave. It can be shown that at frequencies below the critical Biot frequency ω_B , the slow P -wave describes a diffusion process, that influences the attenuation and dispersion behaviour of porous rocks.

As an example, Figure 1.9 shows attenuation measurements of a partially saturated sandstone (Murphy, 1982). Murphy applied a resonant bar technique to obtain the frequency-dependence of partial saturation. While attenuation of the dry sample is very low, maximum measured P -wave attenuation is as high as $1/Q = 0.1$ for 90-92% water saturation. The attenuation of shear waves is lower and attains 0.075. The saturation-dependence of acoustic attenuation can be explained by the effects of wave-induced local flow as described in the previous section 1.2.

For a better understanding of fluid-related attenuation and other seismic signatures the scales of the underlying process have to be analysed in more detail. Therefore, in recent years, an increasing effort has been made to investigate the

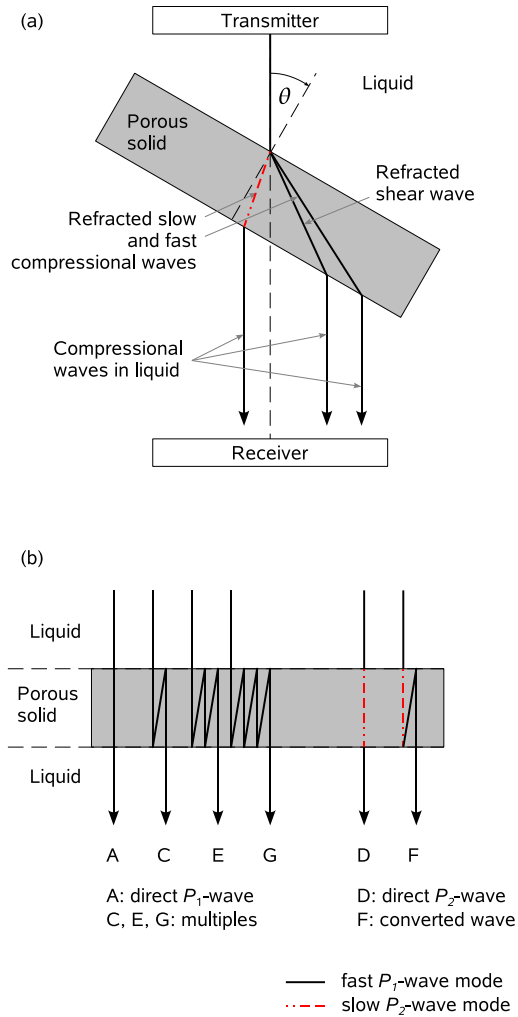


Figure 1.7: Sketch of the experimental setup of Plona. Ultrasonic wave refraction at different interfaces (a) and an overview of compressional wave mode multiples occurring at normal incidence (b). After Bourbié et al. (1987).

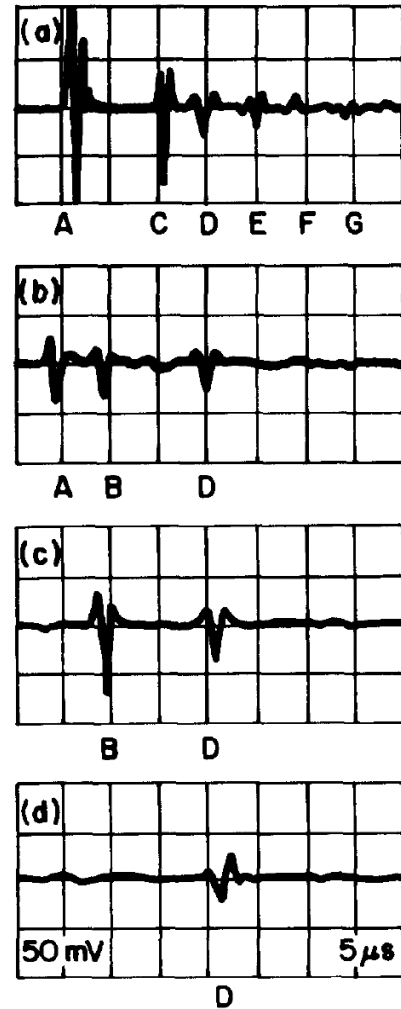


Figure 1.8: Seismograms proving the existence of the second slow compressional wave mode observed by Plona (1980). Signals are recorded at different angles of incidence θ , i. e. at (a) $\theta = 0^\circ$, (b) $0^\circ < \theta < \theta_c^{P1}$, (c) $\theta_c^{P1} < \theta < \theta_c^S$, and (d) $\theta_c^S < \theta < 90^\circ$.

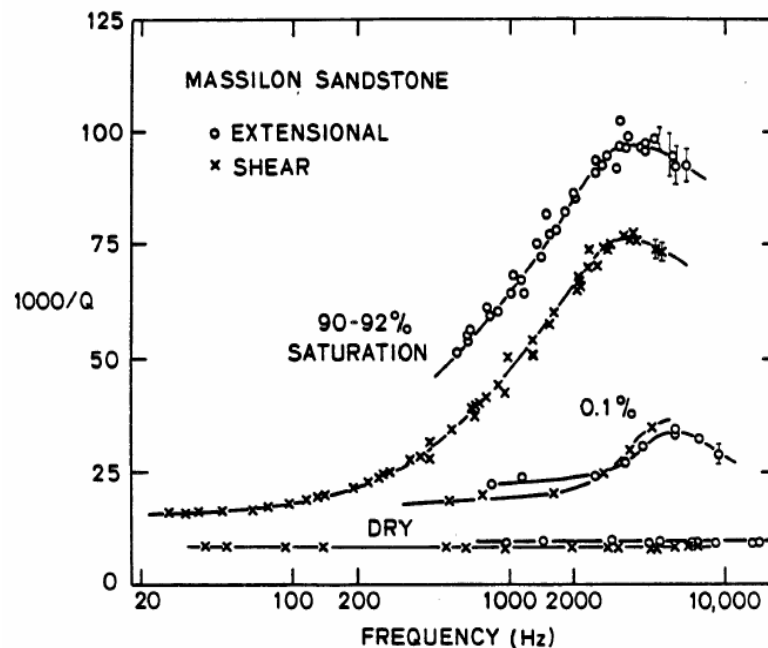


Figure 1.9: Frequency-dependent attenuation measurements in partially saturated sandstone conducted by Murphy (1982).

meso- and microstructure of various rock samples in the laboratory. For that purpose, modern x-ray computer tomography (CT) is applied to estimate porosity and to characterise the pore space geometry down to the micrometre scale (e. g. Klobes et al., 1997). An even higher resolution can be obtained by neutron radiography (de Beer et al., 2004). Commercial CT scanners commonly used in medical radiology have resolutions in the order of millimetre and are not able to resolve the pore space of a porous rock sample. They may be applied instead to characterise mesoscale heterogeneities.

An example of the application of CT scans in rock physics research is given in Figure 1.10. The figures show the development of gas patches within a water-saturated limestone sample during a gas injection experiment. Initially, the sample is fully saturated (upper left subfigure), injection point is in the lower left side of the rock sample. Interestingly, there is no clear gas front visible, but gas and water form a complex patch geometry. Therefore, the scans demonstrate that mesoscopic patchy saturation may occur during fluid replacement. The total sample diameter is 5cm.

A combined investigation of ultrasonic velocities and CT imaging of rock heterogeneity has been recently conducted by Monsen and Johnstad (2005) and earlier also by Cadoret et al. (1995). They found that there is a qualitative link

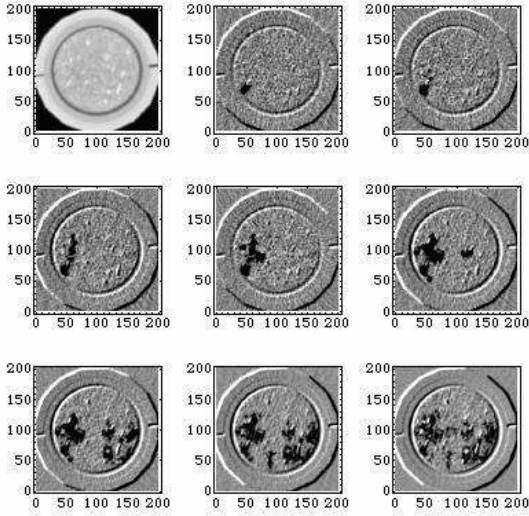


Figure 1.10: Computer tomography scans of an initially fully water-saturated limestone sample during gas injection. The sample diameter is 5cm. The gas forms pockets (indicated by black colour) on a mesoscopic scale. The image scans have a minimum pixel size of 0.36mm. From Müller et al. (2008).

between the frequency-dependent dispersion characteristics of ultrasonic waves and the patch distribution of partially saturated rocks. Lebedev et al. (2009) showed that the speed at which the samples are saturated may influence the mesoscopic fluid distributions and therefore affect acoustic response. Measured seismograms at different stages of their saturation experiment are shown in Figure 1.11 together with the picked velocities.

The 3-D imaging of rocks from the pore scale to larger scales representing whole samples is a relatively new branch of applied geophysics and sometimes referred to as digital core technology. The general availability of high-resolution measurements of core structure motivates the development of theoretical approaches as well as numerical modelling techniques that allow to simulate the acoustic response of real rocks on the basis of scanned images. An example demonstrating the applicability of poroelastic finite-difference simulations for this purpose is given in section 5.5.

1.4 Motivation and overview of this thesis

The motivation to develop a new finite-difference (FD) implementation of Biot's equations of dynamic poroelasticity is threefold. Actually, several FD schemes have been presented in the past (Zhu and McMechan, 1991; Dai et al., 1995; Jianfeng, 1999, and others, see section 3.1), but the frequency dependence and characteristic scales were not analysed adequately by the authors, as pointed out e. g. by Gurevich (1996). Therefore, the first objective of this thesis is to carefully analyse the accuracy and scalability properties of poroelastic finite-difference schemes, which is done by conducting several fundamental benchmark tests within

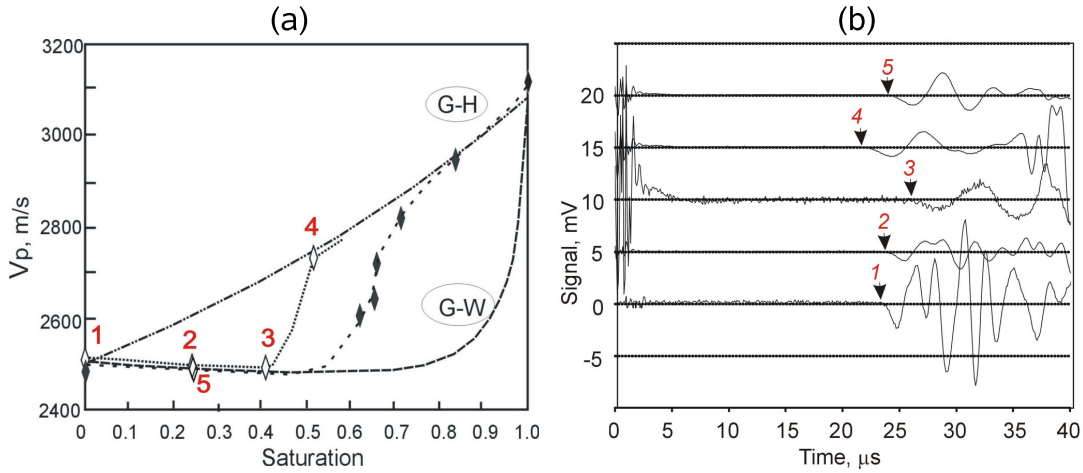


Figure 1.11: (a) Experimentally obtained ultrasonic velocities in a partially saturated rock sample. During one experiment, the sample is saturated with water and the numbers indicate the stage of the saturation experiment. (b) Signals corresponding to the five stages of saturation. From Lebedev et al. (2009).

the frequency band from seismic to ultrasonic. Additionally, the question of numerical stability under strongly heterogeneous conditions is addressed by introducing rotated FD operators that were formerly used only for FD modelling of the elastic wave equation (Saenger et al., 2000).

Secondly, many authors analyse the influence of material properties on wavefield attributes such as attenuation using the spectral ratio method or the frequency shift method (e. g. Helle et al., 2003; Carcione et al., 2003; Picotti et al., 2007). Although this approach is potentially very accurate, the simulation of the underlying wavefields is computationally very expensive. As an alternative to these classic methods, this thesis follows and further develops the ideas of Masson and Pride (2007) and adopts the quasistatic approach to efficiently and accurately infer dispersion and attenuation estimates for heterogeneous media. This part of numerical applications is complemented by elastic scattering experiments and quasistatic finite-element modelling.

Finally, as already mentioned above, FD modelling of poroelastic wave propagation is motivated by the emergence of new laboratory experiments that allow to characterise the details of rock micro- and mesostructure in the context of digital core technology. In combination with physical laboratory experiments, numerical tools may become a powerful simulation tool within the “numerical rock physics lab”.

This thesis is structured as follows. In chapter 2, the mathematical models describing wave propagation in porous media are presented. This includes an introduction to Biot theory, the governing equations, constitutive relations, plane wave solutions for waves propagating in homogeneous media and the formulation of boundary conditions. The chapter contains theoretical estimates for the effective properties of heterogeneous porous media and introduces different models for the quantitative description of wave-induced fluid flow.

If theoretical solutions are not available, approximate solutions can be obtained by using numerical tools. In particular, a new finite-difference scheme is presented that allows to numerically solve the Biot equations of dynamic poroelasticity in heterogeneous media (chapter 3). The stability conditions are reviewed and the problem of numerical stiffness is introduced. It is shown how the FD code is parallelised. Finally, a short introduction is given to the solution of consolidation problems using the finite-element (FE) method.

A detailed analysis of the accuracy properties of the finite-difference scheme is presented in chapter 4. By means of fundamental examples, the applicability of FD method is demonstrated. The obtained numerical results are compared to exact theoretical solutions in order to estimate the approximation error. By a scaling test the parallel performance of the numerical FD solver is checked.

Chapter 5 deals with applying numerical tools for analysing the behaviour of heterogeneous porous media. The scattering from discrete inclusions illustrates the conversion of different wave modes, in particular from fast to slow P -waves. The quasistatic behaviour of synthetic heterogeneous rocks is analysed in order to infer dispersion and attenuation characteristics from relaxation experiments. This is the only class of problems that is based on FE modelling. Then, the focus is on P -wave scattering experiments in random elastic as well as poroelastic media and finally, a ultrasonic laboratory experiment is numerically simulated.

Each chapter contains a discussion of the presented material and the thesis is finalised by concluding remarks in chapter 6.

Chapter 2

Mathematical models for wave propagation in porous media

The propagation of elastic waves in porous media have first been described by Biot in the 1950s as a system of two coupled wave equations. So far, preceding work had focused on effective properties and consolidation of porous solids (Terzaghi and Fröhlich, 1936; Biot, 1941; Gassmann, 1951). Biot's works on porous media extend these results by including inertial effects to the mechanical description and predict three distinct wave modes. In addition to the P - and S -wave commonly known for elastic media, a second so-called slow P -wave exists in poroelastic media. In many publications, the two compressional waves are also referred to as type-I (fast P) and type-II (slow P) waves, respectively.

In order to derive the equations of motion for porous media, Biot (1956a) assumes that continuum mechanics are applicable to the two-phase medium of a solid matrix, saturated with a fluid. He postulates the existence of strain and dissipation potentials and then uses Hamilton's principle to derive the governing equations of motion. Newer works aim at establishing a more rigorous derivation of the equations of motion, based on the clear mechanical first principles on the microscale and using the homogenisation theory (e. g. Lévy, 1979; Burridge and Keller, 1981) or the volume-averaging method (e. g. Pride et al., 1992).

Since the equations of motion are well-established and subject of several reviews and text books (Attenborough, 1982; Bourbié et al., 1987; Coussy, 1991; Carcione, 2001), the derivation will not be repeated here. Instead, the main assumptions of the Biot theory are worked out in the following, some analytical solutions are presented and special cases are considered. In particular, it is shown that the theory is consistent with the elastic wave equation, with the coupled pore pressure diffusion equation and with Gassmann's fluid substitution relation.

An overview of the fundamental concepts of porous media is given in Figure

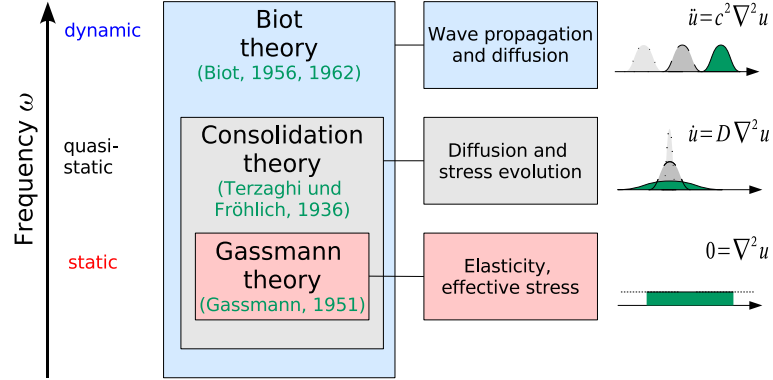


Figure 2.1: Overview of theoretical descriptions of porous media. Gassmann theory allows to calculate the effective moduli of an undrained fluid-saturated medium. The diffusion-type interaction of pore fluid flow with elastic deformation is described by the theory of consolidation. Additionally, inertial effects are considered in Biot theory. The associated frequency regimes are commonly referred to as the static (or elastic) regime, the quasistatic (or diffusive) regime and the dynamic frequency regime.

2.1. Furthermore, the concept of wave-induced fluid flow is introduced. The presentation includes classical theories such as the White theory of partial saturation, but also newly developed so-called continuous random media models.

2.1 Notation

Tensor notation is used throughout this text. The components of a vector \mathbf{b} are written b_i , c_{ij} are components of the second-rank tensor \mathbf{c} . Since there is no possible ambiguity, the terms vector and tensor are used for their respective components, as well, e. g. vector b_i instead of vector components b_i . Conventionally, summation over repeated indices is carried out.

$$\sum_{i=1}^3 c_{ij} b_i = c_{ij} b_i = d_j. \quad (2.1)$$

For convenience, abbreviations for derivatives are used. Derivatives with respect to time t are written as

$$\frac{\partial \phi}{\partial t} = \partial_t \phi = \phi_{,t} = \dot{\phi}, \quad (2.2)$$

$$\frac{\partial^2 \phi}{\partial t^2} = \partial_{tt}^2 \phi = \phi_{,tt} = \ddot{\phi}. \quad (2.3)$$

Spatial derivatives are abbreviated as

$$(\text{grad } \phi)_i = \frac{\partial \phi}{\partial x_i} = \partial_i \phi = \phi_{,i} \quad (2.4)$$

$$\text{div } \mathbf{b} = \frac{\partial b_i}{\partial x_i} = \partial_i b_i = b_{i,i} \quad (2.5)$$

$$(\text{curl } \mathbf{b})_i = \epsilon_{ijk} \frac{\partial b_k}{\partial x_j} = \epsilon_{ijk} \partial_j b_k = \epsilon_{ijk} b_{k,j} \quad (2.6)$$

$$\nabla^2 \phi = \frac{\partial^2 \phi}{\partial x_i \partial x_i} = \partial_i \partial_i \phi = \phi_{,ii}, \quad (2.7)$$

where ϵ_{ijk} is the Levi-Civita-symbol. It is defined as

$$\epsilon_{ijk} = \begin{cases} 1, & \text{if } (i, j, k) \in (1, 2, 3), (2, 3, 1), (3, 1, 2), \\ -1, & \text{if } (i, j, k) \in (1, 3, 2), (3, 2, 1), (2, 1, 3), \\ 0, & \text{else.} \end{cases} \quad (2.8)$$

The Kronecker symbol δ_{ij} is also used as the equivalent of the unit tensor $\mathbf{1}$

$$\delta_{ij} = \begin{cases} 1, & \text{if } i = j, \\ 0, & \text{if } i \neq j. \end{cases} \quad (2.9)$$

A similar symbol is used for the Dirac distribution $\delta(t)$. It is related to the Heaviside step function, both are defined such that

$$\delta(t) = 0 \quad \forall t \neq 0 \quad \text{with} \quad \int_{-\infty}^{\infty} \delta(t) dt = 1, \quad (2.10)$$

$$H(t) = \begin{cases} 0 & \text{for } t < 0, \\ 1 & \text{for } t \geq 0. \end{cases} \quad (2.11)$$

If a Fourier transform is required, it is written using the symbol \mathcal{F} and transformed quantities from the time domain to the frequency domain are indicated by a tilde

$$\mathcal{F} \{ \phi(t) \} = \tilde{\phi}(\omega). \quad (2.12)$$

The kinematic field variables used in the present context are the displacements of the solid frame u_i and the displacements of the fluid phase u_i^f . Relative displacements w_i are defined as

$$w_i \equiv \phi(u_i^f - u_i), \quad (2.13)$$

where porosity ϕ is the volume fraction of the pore space. Strain of the solid matrix ϵ_{ij} is related to the displacements via the kinematic relation

$$\epsilon_{ij} \equiv 1/2 (\partial_j u_i + \partial_i u_j), \quad (2.14)$$

its trace or the divergence of the solid displacement is denoted as

$$\varepsilon \equiv \varepsilon_{ii} = u_{i,i}, \quad (2.15)$$

and that of the relative displacement is called the increment of fluid content

$$\zeta \equiv -w_{i,i}. \quad (2.16)$$

The formulation of the governing equations using the relative displacement instead of the fluid displacement was introduced by Biot (1962). The present work follows closely the modern presentation of the textbook by Carcione (2001).

2.2 Momentum equations

Biot's linear theory of poroelastic wave propagation is valid under the following assumptions: (i) only connected pores are considered in the equations and disconnected pores are treated as part of the solid matrix, (ii) the porous medium is statistically isotropic, i. e. porosity and permeability are the same in all directions, (iii) the wavelength is large compared to the microscopic porescale and (iv) deformations are small in order to ensure linear elastic material behavior.

Then, neglecting source terms, Biot's equations for an isotropic fluid saturated porous medium are given by

$$\rho^b \ddot{u}_i + \rho^f \ddot{w}_i = \partial_j \tau_{ij} \quad (2.17)$$

$$\rho^f \ddot{u}_i + Y * \dot{w}_i = -\partial_i p. \quad (2.18)$$

On the right hand side of these vector equations, the divergence of the total stress field τ_{ij} and the gradient of pore pressure p appear. They are discussed later in section 2.3. Now on the left hand side, four inertial terms are given, with the bulk density ρ^b determined from the density of the solid grains ρ^s and that of the pore fluid ρ^f by

$$\rho^b = \phi \rho^f + (1 - \phi) \rho^s. \quad (2.19)$$

The viscodynamic operator Y is a function of the differential operator ∂_t , and in the frequency domain it becomes a complex, frequency-dependent quantity (Biot, 1956b). Biot evaluates the oscillatory flow in a circular duct as a model for a porous solid and expresses the viscodynamic operator with the help of Bessel functions. Johnson et al. (1987) use the concept of dynamic permeability $k(\omega)$ to introduce the frequency dependence of the operator, i. e.

$$\tilde{Y} = \frac{\eta}{k(\omega)} = \frac{\eta}{\kappa} \cdot \left[\left(1 - \frac{4\nu\omega}{\omega_B n} \right)^{1/2} + \frac{\nu\omega}{\omega_B} \right]. \quad (2.20)$$

Here, η is the dynamic viscosity of the pore fluid, κ is the dc permeability of the porous matrix, ω_B is the critical transition frequency and n is a dimensionless parameter that is related to size of the pore channels. The frequency ω_B plays an important role in the characterisation of the mechanical regime for homogeneous porous solids, since for frequencies lower than ω_B , the flow behaves laminar and is of Poiseuille type. However, for frequencies exceeding ω_B , deviations occur from the laminar flow and therefore additional parameters are needed to characterise the dynamic behaviour of the flow field and of the corresponding mechanical response of the porous composite. The critical frequency is calculated according to

$$\omega_B \equiv \frac{\eta \phi}{\kappa \nu \rho^f}, \quad (2.21)$$

where ν refers to the tortuosity of the pore space, a dimensionless number larger or equal to one. Now, inserting equation 2.21 into equation 2.20 and taking the limit of $n \rightarrow \infty$ results in

$$\tilde{Y} = \frac{\rho^f \nu}{\phi} i \omega + \frac{\eta}{\kappa} = \rho^m i \omega + b. \quad (2.22)$$

The quantities ρ^m and b are referred to as effective fluid density and the hydraulic friction coefficient, respectively. They are given by

$$\rho^m = \frac{\rho^f \nu}{\phi}, \quad (2.23)$$

$$b = \frac{\eta}{\kappa}. \quad (2.24)$$

The simple form of the operator Y given in equation 2.22 is referred to as the classical low-frequency approximation as used in Biot (1956a). The expression consists of an inertial part $\rho^m i \omega$ and a viscous term b , the latter being responsible for internal friction between the pore fluid and the solid frame. Casting equation 2.22 into the momentum equation 2.18 yields the low-frequency formulation of the momentum equations for porous media

$$\rho^b \ddot{u}_i + \rho^f \ddot{w}_i = \partial_j \tau_{ij} \quad (2.25)$$

$$\rho^f \ddot{u}_i + \rho^m \ddot{w}_i = -\partial_i p - b \dot{w}_i. \quad (2.26)$$

In the chapter on numerical methods, this formulation of the momentum equations is usually referred to.

2.3 Constitutive relations

Poroelastic constitutive laws relate the total stress field τ_{ij} and the pore pressure p to the deformation state of a porous medium. The two independent deformation

fields are ε_{ij} and ζ as defined in equations 2.14 and 2.16, respectively. With the help of these strain variables, the poroelastic constitutive relations are written in the general, linear case (Carcione, 2001)

$$\tau_{ij} = c_{ijkl}^u \varepsilon_{kl} - \alpha_{ij} M \zeta, \quad (2.27)$$

$$p = -\alpha_{ij} M \varepsilon_{ij} + M \zeta. \quad (2.28)$$

The three material parameters in these equations are the undrained elasticity tensor c_{ijkl}^u , the tensor of effective stress coefficients α_{ij} and the so-called pore space modulus M . If the medium is isotropic, c_{ijkl}^u can be expressed via the two Lamé parameters λ_u and μ . The tensor α_{ij} then reduces to a scalar, such that

$$c_{ijkl}^u = \lambda_u \delta_{ij} \delta_{kl} + \mu (\delta_{ik} \delta_{jl} + \delta_{il} \delta_{jk}), \quad (2.29)$$

$$\alpha_{ij} = \alpha \delta_{ij}. \quad (2.30)$$

Introducing equations 2.29 and 2.30 into the relations 2.27 and 2.28, the isotropic constitutive relations are obtained as

$$\tau_{ij} = 2\mu \varepsilon_{ij} + \lambda_u \varepsilon \delta_{ij} - \alpha M \zeta \delta_{ij}, \quad (2.31)$$

$$p = -\alpha M \varepsilon + M \zeta. \quad (2.32)$$

In order to illustrate the meaning of these relations, one might consider a few special deformation states and introduce 6 fundamental poroelastic moduli. Beginning with pure shear and pure dilatational deformation under undrained conditions $\zeta \equiv 0$, one obtains expressions for the undrained shear and bulk moduli. Using the deformation angle $\gamma_{ij} = 2\varepsilon_{ij}$ for $i \neq j$, they are

$$G_u \equiv \left. \frac{\tau_{ij}}{\gamma_{ij}} \right|_{\zeta=0, \varepsilon=0} = \frac{2\mu \varepsilon_{ij}}{2\varepsilon_{ij}} = \mu, \quad (2.33)$$

$$K_u \equiv \left. \frac{\tau_{ii}}{3\varepsilon} \right|_{\zeta=0} = \frac{(3\lambda_u + 2\mu)\varepsilon}{3\varepsilon} = \lambda_u + \frac{2}{3}\mu. \quad (2.34)$$

The same two deformations are now applied using drained conditions with $p \equiv 0$. In the pure shear case, $\varepsilon = 0$ and $p = 0$ imply $\zeta = 0$ and therefore

$$G_d \equiv \left. \frac{\tau_{ij}}{\gamma_{ij}} \right|_{p=0, \varepsilon=0} = \frac{2\mu \varepsilon_{ij}}{2\varepsilon_{ij}} = \mu. \quad (2.35)$$

In the case of pure dilatation, equation 2.32 provides $\zeta = \alpha\varepsilon$ and if this is substituted into equation 2.31 one computes the drained bulk modulus K_d as

$$K_d \equiv \left. \frac{\tau_{ii}}{3\varepsilon} \right|_{p=0} = \frac{(3\lambda_u + 2\mu - \alpha^2 M)\varepsilon}{3\varepsilon} = \lambda_u + \frac{2}{3}\mu - \alpha^2 M. \quad (2.36)$$

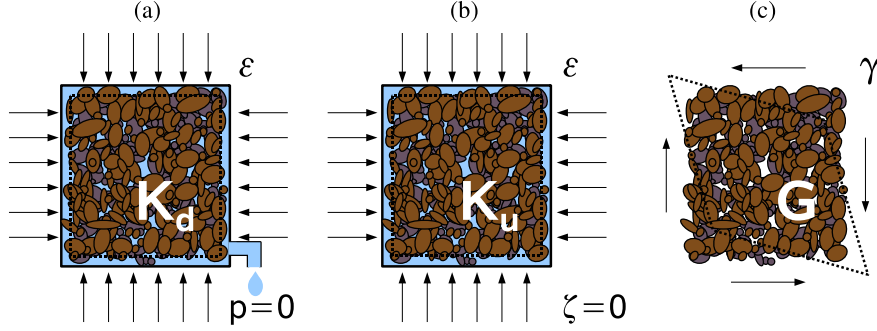


Figure 2.2: Sketches of three deformation experiments for the determination of the drained and undrained bulk moduli K_d and K_u (a,b) as well as the shear modulus G (c) that is independent of the fluid properties.

By comparing the results for the undrained and the drained one obtains easily the famous Gassmann result (Gassmann, 1951)

$$G_u = G_d = G, \quad (2.37)$$

$$K_u = K_d + \alpha^2 M, \quad (2.38)$$

that is that the shear modulus is not affected by the presence of fluid in the pore space and that the undrained bulk modulus is easily obtained from the drained modulus by adding $\alpha^2 M$. The three corresponding experiments for the determination of K_d , K_u and G are shown in Figure 2.2. By means of a simple gedankenexperiment (Biot and Willis, 1957; Brown and Korrington, 1975), α and M can furthermore be related to the bulk moduli of the solid grains K_g and of that of the pore fluid K_f :

$$\alpha = 1 - K_d/K_g, \quad (2.39)$$

$$M = [(\alpha - \phi)/K_g + \phi/K_f]^{-1}. \quad (2.40)$$

Eventually, drained and undrained uniaxial strain conditions provide two vertical incompressibilities, P_d and P_u , that are also denoted as L and H , respectively. Since they are closely related to the velocity of P -waves, they are also called drained and undrained P -wave moduli. Without derivation, they are given as

$$P_d = L \equiv \left. \frac{\tau_{zz}}{\varepsilon_{zz}} \right|_{p=0, \varepsilon_{xx}=\varepsilon_{yy}=0} = K_d + 4/3 G, \quad (2.41)$$

$$P_u = H \equiv \left. \frac{\tau_{zz}}{\varepsilon_{zz}} \right|_{\zeta=0, \varepsilon_{xx}=\varepsilon_{yy}=0} = K_u + 4/3 G. \quad (2.42)$$

2.4 Plane wave solutions

A system of coupled linear wave equations for the displacements u_i and w_i is obtained by inserting the constitutive relations 2.31 and 2.32 into the momentum equations 2.17 and 2.18, so that

$$\rho^b \ddot{u}_i + \rho^f \ddot{w}_i = (\lambda_u + \mu) u_{j,ji} + \mu u_{i,jj} + \alpha M w_{j,ji}, \quad (2.43)$$

$$\rho^f \ddot{u}_i + Y * \dot{w}_i = \alpha M u_{j,ji} + M w_{j,ji}. \quad (2.44)$$

Using the vector theorem

$$u_{i,jj} = u_{j,ji} - \epsilon_{ijk} \epsilon_{klm} u_{m,jl} \quad (2.45)$$

and substituting the poroelastic moduli $H = \lambda_u + 2\mu$ as well as $G = \mu$ and $C = \alpha M$, the wave equations become

$$\rho^b \ddot{u}_i + \rho^f \ddot{w}_i = H u_{j,ji} + C w_{j,ji} - G \epsilon_{ijk} \epsilon_{klm} u_{m,jl} \quad (2.46)$$

$$\rho^f \ddot{u}_i + Y * \dot{w}_i = C u_{j,ji} + M w_{j,ji}. \quad (2.47)$$

On the right hand side of equations 2.46 and 2.47, the spatial derivatives grad div and rot rot of the displacement fields appear. Now, the Helmholtz theorem states that any vector field can be decomposed into the sum of an irrotational and a solenoidal vector field. This means that for the irrotational part of the displacement field, the contribution from the third term on the right hand side of equation 2.46 disappears. At the same time, for the solenoidal part all the terms that contain the divergence operator vanish. As in the case of elastic wave propagation, compressional and shear waves are therefore decoupled. The dispersion relation of all wave modes are obtained by using plane waves as an ansatz for the solution of equations 2.46 and 2.47.

A plane wave propagating in direction x with wavenumber k and circular frequency ω has the form

$$\mathbf{u} = \mathbf{u}_0 \exp[i(kx - \omega t)], \quad (2.48)$$

where $\mathbf{u}(x, t) = (u, w)$ and $\mathbf{u}_0 = (u_0, w_0)$ is constant. Inserting this ansatz into the wave equations and assuming irrotational motion, one finds the following equation in matrix form

$$\omega^2 \mathbf{P} \mathbf{u} = k^2 \mathbf{H} \mathbf{u}, \quad (2.49)$$

where the matrices \mathbf{P} and \mathbf{H} are given by

$$\mathbf{P} = \begin{pmatrix} \rho^b & \rho^f \\ \rho^f & \tilde{Y}/(i\omega) \end{pmatrix} \quad (2.50)$$

and

$$\mathbf{H} = \begin{pmatrix} H & C \\ C & M \end{pmatrix}. \quad (2.51)$$

This is an eigenvalue problem with the unknown eigenvalues $(k/\omega)^2$. They are calculated as the solution to the characteristic equation

$$\det(\mathbf{H}^{-1}\mathbf{P} - (k/\omega)^2 \mathbf{1}) = 0. \quad (2.52)$$

Setting

$$\mathbf{D} = \mathbf{H}^{-1}\mathbf{P} \quad (2.53)$$

one obtains explicitly the dispersion relation for plane P -waves as

$$\frac{k^2}{\omega^2} = \frac{1}{2} \left[\text{tr } \mathbf{D} \pm (\text{tr}^2 \mathbf{D} - 4 \det \mathbf{D})^{1/2} \right] \quad (2.54)$$

with

$$\det \mathbf{D} = \det \mathbf{P} / \det \mathbf{H} \quad (2.55)$$

$$\det \mathbf{H} = HM - C^2 \quad (2.56)$$

$$\det \mathbf{P} = \rho^b \tilde{Y} / (\imath \omega) - \rho^f \rho^f \quad (2.57)$$

$$\text{tr } \mathbf{D} = 1 / \det \mathbf{H} \left[\rho^b M - 2\rho^f C + H\tilde{Y} / (\imath \omega) \right]. \quad (2.58)$$

The same reasoning leads to a characteristic equation in the case of purely solenoidal particle motion. In that case one has

$$\det(\mathbf{P}^{-1}\mathbf{G} - (\omega/k)^2 \mathbf{1}) = 0, \quad (2.59)$$

where the matrix \mathbf{G} is now given by

$$\mathbf{G} = - \begin{pmatrix} G & 0 \\ 0 & 0 \end{pmatrix}. \quad (2.60)$$

Due to the irregular but simple form of \mathbf{G} , the dispersion relation for S -waves is

$$\frac{k^2}{\omega^2} = [\text{tr}(\mathbf{P}^{-1}\mathbf{G})]^{-1} = - \det \mathbf{P} \frac{\imath \omega}{\tilde{Y}G}. \quad (2.61)$$

So far, the two roots of the characteristic equations for compressional waves and the third root of that for shear waves correspond to the three wave modes in porous media. The compressional waves are referred to as fast and slow P -waves or sometimes waves of the first and second kind, respectively. The fast P -wave behaves similarly to the compressional wave mode in elastic media, which is why it often simply referred to as *the P-wave*. The slow P -wave is a particularity of poroelastic media and it usually strongly attenuated in real porous rocks.

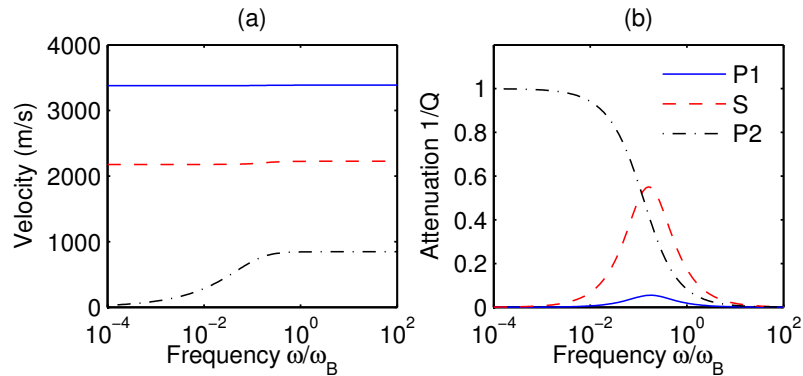


Figure 2.3: Dispersion (a) and attenuation (b) of the three wave modes in a porous medium (water saturated sandstone, see Tables 2.1 and 2.2). Fast P - and S -wave show very small dispersion, while slow P -velocity tends to zero at low frequencies. Note that the inverse quality factors of $P1$ and S in (b) have been multiplied by 50.

Actually, at frequencies below the critical Biot frequency ω_B , this wave mode becomes diffusive, while at frequencies higher than ω_B , it is a propagating wave mode. Due to the diffusive behaviour at low frequencies, the slow P -wave is often considered as a diffusion wave as discussed in more detail in section 2.6.

Propagation velocities v and attenuation in the form of the quality factor Q are calculated from the wavenumbers as

$$v = \frac{\omega}{\operatorname{Re} k} \quad (2.62)$$

$$Q^{-1} = \frac{2 \operatorname{Im} k}{\operatorname{Re} k}. \quad (2.63)$$

Dispersion curves as well as attenuation behaviour for compressional and shear waves are given in Figure 2.3. The medium considered is water-saturated consolidated sandstone model with material parameters given in Tables 2.1 and 2.2. The dispersion curves in Figure 2.3a show a very small frequency dependence of the fast P - and S - waves. Both are higher than the velocity of the slow P -wave, of which the velocity tends to zero as frequency decreases. On the other hand, the attenuation of the slow P -wave at frequencies below ω_c tends to one, see Figure 2.3b. Attenuation values for the S - and P -waves is much smaller; for convenience, the attenuation amplitudes have been enlarged by a factor of 50.

2.5 Boundary conditions

In order to fully specify a particular poroelastic problem, boundary conditions and initial conditions are required to constrain the solution of the governing

equations. For wave propagation problems, the initial conditions are usually a stress-free medium at rest, i. e. all field variables are 0. Generally, the initial conditions must fulfil all the governing equations and they must be consistent with the boundary conditions. Deresiewicz and Skalak (1963) considered the possible cases for external and internal boundaries. A traction free boundary at the edge of the considered problem domain is described by setting the normal stress component and the pore pressure to 0 as

$$\tau_{ij} n_j = 0, \quad p = 0, \quad (2.64)$$

with n_j being the unit vector in normal direction. Similarly, setting the displacements to 0 gives fixed boundaries with

$$u_i = 0, \quad w_i n_i = 0. \quad (2.65)$$

Obviously, boundary conditions of mixed type, e. g. a mechanically constrained but drained condition or a unconfined/undrained condition are also possible. If two porous media are in welded contact with each other, continuity is required for traction, pore pressure, total displacement and the normal component of the relative displacement. Sometimes, a mixed boundary condition is applied for the pore pressure to account for partial closure of the pore space at the interface. This is done by introducing a surface resistance parameter k , where $k = 0$ corresponds to the standard case of an open internal boundary. Denoting the two sides of the interface by a superscript, the porous-porous boundary conditions then read

$$u_i^1 = u_i^2, \quad w_i^1 n_i = w_i^2 n_i, \quad \tau_{ij}^1 n_j = \tau_{ij}^2 n_j, \quad p^1 - p^2 = k \dot{w}_i n_i. \quad (2.66)$$

Eventually, the two special cases of a porous medium in contact with a fluid or with an elastic solid are given. For a porous-solid interface one has

$$u_i^1 = u_i^2, \quad w_i^1 n_i = 0, \quad \tau_{ij}^1 n_j = p^1 = \tau_{ij}^2 n_j, \quad (2.67)$$

and for a porous-fluid interface

$$(u_i^1 + w_i^1) n_i = u_i^2 n_i \quad \tau_{ii}^1/3 = p^1 = p^2. \quad (2.68)$$

On the basis of these boundary conditions, reflection and transmission coefficients of waves in porous media are derived in works by Deresiewicz and Skalak (1963) for reflections at an external boundary and by Dutta and Odé (1983) for a gas-water interface. Simplified expressions for normal incidence are given in Gurevich et al. (2004).

Table 2.1: Typical material properties of a consolidated and unconsolidated sandstone.

		unit	consolidated	unconsolidated
Grain bulk modulus	K_g	GPa	35.0	35.0
Drained bulk modulus	K_d	GPa	5.0	2.5
Shear modulus	G	GPa	11.0	1.0
Porosity	ϕ		0.2	0.3
Tortuosity	ν		2.0	2.0
Permeability	κ	10^{-12}m^2	1	1000
Grain density	ρ_g	kg/m^3	2650	2650

2.6 Quasistatic behaviour of porous media

Many mechanical processes in porous media are slow in the sense that the inertial terms in the momentum equations become negligible. The temporal change in the displacement and stress fields is then only driven by the internal friction between the grain framework and the pore fluid. In this case, the viscodynamic operator reduces to the friction coefficient $b = \eta/\kappa$ and the momentum equations 2.43 and 2.44 become

$$0 = \tau_{ij,j} \quad (2.69)$$

$$b \dot{w}_i = -p_{,i}. \quad (2.70)$$

These two equations are an equilibrium condition for the total stress field τ_{ij} and the equation of Darcy flow stating the proportionality between the negative pressure gradient $\partial_i p$ and the filtration velocity \dot{w}_i . A different way of presenting the equilibrium and Darcy's law is obtained by taking the divergence of the Darcy equation and substituting the constitutive relations. Following Wang (2000), one finds an equilibrium condition expressed in terms of the displacement field u_i

Table 2.2: Material properties of fluids typically found in reservoirs (water, gas, oil) or in the laboratory (air) (Batzle and Wang, 1992).

		unit	water	oil	gas	air
Bulk modulus	K_f	GPa	2.25	1.3	0.1	0.00014
Density	ρ_f	kg/m^3	1000	850	100	1
Viscosity	η	mPas	1.0	4.0	0.22	0.02

coupled with an inhomogeneous diffusion equation for the pore pressure p as

$$0 = (\lambda_d + \mu) u_{j,ji} + \mu u_{i,jj} - \alpha p_{,i} \quad (2.71)$$

$$\alpha \dot{u}_{i,i} + \dot{p}/M = p_{,ii}/b. \quad (2.72)$$

Equations 2.71 and 2.72 describe the coupled quasistatic deformation and pore pressure diffusion in porous media, such as e. g. consolidation processes of fluid saturated soils or reservoir compaction during depletion. They imply that in the general case, the pore pressure field cannot be calculated by a single diffusion equation alone, but the influence of temporal changes in pore pressure on the overall stress and deformation field (and vice versa) needs to be accounted for. In four specific circumstances, the pore pressure equation, however, uncouples from the equilibrium equation and can therefore be solved independently (Wang, 2000). These circumstances are “(1) steady state, (2) a state of uniaxial strain and constant vertical stress, (3) a highly compressible fluid, and (4) an irrotational displacement field in an infinite domain without body forces” (Wang, 2000).

For the four cases, simple analytical solutions are available. In particular, under assumption (4), the diffusion equation 2.72 is decoupled from the strain term and becomes a homogeneous diffusion equation

$$\dot{p}/N = p_{,ii}/b \quad (2.73)$$

with the poroelastic modulus

$$N = \frac{MP_d}{H}. \quad (2.74)$$

The quotient of b and N is called the hydraulic diffusivity

$$D = N/b = \frac{\kappa MP_d}{\eta H} \quad (2.75)$$

and it is the main material parameter describing diffusion problems. In the unidimensional case, the solution of equation 2.73 due to an instantaneous point source with $p(x, t = 0) = \delta(x)$ is (Rudnicki, 1986)

$$p(x, t) = \frac{1}{\sqrt{4\pi Dt}} \exp \frac{-x^2}{4Dt} \quad (2.76)$$

Now, if the point source is a Heaviside step function in time $p(x = 0, t) = H(t)$, the unidimensional pore pressure response is expressed as

$$p(x, t) = \text{erfc} \frac{x}{\sqrt{4Dt}}. \quad (2.77)$$

Some pore pressure profiles resulting of a point source in a 1-D medium are given in Figure 2.4.

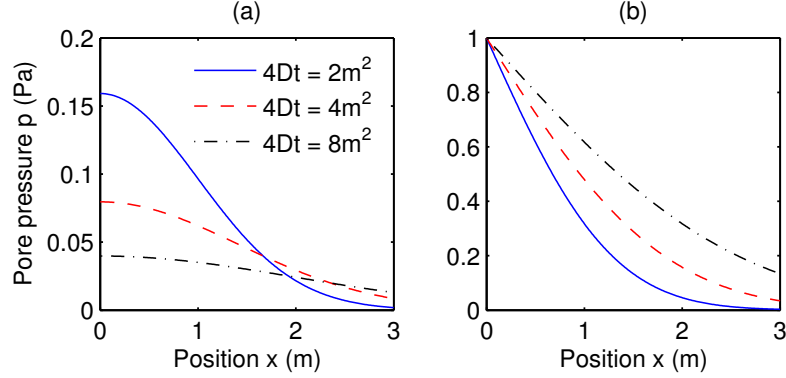


Figure 2.4: Quasistatic pore pressure response due to a point source in a unidimensional homogeneous porous medium (water saturated consolidated sandstone, see Tables 2.1 and 2.2). Profiles are given for (a) an instantaneous source and (b) a constant pressure source.

Eventually, the diffusion equation is applied to derive an low-frequency approximation of the slow P -wavenumber that was already given in equation 2.54. Introducing the plane wave ansatz into equation 2.73 gives the dispersion relation for a “pure diffusion wave”

$$\frac{k^2}{\omega^2} = \frac{\imath b}{\omega N}. \quad (2.78)$$

Simple approximations are obtained for the fast P -wave and for the shear wave, as well, by considering that at low frequencies with $\omega \ll \omega_B$ the dispersion and attenuation are very small. Actually, at low frequencies, friction between the fluid and the grain matrix is dominant and the porous medium is practically undrained. Setting the relative motion w_i to zero, the coupled wave equation 2.46 reduces to a purely elastic wave equation

$$\rho^b \ddot{u}_i = H u_{j,j} - G \epsilon_{ijk} \epsilon_{klm} u_{m,jl} \quad (2.79)$$

from which dispersion relations for the fast P - and S -waves are derived as

$$\frac{k^2}{\omega^2} = \frac{\rho^b}{H} \quad (2.80)$$

and respectively

$$\frac{k^2}{\omega^2} = \frac{\rho^b}{G}. \quad (2.81)$$

Figure 2.5 shows a comparison of predicted wave propagation velocities by the full formulas 2.54–2.61 and the approximations 2.78, 2.80 and 2.81. As is demonstrated there, the simplified formulas provide a good approximation of the full wavenumbers at frequencies sufficiently below the critical Biot frequency ω_B .

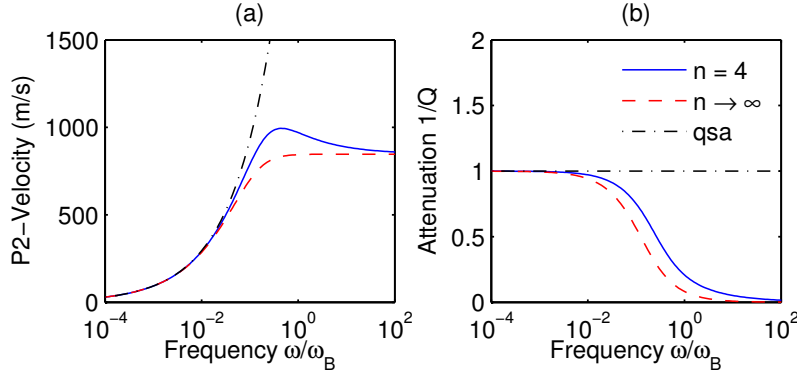


Figure 2.5: Dispersion velocities and attenuation of the slow P -wave in poroelastic media. The quasistatic approximation (qsa) is compared to the full formulation with dynamic operators according to equation 2.20.

2.7 Heterogeneous porous media

So far, only waves in homogeneous porous media have been considered, where homogeneous refers to all scales larger than the porescale. For the homogeneous case in an unbounded domain, plane wave solutions as well as Green's functions for instantaneous point sources are available (See Karpfinger, 2006, for a review). In contrast, for heterogeneous media, i. e. if the medium properties vary as a function of position, general solutions are available only for a few special cases. Often, the properties of the heterogeneous medium are expressed based on the statistical properties of the single constituents. An average of a quantity ϕ over the representative elementary volume is then denoted as

$$\langle \phi \rangle = \frac{1}{V} \int_{\text{REV}} \phi(\mathbf{x}) dV. \quad (2.82)$$

If a mixture of two or more fluid phases fill the pore space of a homogeneous rock, one speaks of partial saturation. In contrast, a double porosity model consists of a heterogeneous rock fully saturated with only one fluid phase. Partial saturation occurs typically in a reservoir where one fluid, e. g. oil is replaced by another fluid such as water during production. Usually, the first fluid phase is not completely replaced by the second fluid, but both may form patches on multiple scales. An example of double porosity media is a fractured reservoir in which cracks and fractures can be considered as soft and permeable inclusions within a stiff host rock.

A particularity of partial saturation is that exact theoretical limits are available for the estimation of effective elastic moduli. This estimate is based on the assumption that a propagating compressional or shear wavelength is much larger than the scale of the fluid patch. The first result is that the effective shear modu-

lus is not affected by the presence of different fluids in the rock, which is a direct consequence of the solenoidal character of the shear motion and the constitutive relations 2.31 and 2.32. Now, if a compressional wave propagates through a partially saturated medium, a fluid diffusion process is induced and the spatial scale of this process is estimated as

$$\lambda_D = \sqrt{\frac{D}{\omega}}, \quad (2.83)$$

where the approximate diffusivity $D = K_f/b$ is the governing hydraulic parameter. λ_D is sometimes called diffusion length (Norris, 1993). If it is small compared to the scales of the fluid patches, no internal fluid flow occurs, the system is unrelaxed and behaves like a heterogeneous elastic medium with varying bulk modulus but constant shear modulus. In this particular case, the theorem of Hill (1963) states that the heterogeneous medium is effectively isotropic with a bulk modulus K_{eff} is determined as the weighted harmonic average of the individual bulk moduli, independent of the distribution of the fluid phases inside the volume. One writes

$$K_{\text{eff}}^H = K_H = \langle K^{-1} \rangle^{-1}, \quad (2.84)$$

where the individual moduli K are calculated using Gassmann's equation. This limit is referred to as Gassmann-Hill.

Now, if the diffusion scale is much larger than the spatial scale of the system, the pore pressure is equilibrated throughout the medium and the effective modulus is obtained by substituting a harmonically averaged effective fluid bulk modulus into Gassmann's equation

$$K_{\text{eff}}^f = \langle K_f^{-1} \rangle^{-1} \quad (2.85)$$

$$K_{\text{eff}}^W = K_W = K_d + \frac{\alpha^2}{(\alpha - \phi)/K_g + \phi/K_{\text{eff}}^f}, \quad (2.86)$$

yielding the so-called effective fluid model or Gassmann-Wood average (Wood, 1955). In Figure 2.6, the theoretical limits are given for two fluid mixtures (water-gas and water-air) that saturate a consolidated sandstone, for material properties see Tables 2.1 and 2.2. Both curve pairs show qualitatively the same behaviour: an approximately linear increase in P -wave velocity from fully gas- to fully water-saturated is characteristic for the Gassmann-Hill bound, while the Gassmann-Wood bound shows a very strong decay of the effective bulk modulus when only a little gas is introduced into a fully water-saturated medium. The decay is the more pronounced, the stronger the contrast is between the fluid phases.

The criterion 2.83 has been given to distinguish between the unrelaxed state (Hill) and the relaxed state (Wood). The limits can as well be considered as the

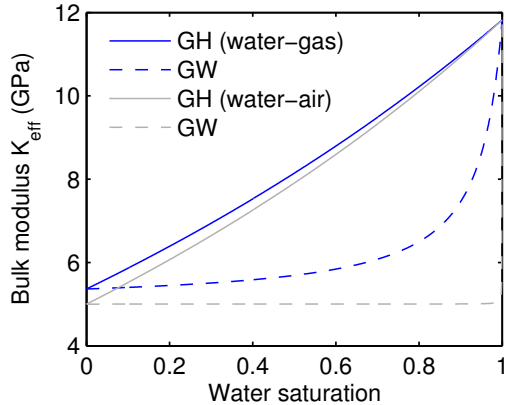


Figure 2.6: Gassmann-Hill and Gassmann-Wood bounds for a consolidated sandstone saturated with a mixture of water and gas, or water and air, respectively. The curves show the effective bulk modulus K_{eff} as function of water saturation.

high- and low-frequency limits of partial saturation models, where a crossover occurs around the critical frequency

$$\omega_c = \frac{D}{L^2}. \quad (2.87)$$

Unfortunately, the Hill theorem does not apply to an elastic medium with varying shear modulus. This implies that theoretical bounds for double porosity media are in general not available. An exception is the case when the porous matrix is a conglomerate of only two porous phases that are distributed such that the conglomerate is again isotropic. Then, effective bulk moduli for the grains and for the matrix are computed directly from the moduli of the constituents (Brown and Korrington, 1975; Berryman and Milton, 1991). Their results are a generalisation of the works of Gassmann (1951).

Another important case with exact theoretical bounds is given by a medium consisting of a stack of porous layers with varying elastic properties. At high frequencies, similar to the patchy-saturation case, there is no time for relaxation by fluid flow and therefore the stack of porous layers behaves like a stack of equivalent elastic layers with moduli determined according to the Gassmann equation. For this case, it is known that the effective medium is transversely isotropic which is described by five independent elastic constants that are unambiguously determined by proper averaging of the elastic moduli of the layers. This averaging is called Backus averaging (Backus, 1962). A poroelastic Backus average is described by Gelinsky and Shapiro (1997) for porous layers with equilibrated pore pressure, i. e. for the relaxed state. Formulas for calculating the effective moduli and corresponding wave velocities are given in appendix C.2.

As an example consider a water-saturated consolidated sandstone with 3% horizontally layered inclusions of unconsolidated sand, such as given in Table 2.1. Angle-dependent velocities for P - and S -waves are shown in Figure 2.7. First off all, in a transversely isotropic medium, three different wave modes exist: a

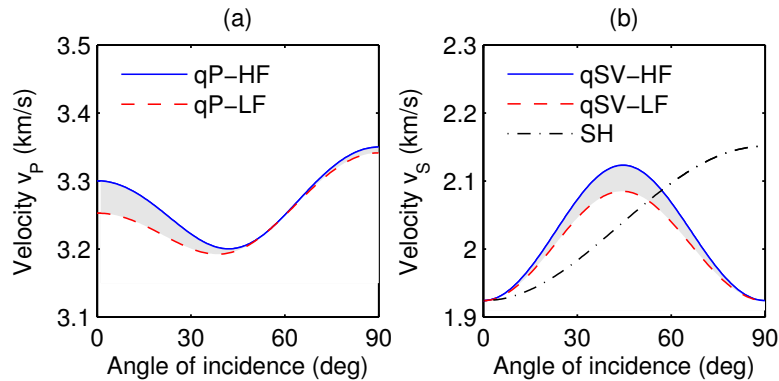


Figure 2.7: Propagation velocities in an effectively anisotropic porous medium, calculated with low-frequency (LF) and high-frequency (HF) limits of poroelastic Backus averaging. In (a), P -wave velocities are shown, in (b) shear waves. While qP and qSV are dispersive, the pure shear mode SH is not. At zero incidence, the velocities of qSV and SH coincide.

pure shear or SH -wave with polarisation perpendicular to the symmetry axis, as well as a quasi compressional qP -wave and a quasi shear qSV -wave (e. g. Auld, 1990). While the SH is always solenoidal, the other wave modes are of mixed type with rotational and divergence components. The angle of incidence is the angle between the wave vector and the symmetry axis. Three main observations are made: (1) The normal incident (0°) P -wave velocities are smaller than the P -wave velocities within the plane of symmetry at 90° . (2) Shear wave velocity is minimal at 0° and 90° for the vertically polarised qSV -wave where it coincides with the horizontally polarised SH -wave at 0° . (3) Both qP - and qSV -waves are dispersive as is indicated by the grey-shaded areas in Figure 2.7a and b. In contrast, the SH -wave is not dispersive, high and low-frequency (relaxed and unrelaxed) behaviour is the same, which is a direct consequence of the purely solenoidal character of this wave mode.

2.8 Wave-induced fluid flow

After establishing the fundamental high- and low-frequency bounds for heterogeneous porous media, rock physics models are now briefly discussed that describe the frequency-dependence of the poroelastic moduli. In the context of wave scattering, the mechanism of wave-induced fluid flow is introduced.

One of the main results of the Biot theory is the existence of the third slow P -wavemode that behaves diffusive at low frequencies, i. e. at frequencies $\omega \ll \omega_B$. In that regime, the fast P - and S -waves do not show considerable attenuation and dispersion.

This situation is very different in heterogeneous porous media, since wave scattering may occur at internal interfaces, thus affecting the wave amplitude. In general, scattering is most effective if the scale of the heterogeneity is of the same order of magnitude as that of the scattered wavemode. A particularity of the poroelastic rheology lies in the properties of the slow P -wavemode and obviously, the interaction of fast P - and S -waves with the slow P -deserves particular consideration. Conversion scattering from fast P - and S - to slow P -waves is referred to as wave-induced fluid flow (e. g. Müller and Gurevich, 2005b). This process usually occurs at heterogeneities that are much smaller than the incident wavelength. Such a scale is called mesoscopic and the wave-induced flow is also referred to as mesoscopic flow.

From a physical point of view, the incident wave field induces pore pressure differences across internal interfaces within a heterogeneous porous medium. During wave propagation, these differences drive fluid flow that tend to reequilibrate the disturbed pore pressure. Since this fluid flow is associated with internal friction, energy is withdrawn from the incident wavefield, causing attenuation and velocity dispersion. For reservoir rocks, mesoscopic flow is considered as one of the most important loss mechanisms at seismic frequencies.

Rock physics models quantifying the effect of wave-induced flow are grouped according to the material property that is heterogeneous, e. g. partial saturation or double porosity. A further distinguishing feature of the models is the dimensionality: some assume unidimensional layering, others make use of three-dimensional structures. And finally, there are models assuming a regular and periodic pattern while more recently, models assume a random distribution of the material parameters. Without making the claim to completeness, in Table 2.3, an overview of several theories for wave-induced flow is given. They are reviewed in the following.

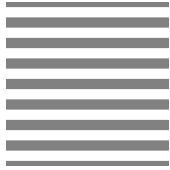
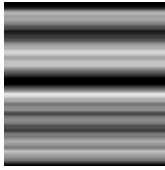
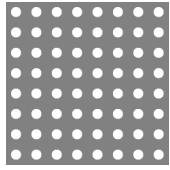
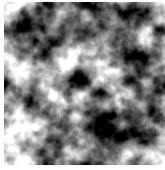
2.8.1 White's model for partial saturation

White et al. (1975) presented a model to compute P -wave velocity and attenuation for partially saturated rocks, where the medium consists of an alternating stack of layers with different fluid properties. A frequency-dependent estimate of the effective modulus H_{eff} for the periodic layers model takes the form (White et al., 1975; Norris, 1993)

$$H_{\text{eff}}^{-1}(\omega) = \left\langle \frac{1}{H} \right\rangle + \frac{2}{i\omega L} \frac{\left(\frac{\alpha M}{H}\right)_1 - \left(\frac{\alpha M}{H}\right)_2}{\left(\frac{b}{k_d} \cot \frac{k_d S L}{2}\right)_1 + \left(\frac{b}{k_d} \cot \frac{k_d S L}{2}\right)_2}, \quad (2.88)$$

where S is the fluid saturation, k_d is the diffusion wavelength in the quasistatic approximation (see eq. 2.78) and L is the spatial layer period. Starting from the

Table 2.3: Overview of rock physics theories for wave-induced fluid flow.

	periodic		random	
1-D		White et al. (1975), Norris (1993), Brajanovski et al. (2005)		Gurevich and Lopatnikov (1995), Gelinsky et al. (1998), Müller and Gurevich (2004)
3-D		White (1975), Dutta and Odé (1979), Johnson (2001), Galvin and Gurevich (2006)		Müller and Gurevich (2005a), Toms et al. (2007), Müller et al. (2008)

results of White et al. and Norris, Brajanovski et al. (2005) developed a unidimensional model for a double porosity media, in particular to simulate thin soft cracks within a stiffer porous matrix.

A famous model of White (1975) considers spherical porous inclusions embedded within a rock saturated with a different fluid. The same configuration has been investigated by Dutta and Odé (1979) on a more fundamental basis using poroelasticity theory, who found similar results to that of White. According to Mavko et al. (1998) the modulus H_{eff} is expressed as

$$H_{\text{eff}}(\omega) = \frac{K_{\infty}}{1 - K_{\infty}W(\omega)} + \frac{4}{3}G, \quad (2.89)$$

where meaning of the quantities K_{∞} and W are given in appendix C.4. An example of different models describing the effect of wave-induced flow on velocity dispersion and attenuation is given in Figure 2.8. Consider a consolidated sandstone (see Table 2.1) saturated 50% with water and 50% with gas.

Two models considered are the White models for periodically layered media (White 1D), and for a periodic array of spherical inclusions (White 3D). The third model is the continuous random medium model (CRM exp.) with an exponential correlation function (Toms et al., 2007). The frequencies are normalised with the critical frequency $\omega_c = D/L^2$, where D is the diffusivity of the fully water-saturated rock and L is the layer period, the inclusion diameter or the correlation length, respectively. The two White models provide approximately the same dispersion curve and the same amount of attenuation with small frequency shift. Attenuation is maximum at about ω_c . The curves provided by the CRM model do not differ strongly from the results predicted by White's theory. However, the

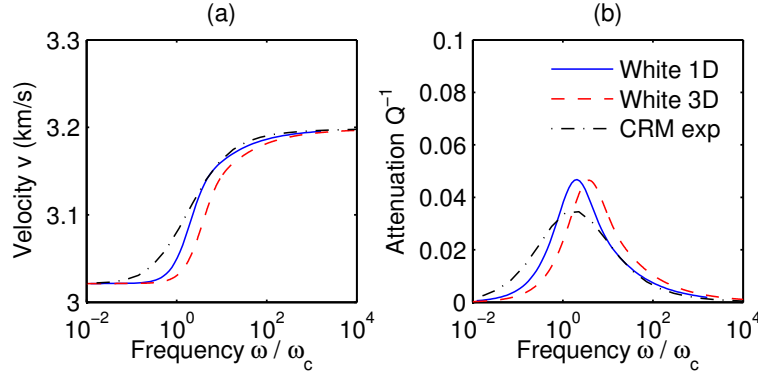


Figure 2.8: Comparison of three theories of partial saturation. Dispersion and attenuation curves are shown for a consolidated sandstone with 50% water and 50% gas saturation (see Tables 2.1 and 2.2 for material parameters).

dispersion curve is smoother and the attenuation peak is a little less pronounced. A detailed comparison of the different models for partial saturation is given in Toms et al. (2006).

2.8.2 Continuous random media models

A new direction of modelling the effective frequency-dependent properties of heterogeneous porous rocks was pioneered by Gurevich and Lopatnikov (1995) who investigate a stack of fine porous layer with a continuous random distribution of the poroelastic coefficients. They use the method of statistical smoothing, an approach that has later been generalised to the 3-D case by (Müller and Gurevich, 2005a,b). The model of Müller and Gurevich predicts the complex effective P -wavenumber in a 3-D randomly heterogeneous porous solid as

$$k_{\text{eff}}(\omega) = k_c \left(1 + \Delta_2 + \Delta_1 k_d^2 \int_0^\infty r B(r) \exp(i k_d r) dr \right), \quad (2.90)$$

where k_c and k_d are the wavenumbers of the fast and the slow P -wave in the quasi-static approximation. The integral containing the spatial correlation function $B(r)$ has to be evaluated according to the statical properties of the underlying medium. Δ_1 and Δ_2 are dimensionless constants given by (Müller and Gurevich, 2005a)

$$\Delta_1 = \frac{\alpha^2 M L}{2 H^2} (\sigma_{LL}^2 - 2 \sigma_{LM}^2 + \sigma_{MM}^2), \quad (2.91)$$

$$\Delta_2 = \frac{L}{2 H} \sigma_{LL}^2 + \frac{\alpha^2 M}{2 H} \sigma_{MM}^2, \quad (2.92)$$

where σ_{LL} , σ_{MM} , σ_{LM} are variances and cross variances of the drained P -wave modulus L and the pore space modulus M . In double-porosity media, σ_{MM} vanishes, while in partially-saturated porous media, the rock is homogeneous and consequently $\sigma_{LL} = 0$. In the latter case, one has

$$\Delta_1 = \frac{\alpha^2 ML}{2H^2} \sigma_{MM}^2, \quad (2.93)$$

$$\Delta_2 = \frac{\alpha^2 M}{2H} \sigma_{MM}^2 = \frac{H}{L} \Delta_1. \quad (2.94)$$

If an average background P -wave modulus H_0 is introduced as

$$H_0 = K_0 + \frac{4}{3}G = K_d + \alpha^2 \langle M \rangle + \frac{4}{3}G, \quad (2.95)$$

and using equation 2.90, one derives an effective P -wave modulus H_{eff} written as

$$H_{\text{eff}}(\omega) = H_0 (1 - \Delta_2 - \Delta_1 \xi)^2 \quad (2.96)$$

with the integral

$$\xi = k_d^2 \int_0^\infty r B(r) \exp(-k_d r) dr \quad (2.97)$$

containing all information about the actual medium distribution as defined by the correlation function $B(r)$. It has been shown that the effective modulus H_{eff} given in equation 2.96 is consistent with the theoretical bounds of Gassmann-Wood and Gassmann-Hill only if the contrast in material properties are small (Müller and Gurevich, 2004). In order to make the model consistent with the theoretical limits, a scaling function is conveniently introduced as (Müller et al., 2008)

$$H_{\text{eff}}^{SC}(\omega) = H_W (1 + \delta[\tau \xi^2 + (\tau - 1)\xi]) \quad (2.98)$$

with

$$\delta = \frac{H_H - H_W}{H_W}, \quad (2.99)$$

$$\tau = \frac{\Delta_1}{2} = \frac{\alpha^2 ML}{4H^2} \sigma_{MM}^2. \quad (2.100)$$

This scaled model is called continuous random media (CRM) model for partial saturation. The only thing left to do is to specify a particular random distribution and calculate the corresponding integral to yield the frequency-dependent function ξ . The solutions are given for the normal (Gaussian) distribution, the exponential distribution and for the von-Kármán type fractal distribution. The

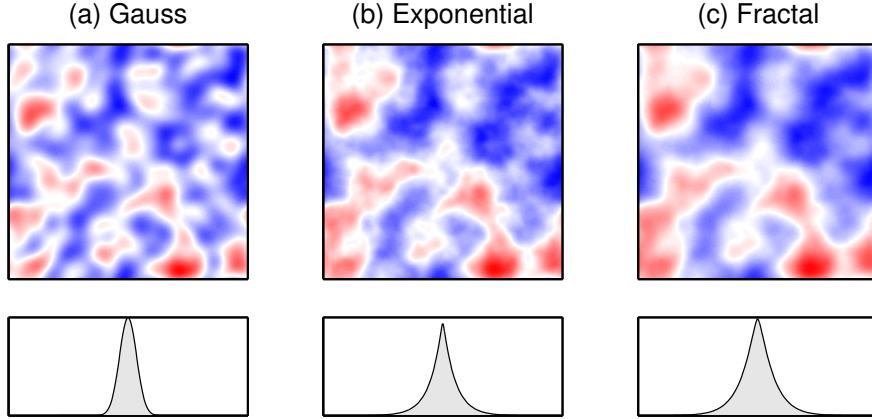


Figure 2.9: Realisations of random media and corresponding correlation functions: (a) Gaussian, (b) exponential, (c) fractal with $\nu = 0.8$.

correlation functions are (Sato and Fehler, 1998, pages 14–16)

$$B^{\text{gauss}}(r) = \sigma_{MM}^2 \exp\left(-\frac{r^2}{a^2}\right), \quad (2.101)$$

$$B^{\text{exp}}(r) = \sigma_{MM}^2 \exp\left(-\frac{|r|}{a}\right), \quad (2.102)$$

$$B^{\text{fractal}}(r) = \sigma_{MM}^2 \frac{2^{1-\nu}}{\Gamma(\nu)} \left(\frac{r}{a}\right)^\nu K_\nu\left(\frac{r}{a}\right), \quad (2.103)$$

where Γ is the Gamma function and K_ν is the modified Bessel function of the second kind of order ν . Spectra of these distributions $\Phi(k) = \mathcal{F}\{B(r)\}$ are obtained by 3-D Fourier transform as

$$\Phi^{\text{gauss}}(k) = \sigma_{MM}^2 \frac{a^3}{8\pi^{3/2}} \exp\left(-\frac{k^2 a^2}{4}\right), \quad (2.104)$$

$$\Phi^{\text{exp}}(k) = \sigma_{MM}^2 \frac{a^3}{\pi^2(1+k^2 a^2)^2}, \quad (2.105)$$

$$\Phi^{\text{fractal}}(k) = \sigma_{MM}^2 \frac{a^3 \Gamma(\nu + 3/2)}{\pi^{3/2} \Gamma(\nu) (1+k^2 a^2)^{\nu+3/2}}. \quad (2.106)$$

The quantity a is the correlation length and a measure of the typical size of medium heterogeneities. In the fractal distribution, Γ is the Gamma function and the so-called Hurst exponent ν is an additional model parameter describing whether neighboring heterogeneities belong to the same phase (persistence) or to different phases (anti-persistence) (Feder, 1988). For the above mentioned correlation functions, the integral in equation 2.97 can be solved in closed form

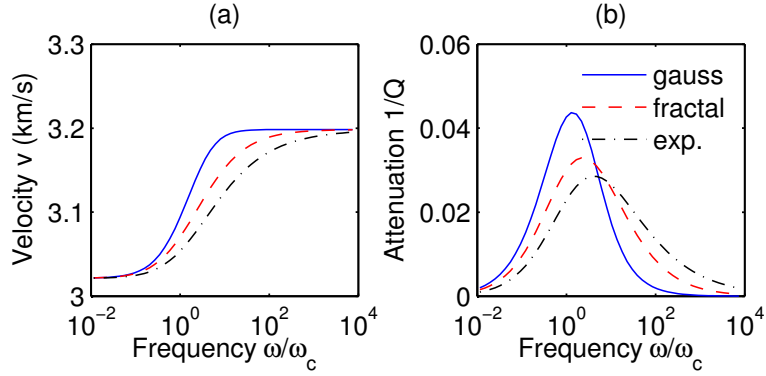


Figure 2.10: CRM model for partial saturation. Velocity dispersion and attenuation are given as a function of frequency for models with the same correlation length but different correlation functions: Gaussian, fractal ($\nu = 0.8$), exponential.

one obtains according to Toms et al. (2007) and Müller et al. (2008)

$$\xi^{\text{gauss}} = \frac{k_d^2 a^2}{(\imath k_d a - 1)^2}, \quad (2.107)$$

$$\xi^{\text{exp}} = \frac{k_d^2 a^2}{2} \left[1 + \frac{\imath k_d a}{2} \sqrt{\pi} \exp\left(\frac{k_d^2 a^2}{4}\right) \operatorname{erfc}\left(-\frac{\imath k_d a}{2}\right) \right], \quad (2.108)$$

$$\xi^{\text{fractal}} = 2\nu (k_d a)^2 {}_2F_1\left([1, \nu + 1], \frac{1}{2}, -k_d^2 a^2\right) + 2\imath \pi^2 k_d^3 \Phi^{\text{fractal}}. \quad (2.109)$$

The last equation involves the Gaussian hypergeometric function of complex argument ${}_2F_1$ (Gradshteyn and Ryzhik, 1983), a definition is given in appendix C.5.

2.9 Discussion

In the literature, it is sometimes argued that the Biot model as characterised by the dispersion relations for the three wave modes 2.54 and 2.61 is incomplete in the sense that it underestimates the dispersion in saturated porous rocks. The squirt-flow model of Mavko and Jizba (1991) has been suggested to include the effects of microscopic heterogeneity on velocity dispersion. Indeed it is true that real rocks always possess some heterogeneity on various scales.

It shall be pointed out here, that in contrast to the squirt-flow, the wave-induced mesoscopic flow models presented in section 2.8 are not extensions of the Biot theory but they are based on the quasistatic approximation of Biot's governing equations. Therefore, they can be considered as special solutions of

the Biot equations under heterogeneous conditions. A numerical model – such as presented in the subsequent chapter – for solving the Biot equations for heterogeneous systems is consequently a valuable tool for testing various theoretical approaches.

Comparing the effects of the Biot global flow and the mesoscopic flow models, one finds that the latter generally produce considerably higher dispersion and attenuation. In addition to that, at seismic frequencies, the Biot global flow effect is usually insignificant. There is, however, an impact of the Biot global flow on the dispersion of poroelastic waves at ultrasonic frequencies.

In this chapter, the radiation characteristics of different sources in porous media were not included, since in the following this thesis will focus on wave propagation effects rather than on source characteristics. Instead, it is referred to the review article of Karpfinger (2006) or the textbooks of Bourbié et al. (1987) and Carcione (2001).

It is natural that mathematical models of linear poroelastic wave propagation are not universally applicable. For example, it is well known that Earth materials with microcracks may close under compressive stresses, which leads to hysteretical and non-linear material behaviour (Johnson et al., 1996). Another example is the effect of partial saturation, where the wave-induced fluid flow theory predicts zero attenuation of the shear waves. The laboratory observation depicted in Figure 1.9, however, shows saturation- and frequency dependent shear wave attenuation in partially saturated rock, which obviously cannot be explained directly by mesoscopic flow models. Therefore, theoretical models as well as numerical results must always be accomplished with corresponding laboratory experiments in order to ensure that all the relevant effects are included in the mathematical description.

Chapter 3

Numerical methods

General solutions for waves and diffusion processes in porous media are available for simple cases. For example, if homogeneity and isotropy is assumed, Green's functions are known and are used to calculate the response of a poroelastic medium to external forces, fluid injections or seismic moments. Another class of theoretical results is used to calculate the effective behaviour of heterogeneous porous media. Here, it is commonly assumed that the wavelength is much larger than the characteristic size of the heterogeneity. For the evaluation of fluid flow effects on the elastic properties of a heterogeneous porous medium, assumptions are necessary about the geometry of the heterogeneity. For most complex geometries, the theoretical solutions are not presented in closed form but require the numerical evaluation of integrals (like e. g. in Dutta and Odé, 1979).

For cases when theoretical solutions are not available, numerical methods provide means to find approximate solutions to a given poroelastic problem. On the basis of an appropriate mathematical model, a numerical model is obtained by discretising the governing equations. The resulting system of algebraic equations is then solved using a computer system and the discrete solution is interpreted as an approximate solution of the physical problem.

The numerical method most frequently applied in geophysical research for wave propagation modelling is the finite-difference (FD) method (e. g. Boore, 1972; Virieux, 1986; Bohlen, 2002). The basic concept of this method is the approximation of the differential operators by finite differences on a discrete mesh in space and time. Therefore, an approximate solution is obtained at the mesh grid points. The finite-element (FE) method is also widely used for solving wave propagation problems, in particular, if the modelling domain has a complex shape (Smith, 1975; Cohen, 2002). While the FD method discretises the differential operators, the FE method discretise the solution space and applies the differential operators to a set of ansatz functions. The advantage of the FE method is its potential to better resolve small-scale geometries by using triangular or tetrahe-

dral elements instead of uniform grids. Complex boundaries can be represented more accurately this way. If trigonometric functions are used to form the solution space one also speaks of spectral elements instead of finite elements.

It is the purpose of this chapter to develop a numerical FD scheme for solving the dynamic Biot equations and to analyse its accuracy and stability properties. The section is based on corresponding publications (Wenzlau et al., 2007; Wenzlau and Müller, 2008). In a second part of this chapter, a short introduction is given to the numerical FE solution of the quasistatic Biot equations. For this type of problems, the commercial software package “Abaqus” is available and the aim of the section on FE modelling is to explain the theoretical background of the Abaqus package for poroelastic rheology.

3.1 Modelling poroelastic wave propagation using the FD method

The earliest publications on the finite-difference method for solving the dynamic Biot equations appeared in the 1990s (Hassanzadeh, 1991; Zhu and McMechan, 1991; Dai et al., 1995). These contributions explain the derivation of numerical schemes and give several 2-D examples related to seismic exploration. However, the proper use of the numerical codes requires the analysis of the relevant scales in order to reveal the actual poroelastic effects (Gurevich, 1996).

Carcione and Quiroga-Goode (1995) remark that the existence of the slow P -wave introduces a scale to the general solution of the Biot equations that is very different from the scales of the fast P -wave and the S -wave. By comparing the magnitudes of the eigenvalues given in equation 2.54, they state that at low frequencies, i. e. at frequencies much below than the Biot frequency ω_B , the Biot equations are stiff. This means that the wave propagation phenomena related to the fast wave modes occur on spatial scales that are much larger than the spatial scale of the diffusion process associated with the slow P -wave. Resolving the small diffusion scale as well as the large propagation scale is computationally very expensive. Since it is the scale resolution is a crucial factor for the accuracy of the scheme, the stiffness problem will be discussed in section 3.1.5. An important contribution on numerical stability of poroelastic FD solvers has been made by Masson and Pride (2007), their results are reviewed in section 3.1.4. As a consequence of the computational demand of large FD simulations, the development of codes has begun that make use of parallel algorithms (Aldridge et al., 2004; Sheen et al., 2006). This is particularly necessary, if the simulations are done in 3-D.

In this thesis, the discretisation of the Biot equations is based on the velocity-stress formulation, an approach suggested for elastic wave propagation by Virieux

(1986). This means that instead of the displacements, corresponding velocities are used as field variables. Setting

$$v_i = \dot{u}_i, \quad (3.1)$$

$$q_i = \dot{w}_i \quad (3.2)$$

and using the low-frequency approximation for the viscodynamic operator Y (equation 2.22), the two wave equations of second order 2.43 and 2.44 are rewritten as a set of four evolution equations of first order

$$\dot{v}_i = (\rho^m \rho^b - \rho^f \rho^f)^{-1} (\rho^m \tau_{ij,j} + \rho^f p_{,i} + \rho^f b q_i), \quad (3.3)$$

$$\dot{q}_i = (\rho^m \rho^b - \rho^f \rho^f)^{-1} (-\rho^f \tau_{ij,j} - \rho^b p_{,i} - \rho^b b q_i), \quad (3.4)$$

$$\dot{\tau}_{ij} = \mu (v_{i,j} + v_{j,i}) + (\lambda_u v_{i,i} + \alpha M q_{i,i}) \delta_{ij}, \quad (3.5)$$

$$\dot{p} = -\alpha M v_{i,i} - M q_{i,i}. \quad (3.6)$$

The new field variables are the total velocity v_i , the filtration velocity q_i as well as the stress tensor and the pore pressure τ_{ij} and p . For the derivation of a numerical FD scheme, approximations for the temporal and spatial differential operators are now introduced.

3.1.1 Time discretisation

If the linear system 3.3–3.6 is written in compact matrix form as

$$\partial_t \mathbf{v} = \mathbf{A} \partial_j \mathbf{v} + \mathbf{B} \mathbf{v}. \quad (3.7)$$

Writing equation 3.7 in a more elaborate way while abbreviating matrix entries with an asterix as

$$\partial_t \begin{pmatrix} v_i \\ q_i \\ \tau_{ij} \\ p \end{pmatrix} = \left(\begin{array}{c|cc} & * & * \\ & * & * \\ \hline * & * & \\ * & * & \end{array} \right) \partial_j \begin{pmatrix} v_i \\ q_i \\ \tau_{ij} \\ p \end{pmatrix} + \left(\begin{array}{c|c} * & \\ \hline * & \end{array} \right) \begin{pmatrix} v_i \\ q_i \\ \tau_{ij} \\ p \end{pmatrix}, \quad (3.8)$$

one observes that the structure of the coefficient matrix \mathbf{A} has a form that makes it advantageous to introduce a discretisation that is staggered time. Therefore, time-discrete fields for stresses and velocities are

$$v_i^{n+1/2} = v_i(\mathbf{x}, t = (n + 1/2)\Delta_t), \quad (3.9)$$

$$q_i^{n+1/2} = q_i(\mathbf{x}, t = (n + 1/2)\Delta_t) \quad (3.10)$$

$$(3.11)$$

and that for the stresses and pore pressure are

$$\tau_{ij}^n = \tau_{ij}(\mathbf{x}, t = n\Delta_t), \quad (3.12)$$

$$p^n = p(\mathbf{x}, t = n\Delta_t). \quad (3.13)$$

In order to derive the FD scheme, the temporal derivatives in equations 3.3–3.6 are replaced by the second order discrete time differential operator

$$D_t \phi^n = \frac{1}{\Delta_t} (\phi^{n+1/2} - \phi^{n-1/2}) \quad (3.14)$$

and solving for the variable fields at the new time step yields

$$v_i^{n+1/2} = v_i^{n-1/2} + A \tau_{ij,j}^n + B p_i^n + C (q_i^{n+1/2} + q_i^{n-1/2}) / 2 \quad (3.15)$$

$$q_i^{n+1/2} = D q_i^{n-1/2} + E \tau_{ij,j}^n + F p_i^n \quad (3.16)$$

$$\tau_{ij}^n = \tau_{ij}^n + G (v_{i,j}^{n+1/2} + v_{j,i}^{n+1/2}) + (H v_{i,i}^{n+1/2} + I q_{i,i}^{n+1/2}) \delta_{ij} \quad (3.17)$$

$$p^n = p^n + J v_{i,i}^{n+1/2} + J q_{i,i}^{n+1/2}. \quad (3.18)$$

Here, an arithmetic average for the filtration velocity q_i at the intermediate time step n has been used, written as

$$\bar{q}_i^n = 1/2 (q_i^{n-1/2} + q_i^{n+1/2}). \quad (3.19)$$

The time stepping consists of the following steps:

1. Velocity update at time step $n + 1/2$, beginning with the filtration velocity.
2. Introduction of body forces that act as a momentum source. For a description see section 3.1.3.
3. Stress and pore pressure update at time step n .
4. Introduction of sources to the stress tensor and pore pressure. For a description see section 3.1.3, as well.

The six velocity update coefficients A–F in equations 3.15–3.16 and the stress update coefficients G–J in equations 3.17–3.18 are given by

$$A = (\rho^m \Delta_t) / r^2 \quad (3.20)$$

$$B = (\rho^f \Delta_t) / r^2 \quad (3.21)$$

$$C = (\rho^f b \Delta_t) / r^2 \quad (3.22)$$

$$D = (2r^2 - \rho^b b \Delta_t) / (2r^2 + \rho^b b \Delta_t) \quad (3.23)$$

$$E = -(\rho^f \Delta_t) / (r^2 + \rho^b b \Delta_t) \quad (3.24)$$

$$F = -(\rho^b \Delta_t) / (r^2 + \rho^b b \Delta_t) \quad (3.25)$$

$$G = \mu \Delta_t \quad (3.26)$$

$$H = \lambda_u \Delta_t \quad (3.27)$$

$$I = \alpha M \Delta_t \quad (3.28)$$

$$J = -M \Delta_t, \quad (3.29)$$

where the determinant of the density matrix has been abbreviated as

$$r^2 = \rho^b \rho^m - \rho^f \rho^f. \quad (3.30)$$

Since the new timestep is calculated from the preceding and therefore known time step, the scheme is explicit. The scheme is second order, i. e. the discretisation error is proportional to the square root of time step Δ_t . By decreasing the time step, an improved approximation of the spatial derivatives is obtained and in the limit, the scheme is consistent with the governing equations of dynamic poroelasticity. The time step size plays a crucial role for the stability of the scheme, as discussed in section 3.1.4.

3.1.2 Calculation of spatial derivatives

In order to spatially discretise the governing equations, staggered grids are introduced for all field variables and the spatial derivatives are approximated by discrete operators. If a spatial grid is defined by

$$\phi_{i,j,k} = \phi(x = i\Delta_x, y = j\Delta_y, z = k\Delta_z, t), \quad (3.31)$$

the standard expression of finite-difference operators in the x -direction is written as

$$D_x^{(n)} \phi = 1/\Delta_x \sum_{m=0}^{n/2-1} a(m) (\phi_{i+m+1/2,j,k} - \phi_{i-m-1/2,j,k}). \quad (3.32)$$

The maximum number of different coefficients $a(m)$ depends on the integer n , which is referred to as the order of the operator since

$$\partial_x \phi = D_x^{(n)} \phi + \mathcal{O}(n). \quad (3.33)$$

Table 3.1: Finite-differences coefficients for 2nd, 4th and 8th order differentiation.

n	$a(1)$	$a(2)$	$a(3)$	$a(4)$	$a_{\text{sum}} = \sum_{i=1}^n a(i) $
2	1				1.0000
4	$\frac{27}{24}$	$-\frac{1}{24}$			1.1667
8	$\frac{1225}{1024}$	$-\frac{1225}{1024 \times 15}$	$\frac{1225}{1024 \times 125}$	$-\frac{1225}{1024 \times 1715}$	1.2863

Examples for second, fourth and eighth order operators are given in Table 3.1 and Figure 3.1 shows a graphical representation of the coefficients. As observed from Figure 3.1c, the higher order FD operator provides a more accurate estimate of the spectral behaviour of the differential operator ∂_x . However, due to its length, the numerical evaluation requires more computations than that of the lower order operator.

If the velocity-stress formulation is applied as a basis for FD schemes, the standard grid staggering method is described by Levander (1988) and Virieux (1986). In this case, the derivatives are calculated along the coordinate axes. A 2-D example of such a grid is shown in Figure 3.2a. Actually, four different grids are applied to represent the positions of all field variables. Isotropic components of the stresses and strains are located in the centre of a control volume, referred to as the p -grid. Horizontal components of the velocity vector are stored on the u -grid, appearing horizontally staggered with respect to the p -grid. Vertical components are staggered vertically on the v -grid and finally, the shear components – requiring horizontal derivatives of vertical velocity components – are stored on the τ -grid. On every grid, certain material properties are required to link e. g. the strains and stress components. Densities are stored on the two velocity grids, while the elastic moduli are required on the p - and τ -grids. The consequence is that material properties have to be averaged according to the position where they are required. In particular, it is known in the case of elastic waves that the shear modulus needs to be averaged harmonically in order to ensure stable results (Bohlen, 2002).

A modified staggering scheme has been proposed for elastic and viscoelastic wave equation modelling by Saenger et al. (2000). The idea is to apply rotated operators such that the FD approximation is calculated first along diagonal lines and then in a second step the derivatives along the coordinate axes are obtained

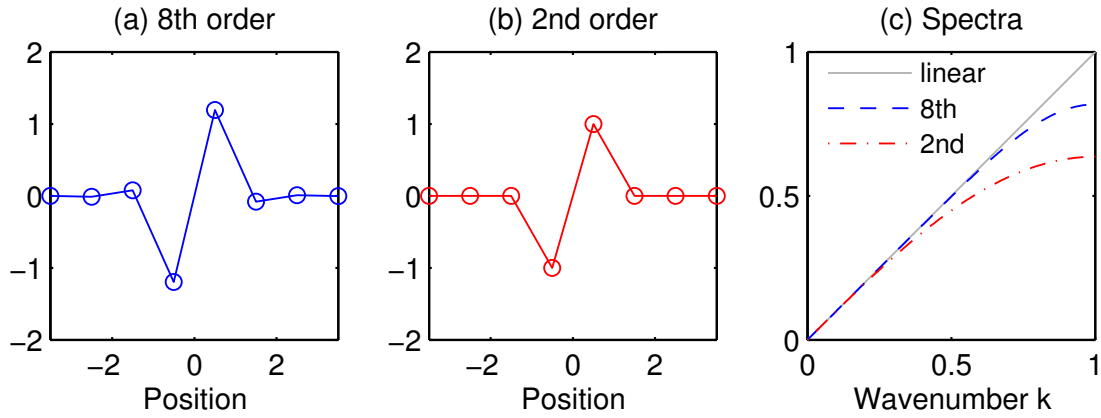


Figure 3.1: Finite-difference operators for (a) 8th order and (b) second order approximations. Amplitude spectra of the discrete operators are given in (c). Note that the optimal spectrum is a linear function, since $|\mathcal{F}\{\partial_i\}| = k$.

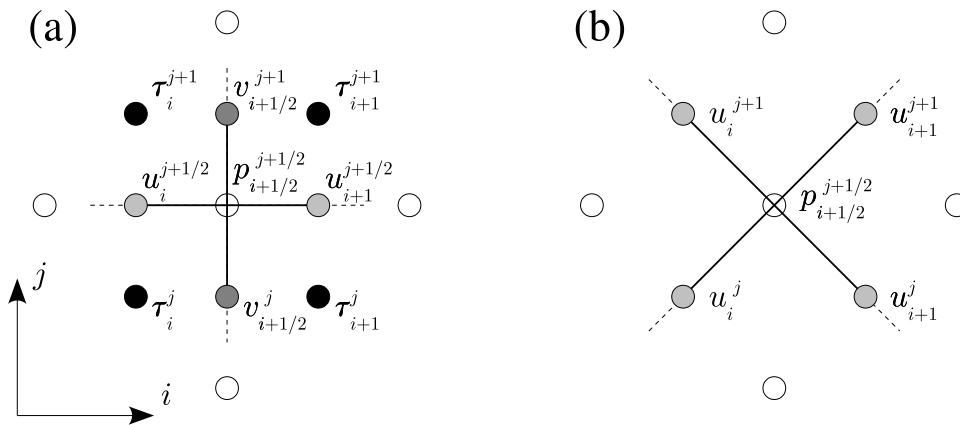


Figure 3.2: Stencils of finite-differences formulations. (a) Standard staggered grid, with normal stresses stored on the p -grid, shear stresses stored on the τ -grid; horizontal and vertical velocity components are stored on separate the u - and v -grid respectively. (b) Rotated staggered grid, with all velocity components stored at the same gridpoints and therefore only one grid for all stress components.

by a linear transformation. As an advantage of this method, the different velocity grids and the grids for the strains and stresses coincide, respectively, such that only one velocity and one stress grid is required. This reduces the need for averaging of material properties: only densities are averaged over the control volume. It has been found in the case of elastic and viscoelastic waves that this so-called rotated staggered grid approach enhances the stability properties of the underlying FD scheme in the presence of high material contrasts (Saenger et al., 2000). In Figure 3.2b, a sketch of the rotated staggered grid is shown in comparison to the standard staggered grid. In fact, the u - and v -grids coincide as well as the p - and the τ -grid.

3.1.3 Boundaries and sources

Typically, seismic sources are represented by a spatio-temporal distribution of body forces (Aki and Richards, 1980). These are easily included in the numerical scheme by adding an acceleration term to the evolution equations of the total velocity v_i . Alternatively, stress sources are added to evolution equations of the stress tensor components and to the pore pressure in order to simulate pure dilatational forces (source to mean stress and/or pore pressure) or pure shear forces (source to the shear stress). For convenience, a source distribution parameter q_p is introduced to distinguish between pressure sources acting on the solid matrix and on the pore fluid. The sources to stress and pore pressure are then written

$$S_{\tau_{ij}} = S_0(1 - q_p), \quad (3.34)$$

$$S_p = S_0 q_p, \quad (3.35)$$

where S_0 is a time-dependent source function. Obviously, a source parameter $q_p = 0$ describes a pure dilatational excitation of the solid frame, while $q_p = 1$ indicates a pure pore pressure source.

The numerical treatment of the domain boundaries is also straightforward. Dirichlet conditions are implemented by assigning in every time step a given, time-dependent value to the velocity fields. E. g. setting the filtration q_i velocity to zero corresponds to hydraulic sealing of the boundary, this is referred to as undrained boundaries. A confining boundary is obtained by setting the total velocity v_i to zero.

Additional boundary conditions are used to mimic waves propagating within an unbounded domain. In this case, the aim is to avoid reflections from the domain edges. If plane waves are considered with a wave vector parallel to the lateral boundaries, it is often possible to use periodicity conditions for all field variables. This is done by assigning to the left domain edges the values of the right domain edge and vice versa. If this periodic boundaries are not applicable,

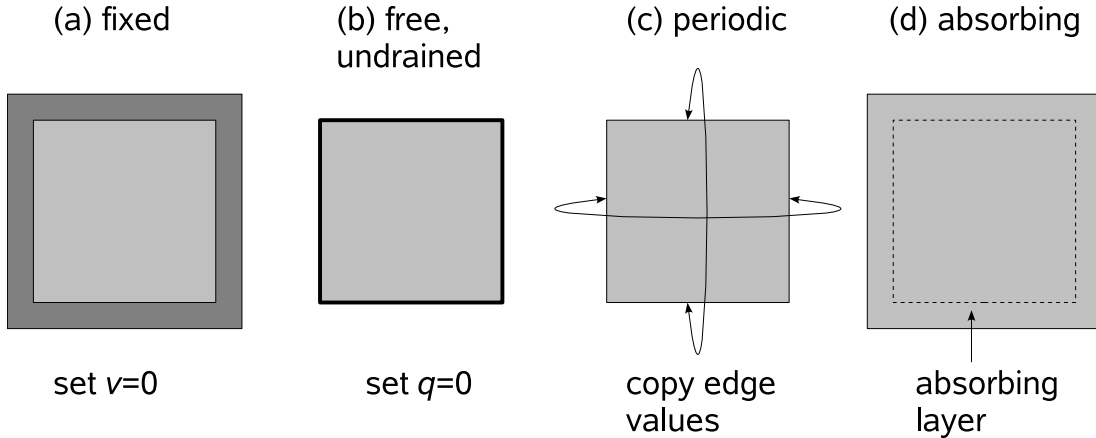


Figure 3.3: Examples of boundary conditions for poroelastic wave simulation.

absorbing boundaries are used in order to attenuate all signals approaching the domain edges, analogous to the elastic case described e. g. in Bohlen (2002). Within an absorbing layer the field variables are multiplied with static absorption coefficients that are exponentially dependent on the distance from domain edge. By adequately choosing the width of the absorbing layer and the decay exponent of the absorption coefficients, reflections of artificial boundaries are significantly reduced.

Four examples of boundary conditions are given in Figure 3.3. Subfigures a and b represent Dirichlet conditions for total and filtration velocity, respectively, while periodic and absorbing boundaries are sketched in subfigures c and d.

3.1.4 Stability

The explicit time stepping scheme (equations 3.15–3.18) can be presented in the short form

$$\mathbf{u}^{n+1} = \mathbf{A}\mathbf{u}^n, \quad (3.36)$$

with the field variable vector $\mathbf{u} = (v_x, v_y, q_x, q_y, \tau_{xx}, \tau_{yy}, \tau_{xy}, p)$ and the discrete matrix \mathbf{A} containing material parameters, time step size and discrete spatial operators. By analysing the properties of \mathbf{A} , information can be obtained about the accuracy and stability of the scheme. Standard von Neumann type analysis states that if the spectral radius of \mathbf{A} is smaller or equal to 1, the explicit scheme is stable. In 2-D, eigenvalues of a 8×8 -matrix must be computed analytically, which is not possible in the general case. However, for the poroacoustic ($\tau_{xy} = 0$) and frictionless ($b = 0$) case, analytical expressions for the eigenvalues are available. In the 1-D case, \mathbf{A} reduces to a 4×4 matrix, and in order to evaluate the eigenvalues, an equation of 4th order has to be solved. For a similar scheme, this has been

done by Masson et al. (2006).

The main finding is that the well-known stability requirement for elastic wave propagation holds also for the poroelastic case: the time step must be sufficiently small that the fastest wave mode travels less than the distance between two grid points. This relationship is

$$\Delta_t < \frac{\Delta_x}{a_{\text{sum}} c_{\text{max}}}, \quad (3.37)$$

where c_{max} is the maximum phase velocity and the coefficient $a_{\text{sum}} \geq 1$ is the sum of the absolute FD coefficients, see Table 3.1. A safe estimate of c_{max} is given by equation 2.54 by setting friction to zero. In this case one has

$$c_{\text{max}} = c_{P1} = \sqrt{2} \left[\text{tr} \mathbf{D} - (\text{tr}^2 \mathbf{D} - 4 \det \mathbf{D})^{1/2} \right]^{-1/2}, \quad (3.38)$$

where \mathbf{D} is given in equation 2.53. The analysis of this formula reveals that the existence of an inverse density matrix \mathbf{P} is necessary and consequently, the determinant $\det \mathbf{P} = r^2$ must be positive and larger than zero. This condition is also related to the appearance of the determinant r^2 in the denominator of the update coefficients, as defined in equations 3.20–3.29. As a consequence, the phase velocity of the compressional wave modes have a pole at $\det \mathbf{P} = 0$ implying that at

$$\frac{\nu}{\phi} \leq \frac{\rho^f}{\rho^b}, \quad (3.39)$$

velocities increase without bounds and the scheme becomes unconditionally unstable. In the limit of large tortuosity parameters, equation 3.38 approaches the quasistatic limit with $c_{\text{qs}} = \sqrt{H/\rho^b}$.

In Figure 3.4, normalised maximum timestep Δ_t is given as function of normalised tortuosity ν . The solid blue line indicates the strictest stability criterion 3.38 that applies if no friction between fluid and solid matrix is taken into account. For increasing friction, the condition is relaxed, and the domain of stability, indicated by a grey shaded area is enlarged. However, the condition 3.39 must always be respected even for $b \rightarrow \infty$, when the size of the stability domain is maximum (dashed red line). A more detailed discussion of stability is given in Masson et al. (2006).

Note that inequality 3.39 is usually not crucial in homogeneous porous rock. For a water-saturated porous sandstone with $\phi = 20\%$ porosity and tortuosity $\nu = 2$, one obtains for $\frac{\nu \rho^b}{\phi \rho^f}$ a value of 4.3 which is approximately at the very right edge of Figure 3.4. The value of the stability limit is 0.97 which is 3% below the limit estimated from equation 3.37 by using the quasistatic approximation $c_{\text{max}} = c_{\text{qs}}$. The situation changes for inclusions with high porosity ϕ and a tortuosity ν close to one. E. g. choosing $\phi = 0.9$ and $\nu = 1.1$ yields $\frac{\nu \rho^b}{\phi \rho^f} \approx 1.44$ where time stability limit is 0.54. Therefore, the time step has to be chosen about half as large as

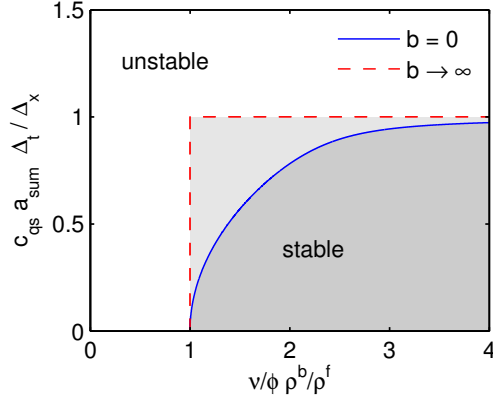


Figure 3.4: Domain of stability, limited by two conditions 3.37 and 3.39. In the frictionless case ($b = 0$), shaded in dark grey, the stability domain is smaller than in the opposite case ($b \rightarrow \infty$), shaded in light grey. Adapted from Masson et al. (2006).

for normal sandstone. A combination of 100% porosity and tortuosity 1 yields unconditionally unstable results, as discussed later in section 4.4.

3.1.5 Accuracy

The accuracy of the computation is governed by the effects of numerical dispersion. The dispersion errors depend on the order of the spatial FD approximation and the number of gridpoints per smallest wavelength. They accumulate with increasing propagation distance and therefore, depending on the size of the computational domain as well as the desired accuracy, a sufficiently fine grid spacing Δ_x is necessary. In poroelasticity, the slowest wave, being consequently critical for dispersion errors, is the slow P -wave. At seismic frequencies this wave mode is associated with a diffusion process. One possibility to quantify the scale of this diffusion process is the diffusion length introduced earlier in section 2.7

$$\lambda_D = \sqrt{\frac{D}{\omega}}, \quad (3.40)$$

with D being the coefficient of hydraulic diffusivity. Note that the hydraulic diffusivity is usually a very small quantity, resulting in a very small diffusion length that is considerably smaller than the wave lengths of the fast compressional and shear waves. A system that responds on very different time scales and spatial scales, is called stiff (Carcione and Quiroga-Goode, 1995). Since the system response is described by its eigenvalues it is sufficient to analyse the dispersion relation 2.54 of plane waves in poroelastic media. Plotting the eigenvalues of the governing system in the complex plane reveals their large difference in amplitude, as shown in Figure 3.5.

Quantifying the stiffness by

$$\text{stiffness} = \frac{\lambda_{P_f}}{\lambda_D} = \frac{c_{P_f} \omega^{-1}}{\sqrt{D \omega^{-1}}} = \sqrt{\frac{c_{P_f}^2}{D \omega}} \quad (3.41)$$

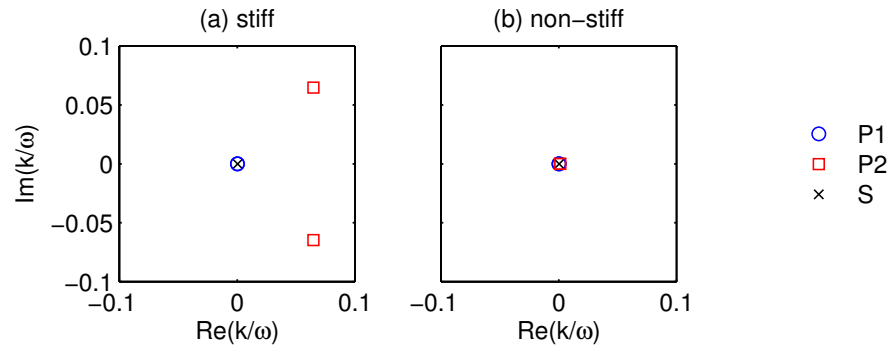


Figure 3.5: System eigenvalues, i. e. complex slownesses, of fast and slow P -waves as well as shear waves illustrating the stiffness of the governing equations. For a water-saturated sandstone at seismic frequencies (a) the slowness amplitudes are very different while at ultrasonic frequencies (b) they are closer to each other.

reveals that the problem becomes stiffer the lower the frequency is. Using the Biot frequency ω_B given in equation 2.21, this is also expressed by the dimensionless Deborah number $De = \omega/\omega_B$ used in rheology (Reiner, 1964). For small Deborah numbers we again obtain stiff behavior of the equations, resulting in a high computational effort, since small-scale diffusion processes have to be resolved, while the scale of the fast propagating wave is orders of magnitude larger. In the same way, the time increment has to be chosen according to the stability requirement 3.37, while the very slow diffusion process needs a long time to evolve.

3.1.6 Parallelisation

The computational effort for wave simulations increases linearly with increasing size of the problem, i. e. with (1) the number of total grid points, (2) the number of the simulated time steps and (3) the length of the spatial FD operator. As discussed in the previous sections, the accuracy requirements mainly control the choice of the spatial sampling while the time step size is usually chosen such that stable results are obtained.

The availability of parallel computing facilities makes it possible to simulate wave propagation experiments in larger domains and with an increased spatial resolution. In order to exploit the computing facilities, the numerical code needs to be distributed to several communicating processes. This parallelisation is done by the domain decomposition technique, implying that the computational domain is subdivided into smaller cells, each of which is assigned to a particular process. In order to propagate signals from one cell to an adjacent cell, communication buffers are located at the edges of each local cell, as shown in Figure 3.6. The communication is implemented using the message passing interface (MPI).

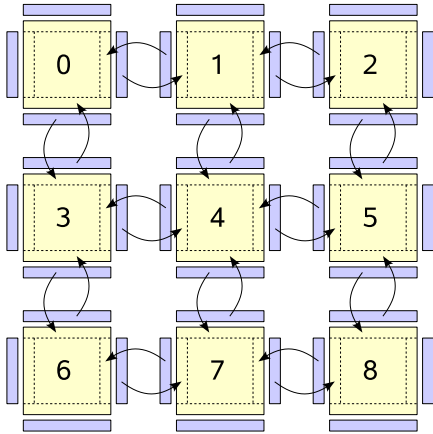


Figure 3.6: Sketch of the parallelisation by domain decomposition. Subdomain cells are surrounded by buffers, arrows indicate communication between different processes.

Communication via MPI is required after each update step and therefore twice in a time step. Preferably, the communication time should be as small as possible if compared to the actual time needed to compute the time update of the field variables. Unfortunately, the fraction of communication runtime rises with the degree of parallelisation and therefore, the number of processes involved in a particular simulation is limited. The ability of a numerical code to reduce the total wallclock time when more processes are involved in the simulation is called scalability. A parallel performance test is given later in section 4.5.

3.2 Modelling quasistatic consolidation using the FE method

In physics and engineering, the method of finite elements is widely used for solving mechanical problems due to its flexibility to handle complex geometries. The principle of the method is based on the partitioning of the problem domain using elements of simple geometry, e. g. triangles in the two-dimensional case as shown in Figure 3.7. Within each element, the solution is interpolated by polynomial basis functions where the interpolation coefficients are n nodal values of the field variables. The discretised governing equations are then multiplied with n weighting functions and integration is performed over the element volume V , yielding a set of $n \times n$ algebraic equations for the unknown nodal values. The approximate solution fulfils Galerkin's principle that states the minimisation of the weighted residuals. Therefore, the finite-element method is a special case of the Galerkin method (Zienkiewicz, 1977).

The aim of this section is to give an overview of the FE method for quasistatic poroelastic problems as described e. g. by Wang (2000) and Wang and Anderson (1982). I follow their presentation and account for the particularities of the com-

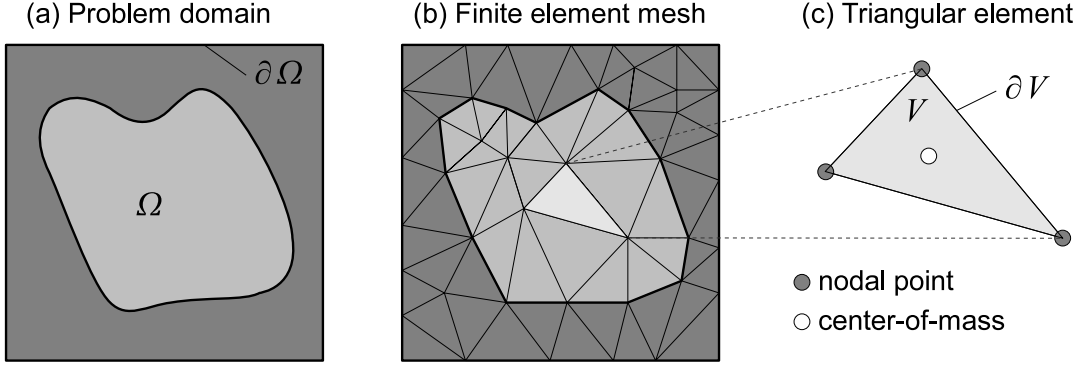


Figure 3.7: Example of a finite-element mesh (b) constructed on the basis of triangular elements (c) and resolving a problem domain of complex shape (a).

mercial Abaqus FE package (Abaqus, Inc., 1998). Abaqus is a flexible tool for a variety of poroelastic problems including partially saturated rheologies, different laws of fluid flow, buoyancy effects, matrix anisotropy and plastic deformation. Since these options are beyond the scope of this work, the derivations are restricted to isotropic poroelasticity such as described by equations 2.69 and 2.70. Please note that the rheology as implemented in the Abaqus porous elastic model is generally non-linear. For the reduction of the material parameters to the linear case of small deformation see appendix D.

3.2.1 Spatial discretisation by the Galerkin method

Under the absence of body forces, the equilibrium condition within an element e is generally written as the vanishing sum of internal and external forces F_i^i and F_i^e

$$F_i^i + F_i^e = \int_V \tau_{ij,j} dV + \int_{\partial V} t_i dS = 0, \quad (3.42)$$

where t_i is the traction vector acting on the element boundary ∂V . Applying the principle of virtual work leads to the variational or weak formulation of equilibrium: the variational sum of internal and external energies is zero. With the virtual strain $\delta\varepsilon_{ij}$ within V and the virtual displacement at the boundary δu_i one writes

$$\delta E^i + \delta E^e = \int_V \tau_{ij} \delta\varepsilon_{ij} dV + \int_{\partial V} t_i \delta u_i dS = 0. \quad (3.43)$$

Now, in order to derive a discrete approximation of equation 3.43, the virtual displacement and strain are substituted by interpolation functions

$$\delta u_i = \sum_{k=1}^m N_i^k U^k. \quad (3.44)$$

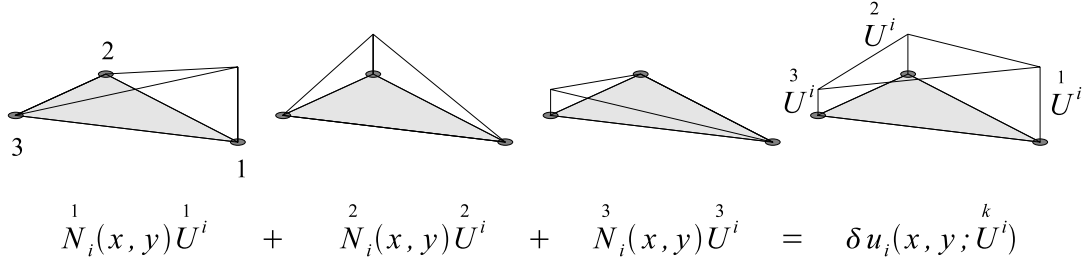


Figure 3.8: The virtual displacement δu_i within a triangular element is approximated by three linearly independent basis functions N_i .

Here, N_i are m basis functions that depend on the position within the element, U^i are interpolation coefficients and commonly the unknown nodal values of the element. E. g. a plane linear triangular element (see Figure 3.8) uses 3 independent interpolation functions, while bilinear rectangular elements and tetrahedral elements use $m = 4$ functions.

For the virtual strain one writes

$$\delta \varepsilon_{ij} = \frac{1}{2} (\delta u_{i,j} + \delta u_{j,i}) = \sum_{k=1}^m \frac{1}{2} \left(N_{i,j}^k U^k + N_{j,i}^k U^k \right) = \sum_{k=1}^m \beta_{ij}^k U^k \quad (3.45)$$

and this equation makes clear how the spatial differentiation is passed on from the field variables to the known basis functions. If the approximations 3.44 and 3.45 are introduced into the virtual energy equation 3.43, an algebraic equation is obtained for the m nodal unknowns. In order to derive m independent equations for all unknowns, the virtual energy equation is multiplied successively with m so-called weighting functions. In the finite-element method, the basis functions are used for this purpose which is referred to as isoparametric ansatz or Ritz ansatz (Zienkiewicz, 1977). This approach provides a $m \times m$ linear system of algebraic equations

$$\int_V N_i^l \sum_{k=1}^m \tau_{ij}^k \beta_{ij}^k U^j dV + \int_{\partial V} N_i^l \sum_{k=1}^m t_i^k N_i^k U^i dS = 0 \quad (3.46)$$

representing on the one hand side the internal energy in the form of a volume integral and work done by external forces in the form a surface integral.

A global system is obtained by summing up the contributions from individual elements, which is referred to as assembling. The resulting system is formally the same as that used in elastic finite-element descriptions. There is, however, the particularity of poroelastic FE modelling that the stress tensor τ_{ij} depends not only on the displacement field but also on the pore fluid flow as described by the coupled diffusion equation 2.72. Therefore, a simultaneous solution of equilibrium

and pore pressure diffusion is necessary to describe the time-dependent stress field (Abaqus, Inc., 1998).

The discretisation of the diffusion equation is carried out analogously to that of the equilibrium equations: the pore pressure field is approximated using the same basis functions as for the displacements; multiplication with isoparametric weighting functions and integration over one element provides a local system of algebraic equations that is assembled to the global system by summing contributions from every element. For details, it is referred to the literature (Wang, 2000; Abaqus, Inc., 1998, and references therein).

3.2.2 Boundaries and sources

Initial conditions and boundary conditions have to be specified to constrain the solution of a given poroelastic problem. Within the context of this work, the initial fields are assumed to be in equilibrium, i. e. all fields are set to zero throughout the model domain.

Boundary conditions are specified either by constraining the relevant degrees of freedom at the model edges, e. g. normal displacement, or by specifying a (potentially time-dependent) traction vector. If the displacement components or the traction vector are zero at the model boundary, this leads to a vanishing of the corresponding virtual work in the global energy budget.

Although it is possible to include volume forces such as gravity or point mass sources such as fluid injections within the model domain, a discussion is passed on since in the subsequent chapter, the focus is on consolidation processes that are generally driven by externally applied forces.

3.2.3 Time integration and solution of the linear system

In contrast to static problems in elasticity, quasistatic formulations as described by the coupled diffusion process in poroelasticity are time-dependent. The solution of such problems therefore requires an approximation of the temporal behaviour of the field variables. This is done by introducing a backward FD operator such that the time derivative is written at the new time step $t + \Delta_t$

$$\phi_{t+\Delta_t} = \phi_t + \Delta_t \dot{\phi}_{t+\Delta_t}. \quad (3.47)$$

The resulting numerical scheme is implicit implying that a matrix inversion is required within each time step. This entails a higher computational cost if compared to explicit schemes such as described in section 3.1.1. The main advantage of implicit schemes, however, is their better stability behaviour. Actually, there is no restriction on the time step size to ensure stable results and the choice of the number of required time steps can therefore be drastically reduced as long

as the physical time scales are properly resolved. This means that for consolidation processes, being typically characterised by strong spatio-temporal changes of the stress and displacement fields at the beginning of the simulation, the time step is short at the beginning and is then augmented during the simulation when pore pressure equilibration takes place, and the stress and strain fields become smoother. In practice, the time step size is determined automatically such that the increment in pore pressure does not exceed a specified value during each time step.

The result of the implicit FE discretisation is a large and sparse linear algebraic system with a size that is proportional to the number of elements as well as to the number of nodal points per element. With the system matrix \mathbf{A} , the vector of unknown nodal values \mathbf{u} and the source vector \mathbf{b} the linear system is

$$\mathbf{A}\mathbf{u} = \mathbf{b}. \quad (3.48)$$

This system is solved using the conjugate gradient method that minimises the function

$$f = \frac{1}{2} \mathbf{u}^t \mathbf{A} \mathbf{u} - \mathbf{A} \mathbf{u}. \quad (3.49)$$

which is then the case if the gradient of f

$$-\text{grad } f = \mathbf{r} = \mathbf{b} - \mathbf{A} \mathbf{u} \quad (3.50)$$

approaches zero. Starting with an initial point in the solution space, in every iteration k , a vector \mathbf{p}^k is determined that determines the direction in which the solution should be approached. Basically, two successive directions are conjugate with respect to \mathbf{A}

$$\mathbf{p}_k^t \mathbf{A} \mathbf{p}_{k+1} = 0 \quad (3.51)$$

and hence the name of the method. The approximation accuracy of the conjugate gradient method is controlled by a user-specified tolerance value. In order to improve the convergence properties of the solver, the system matrix is preconditioned.

The Abaqus FE code is parallelised using the domain decomposition technique and can therefore be executed on large computer clusters. The numerical effort for simulating 2-D and 3-D poroelastic processes is discussed in the chapter 5 concerning applications of the numerical FE model.

3.3 Discussion

The finite-difference method is the oldest method for determining approximate solutions of partial differential equations and in many engineering applications

it has already been replaced by more modern concepts such as e. g. the finite-element method. FD methods are nevertheless still popular and widely used in many branches of engineering and applied physics, in particular for solving hyperbolic problems such as wave propagation. One reason for this is that the limiting factor for code accuracy is inherently the propagating wavelength that has to be resolved properly throughout the whole domain through which the propagation occurs. Therefore, the advantage of unstructured meshes is less than e. g. for static stress calculation, where localisation effects may play an important role. A similar argument applies for the case of random media where medium heterogeneities are distributed throughout the model domain. In this case, the creation of an irregular grid is also a difficult task. If a FE scheme is written for a regular grid, it becomes similar to the schemes derived by the FD method.

The FE method, however has several advantages for modelling quasistatic consolidation. In particular, if a well-defined internal interface is modelled, the irregular grid allows to accurately resolve the strong spatial gradients in its vicinity. The automatic determination of the time step size is another advantage for consolidation experiments, since the strongest temporal changes are usually encountered in the beginning of a simulation, while for later times, the diffusion process becomes very slow. If the time step is determined accordingly before each time update, the discrete FE solution is optimally adapted to the physical problem under consideration.

A difference between the formulations of the FD and FE method is in the stability properties of the two schemes. While the implicit time stepping, as used by the FE solver, provides unconditionally stable solutions, the explicit FD time stepping requires that the maximum time step size is chosen sufficiently small, as explained in section 3.1.4. It is however important to note that all derived stability criteria are only applicable for homogeneous media, and in the heterogeneous case, general stability conditions are not available.

In the section on spatial FD operators, two approaches were presented: standard and rotated staggered grids. As was pointed out, the rotated approach entails lower memory requirements for storing material parameters, or update coefficients, respectively. On the other hand, an additional mapping operation is required per computed derivative. Sometimes, the rotated grid approach is found to improve the stability of the algorithm when high material contrasts are present within the medium. In contrast to the work of Saenger et al. (2000) on elastic wave propagation, in the context of this work no evidence was found that rotated operators if compared to standard operators provide more stable results under strongly heterogeneous conditions. Actually, both staggered approaches provide stable results, even if the contrasts are extremely large. This will be demonstrated in the following chapters by different numerical examples.

Chapter 4

Accuracy and scalability tests

The numerical methods presented in the preceding chapter provide approximate solutions of a given poroelastic problem. Before applying numerical methods for practical problems, it is useful to carefully investigate the conditions under which accurate solutions are obtained. As far as the simulation of wave propagation is concerned, the resolution of the wavelength plays a key role in the context of accuracy. If the wave length is not well sampled, numerical dispersion effects deteriorate the solution which is similar to aliasing effects in signal processing. The Biot slow P -wave is an additional wavemode in poroelastic media with a large impact on simulation accuracy. Depending on the frequency regime, this wave mode is either inertially dominated or diffusive. In the latter case, the diffusion lengthscale needs to be resolved by the numerical simulation in addition to the propagating fast P - and S -waves.

In this chapter, a series of finite-difference experiments is presented that allows the accuracy of the numerical scheme presented in section 3.1 to be investigated under various conditions. For this purpose, the simulation results are compared to exact analytical solutions. A performance test carried out on a parallel Linux cluster demonstrates the scalability of the FD scheme.

4.1 Numerical dispersion

In this first numerical example, I simulate wave propagation within a homogeneous porous medium and compare it to an analytical solution given by Norris (1985). Such a solution is available in the time domain if friction between fluid and matrix is neglected, i. e. if the viscosity η is set to zero or permeability κ to infinity, respectively. This corresponds to the high-frequency limit of Biot's equations. As a source, a Ricker wavelet with centre frequency 25 kHz is used. At 100 mm offset, two incoming waves are recorded: first, a fast P -wave arrives and then a slow P -wave. The two seismograms in Figure 4.1a are calculated

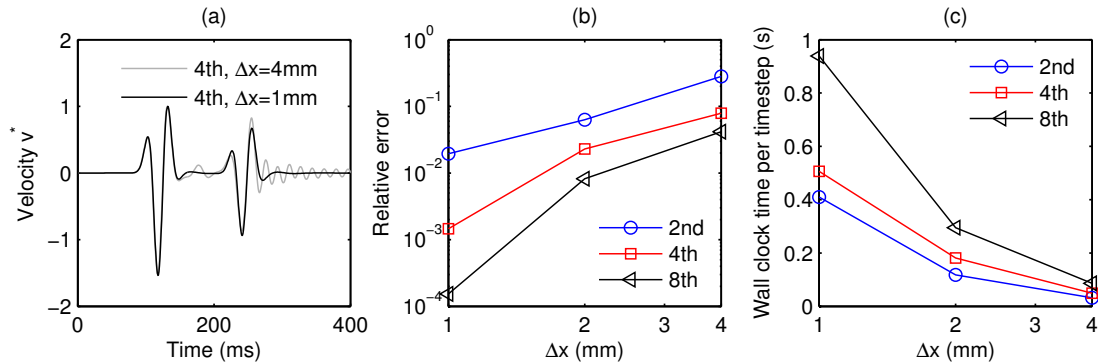


Figure 4.1: Numerical dispersion in a 2-D frictionless, homogeneous, porous medium. (a) Synthetic seismograms, calculated with 4th order operators and different spatial resolution. (b) Deviation from the exact analytical solution given by Norris (1985) for varying spatial resolution and spatial FD operators. (c) Associated wall clock time required per timestep.

using 4th order FD operators, a time step $\Delta_t = 0.2\mu\text{s}$ and two different spatial samplings. The seismogram with the coarser resolution $\Delta_x = 4\text{mm}$ shows typical oscillations that indicate strong numerical dispersion. In order to quantify the dispersion errors, I compute the sum of rms deviation of the computed seismograms from Norris' exact solution. For varying spatial resolution and different spatial operators, the dispersion errors are given in Figure 4.1b. The error is reduced by both decreasing the spatial sampling Δ_x and increasing the order of the spatial operator, thus approaching the theoretical solution. As can be seen in Figure 4.1c, the price for accuracy is of course an increased computational cost.

A comparison of velocity and pore pressure seismograms for the same numerical setup is shown in Figure 4.2. Here, the seismograms of relative velocity q reveal that the fast mode is associated with very little relative motion between the fluid and the solid phase, unlike the slow wave mode. This makes the relative particle velocity field particularly useful to emphasise slow P -wave modes. Provided that the spatial discretisation is sufficiently fine, the FD approximation is accurate and numerical and thus analytical results are in excellent agreement.

4.2 Inertial and diffusive regimes

One of the fundamental results of Biot's theory is the existence of a slow compressional wave mode in addition to the compressional and shear wave modes in elastic solids. At very high frequencies this slow P_s -wave has the character of a propagating wave mode, while at low frequencies, it shows diffusive behaviour.

The example given in Figure 4.3 shows that numerical implementations of

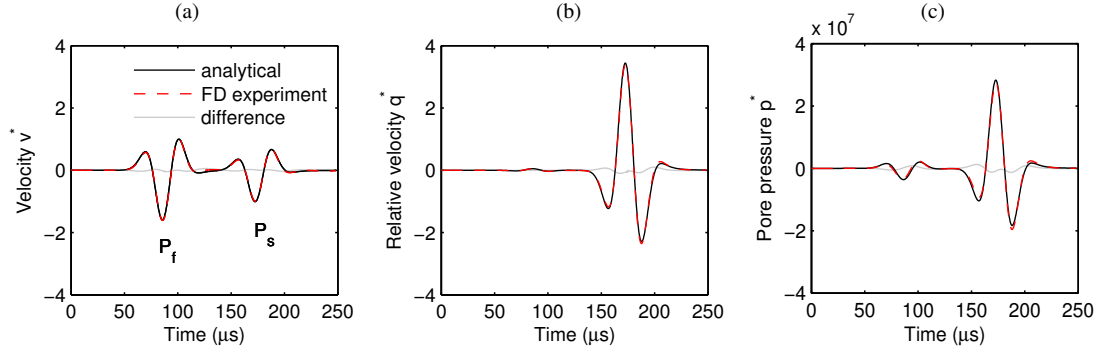


Figure 4.2: Synthetic velocity and pore pressure seismograms simulated within a 2-D frictionless, porous medium using 4th order operators and 1mm grid spacing. Synthetic seismograms of total velocity (a), relative velocity (b) and pore pressure (c) are compared to the exact solution given by Norris (1985).

Biot's equations describe not only propagating waves, but also completely contain the low-frequency diffusive behaviour of the slow P -wave. For that purpose, a fluid injection source (in units of Pa) of the form

$$p(t) = \begin{cases} 0 & \text{if } t < 0 \\ \int_0^t \sin^3(\pi\tau/t_s) d\tau & \text{if } 0 < t < t_s \\ 1 & \text{if } t > t_s \end{cases}, \quad (4.1)$$

is used to excite a slow P -wave within a homogeneous wet sandstone model. By varying the medium permeability κ and therefore ω_B , the spatiotemporal response is either more of an inertial type with a propagating wave front or of a diffusive type. In the inertial regime, the wave front moves with a constant velocity. This high-frequency velocity is obtained easily from the dispersion relation 2.54

At low-frequencies, the slow P -wave does not propagate any more. Instead, in the diffusive regime, the pore pressure is governed by the homogeneous diffusion equation and the solution to a step load is given in form of the complementary error function, see equation 2.77.

The results as shown in Figure 4.3 indicate that both limits are modelled accurately by the numerical implementation of the dynamic Biot equations. At a very small time scales with $t = 0.2\omega_B^{-1}$, one observes a propagating front whose position in agreement with the expected velocity as calculated from equation 2.54. At large time scale with $t = 20\omega_B^{-1}$, the diffusion limit provided by equation 2.77 is met. At intermediate timescales that are in the order of the critical relaxation time, i. e. at $t = 2\omega_B^{-1}$, the diffusion solution is also valid but the signal propagation is bounded by the velocity for the slow wave.

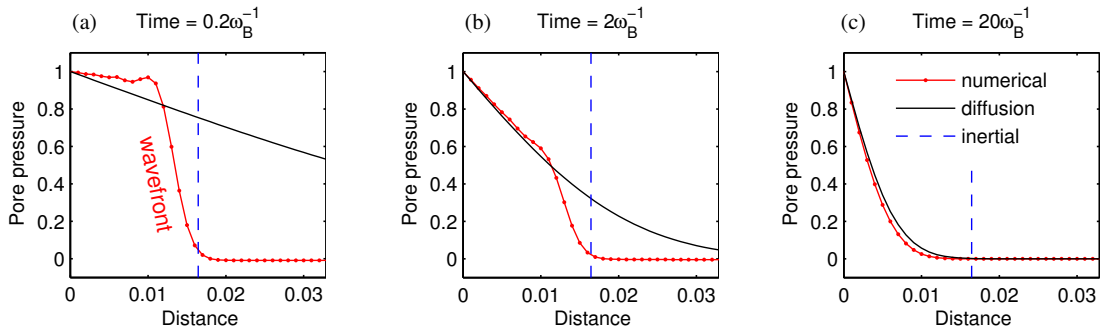


Figure 4.3: Pore pressure profiles for a “step” loading at $x = 0$. The numerical solution of the fully dynamical Biot equations is compared to the limiting cases of pure inertial wavefront and the solution of the diffusion equation. The response a pure wave front for short times (a), a diffusive response for long times (c) or a combination of both at intermediate times (b).

4.3 Resolution of the diffusion boundary layer

In the preceding example, a slow P -wave is excited by a Dirichlet pore pressure source. Now it is demonstrated that at poroelastic interfaces, fast P -waves may excite fast *and* slow P -waves and the reflection coefficient is governed by the behaviour of the slow P -wave. From the frequency-dependence of the slow P -wave it follows that the reflection response also depends on the frequency of the incident wave.

Consider an interface between a gas-saturated and a fully water-saturated unconsolidated sandstone with material properties given in Tables 2.1 and 2.2. A Ricker wavelet is chosen as an input signal. The model domain consisting of two halfspaces is four times as large as one P -wavelength. In order to reveal the frequency-dependence of the reflection response, a set of simulations with varying permeability κ is conducted, exploiting the fact that the normalised frequency ω/ω_B is the governing non-dimensional parameter in the system. This implies that changing the permeability of the porous matrix κ (and therefore the Biot frequency ω_B) is mathematically equivalent to changing the source frequency and the spatial scale of the simulation. The frequency regimes modelled this way range from seismic where friction is dominant to ultrasonic where the inertial terms prevail. The spatial sampling is varied between 30 and 240 gridpoints per fast P -wavelength and 4th order spatial operators are used. As in the previous example, the time step is $\Delta_t = 0.2\mu\text{s}$. The results are compared to the exact analytical solution given by Dutta and Odé (1983), see Figure 4.4.

The reflection coefficient is obtained from the synthetic pore pressure seismograms by dividing the maximum amplitude of the reflected fast P -wave by the

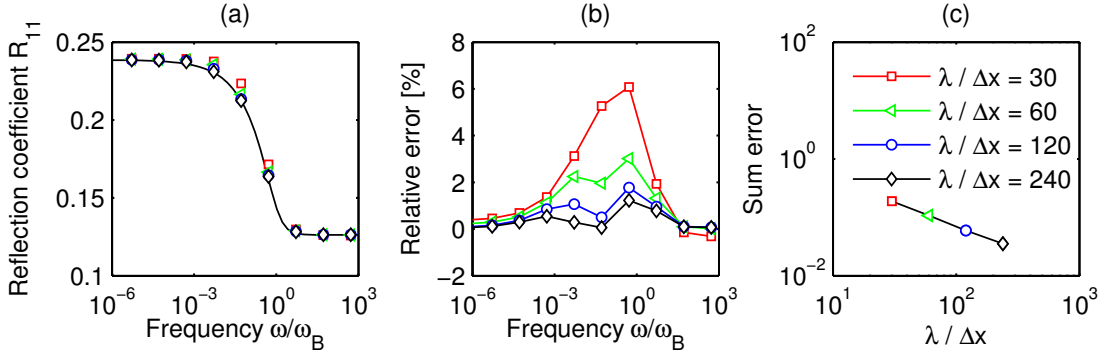


Figure 4.4: Frequency-dependent reflection from a gas-water contact in unconsolidated sandstone. (a) The numerical coefficients, obtained for four different spatial samplings, are computed as the fraction of maximum pore pressure of the reflected wave p_r and the incident wave p_i . The solution is compared to an exact analytical solution (solid line) given by Dutta and Odé (1983). (b) Estimates of the relative error as a function of frequency and spatial resolution. (c) Integral error obtained by summing up the deviation of the numerically obtained values from the exact solution.

maximum amplitude of the incident fast P -wave

$$R_{11}^{\text{num.}}(\omega/\omega_B) = \frac{p_r}{p_i}. \quad (4.2)$$

In Figure 4.4a, two frequency regimes are identified. In the low-frequency limit, i. e. for very low permeabilities, the diffusion length is very small compared to the wavelength and therefore practically no fluid flows during one wave cycle. For very high permeabilities with $b \rightarrow 0$, i. e. in the high-frequency limit, fast and slow P -waves are reflected and transmitted from the gas-water contact, since inertial terms dominate the friction effects. The crossover between these two regimes occurs at frequencies around and below the critical Biot frequency.

Qualitatively, the simulations with different spatial samplings provide similar results. In particular, the high- and low-frequency limits are met. There are, however, deviations from the exact solution at intermediate frequencies, especially for the lower resolution. This is emphasised in Figure 4.4b showing the relative deviation of the numerically obtained estimates of R_{11} from the exact solution. Maximum relative errors are obtained at approximately the Biot frequency and their magnitude decreases with increasing spatial resolution. An integral measure of the overall error is shown in Figure 4.4c.

Figure 4.4b shows comparatively strong deviations at frequencies around and below the characteristic Biot frequency ω_B , while the error is smaller for $\omega/\omega_B < 10^{-3}$ and $\omega/\omega_B > 10$. This is due to the fact that at frequencies considerably exceeding ω_B , the diffusion lengthscale of the slow P -wave is large and therefore, a

coarse grid is basically sufficient to resolve the process. The lower the frequency is, the smaller is the diffusion length and errors occur due to improper resolution of the diffusion process at the interface. The numerical solution is biased towards the low-frequency limit or in other words, low spatial resolution enhances apparent friction and hampers the diffusion process. In the low-frequency limit, the effects of the diffusive slow P -wave become insignificant and therefore, a good estimate of the reflection response is obtained even if the diffusion scale is not resolved.

Although no seismograms of the reflection experiment are shown, it should be noted that the amplitude errors cannot be observed in the shape of the fast P -waveform. The fact that a very fine spatial sampling of the propagating P -wave is required to yield an adequate reflection response is a manifestation of the problem of numerical stiffness addressed in the preceding chapter.

4.4 Modelling free fluids

A special question arising in poroelastic modelling is the correct representation of free fluids within the framework of poroelasticity. This problem appears when high-porous inclusions such as cracks and fractures are embedded within a porous rock matrix. They are mechanically very soft and on the other hand characterised by a very high permeability. Indeed, in reservoirs fractures usually govern the fluid mobility while most of the pore space volume is often associated with the porous host rock.

As was shown section 2.6, the Biot wave equations are consistent with the equations of elastic wave propagation and this limit is approached by increasing the friction between fluid and solid matrix.

There are two possible approaches to numerically model fluids in contact with a porous medium. The first approach is to explicitly define different domains that are filled by fluid or a porous medium, respectively. In both domains, the poroelastic or acoustic wave equations are solved and they are then linked dynamically at the internal interface. Although this is a common approach for analytical models, its numerical implementation is complex and comes with a lot of administrative cost for exchanging mass and momentum internally between different domains.

Therefore, it would be useful to model fluids directly within the framework of poroelastic rheology by choosing the material parameters appropriately. An obvious choice for the porosity is letting $\phi \rightarrow 1$ and at the same time tortuosity $\nu \rightarrow 1$. This implies $\rho^b, \rho^m \rightarrow \rho^f$ as well as $\alpha \rightarrow 1$ and $H, M \rightarrow K_f$ (Bourbié et al., 1987). Furthermore, letting $K_d, G \rightarrow 0$, the poroelastic wave equation 2.25 becomes

$$\rho^f \ddot{u}_i + \rho^f \ddot{w}_i = K^f u_{j,ji} + K^f w_{j,ji} \quad (4.3)$$

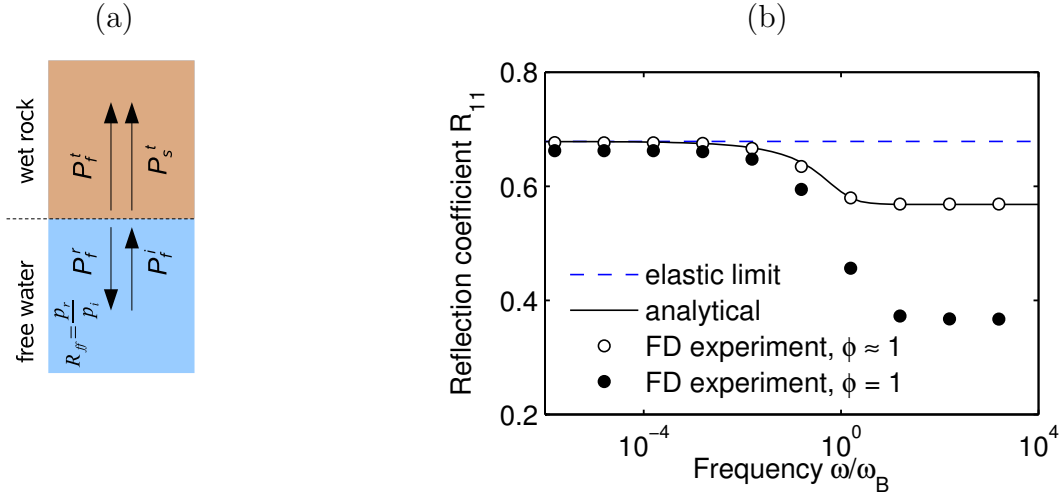


Figure 4.5: Frequency-dependent reflection from an interface between a free fluid (water) and a porous rock (saturated sandstone), as shown in (a). The reflection response is very different if the fluid is modelled with 100% porosity or porosity 99.9% (b). The latter is identical with an analytical solution (Quiroga-Goode and Carcione, 1997).

which simplifies using $w_i = u_i^f - u_i$ to

$$\rho^f \ddot{u}_i^f = K^f u_{j,ji}^f. \quad (4.4)$$

This is indeed the acoustic wave equation, describing compressional waves in fluids. Although this reduction to the acoustic case is done easily, the modelling of fluids by using poroelastic equations requires particular care. E. g., one observation of the behaviour of the numerical FD code is shown in Figure 4.5. The model contains an interface between fluid (water) and a consolidated porous sandstone, fully saturated with water, as well. For this case, an analytical solution is given by Dutta and Odé (1983) or alternatively Quiroga-Goode and Carcione (1997). Numerical results show a strong deviation from the theoretical values if the fluid is modelled using $\phi = 1$. If porosity is only slightly smaller than 1, the numerical results are in agreement with the theoretical values. In this case, the elastic moduli should be

$$K_s = \epsilon, \quad (4.5)$$

i. e. a small value larger than one,

$$K_d = (1 - \phi)K_s, \quad (4.6)$$

$$G = 0, \quad (4.7)$$

thus ensuring the conditions for the Biot coefficient $\alpha = 1$ and the pore space modulus $M = K_f$. If the model parameters are chosen such, fluids and interfaces

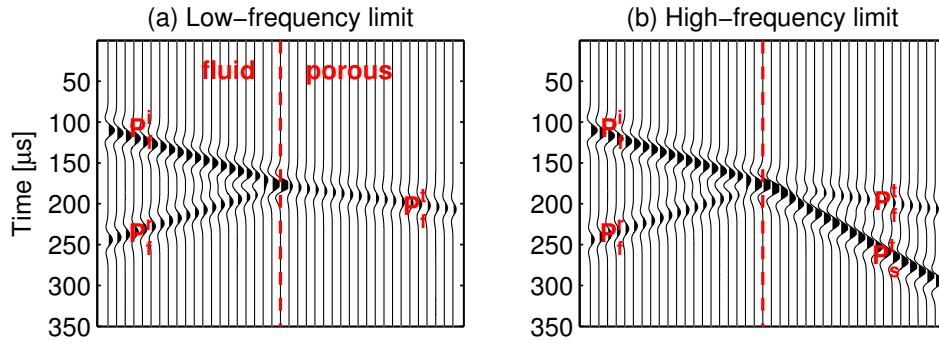


Figure 4.6: Seismograms of normal incidence plane wave scattering from an interface between a free fluid and a porous water saturated sandstone. In the low-frequency limit (a), the porous rock behaves like an equivalent elastic medium, such that one fast P -wave is transmitted. At high frequencies (b), however, fast and slow P -waves appear and the amplitude of the reflected wave mode is lower.

are consistently represented within the framework of poroelastic modelling tools. Figure 4.6 illustrates the behaviour of an acoustic wave reflected and transmitted at a fluid-porous interface. In the low-frequency regime, the slow P -wave does not propagate and only one wave is transmitted, one reflected. At high frequencies, the slow P -wave propagates and an additional wave mode is involved in the mass and momentum balance across the interface.

Finally, stability is also an important issue when modelling cracks and free fluids. Critical in this context is the stability condition 3.39

$$\frac{\nu}{\phi} > \frac{\rho^f}{\rho^b}, \quad (4.8)$$

stating that the tortuosity ν is cannot be approach 1 simultaneously with porosity ϕ . This would violate the stability condition. Therefore, a value slightly larger than one is required for the tortuosity to yield stable results.

4.5 Parallel performance

The scalability of the poroelastic FD scheme is estimated by two performance tests performed on the XC6000 Linux cluster of the Scientific Supercomputing Center of Karlsruhe University. Simulations are carried out on 4, 8, 16, 32 and 64 Intel Itanium2 processors, where each processor is located on a two-way node with 12 GB of main memory. The communication network is a Quadrics QsNet II Interconnect. The performance tests differ insofar that first, total number of

np	wall clock time / time step (ms)	
	ngp = 10 ⁶	ngp = 10 ⁶ × np
4	53	212 ¹
8	27	215
16	15	217
32	08	221
64	05	232

Table 4.1: Elapsed wall clock time for two sets of test simulations: one with constant total domain size, the other one with constant domain size per process.

¹ Reference value wct_{ref}

grid points is kept constant while increasing the number of processes involved, and in the second test, the number of gridpoints per process is kept constant.

First, the model with a total size of 1000×1000 grid points (ngp) was considered. Increasing the number of processes (np) results in a reciprocal decay of elapsed wall clock time (wct) per time step. The speedup is then the inverse relative decay in computation time

$$\text{speedup}_1 = wct_{\text{ref}}/wct_i. \quad (4.9)$$

In the second test set, the domain size was increased with increasing number of processes up to a maximum domain size of 8000×8000 grid points. Obviously, the elapsed time per timestep is approximately constant with a slight increase due to communication between the processes. For this set, the fraction

$$\text{efficiency}_2 = \text{speedup}_1 = wct_{\text{ref}}/wct_i \quad (4.10)$$

is the efficiency of the simulation. For comparison, a speedup curve is also computed according to

$$\text{speedup}_2 = wct_{\text{ref}}/wct_i \times \text{np}. \quad (4.11)$$

The results of the scaling investigation are listed in Table 4.1 and furthermore given in Figure 4.7. A continuous decay in efficiency with rising number of processes is observed for both sets of simulations. However, if the domain size per process is kept constant, an efficiency of 91% is obtained for 64 processes.

4.6 Discussion

The quantification of numerical discretisation errors for poroelastic FD modelling has been the main focus of this chapter. In seismic modelling of purely elastic waves, numerical dispersion criteria are well-known, stating that the smallest wavelength has to be resolved properly. The better the criterion is fulfilled, the

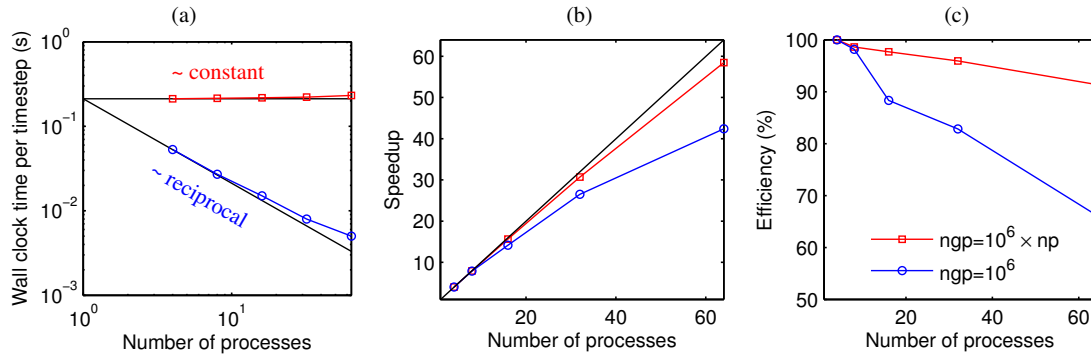


Figure 4.7: Scalability test of the poroelastic FD scheme. Two sets of test simulations are considered with values given in Table 4.1.

better is the conservation of waveforms and the reproduction of phase velocities. Within the seismic frequency range in poroelasticity, the smallest relevant scale is the diffusion length λ_D that is usually orders of magnitudes smaller than the largest wavelength λ_{P_f} of the fastest wavemode. This is a well-known problem of poroelastic modelling (Carcione and Quiroga-Goode, 1995), however it is often disregarded in the literature. If the grid is too coarse to sample the slow and hence small-scale diffusion process, the grid acts like a spatial filter and the solution deteriorates. It was found that the effect of such a “grid filter” is that instead of the true poroelastic response, one obtains numerically the response of the equivalent elastic medium. In order to give physically consistent results, the grid increment often has to be orders of magnitude smaller than what is needed for elastic or viscoelastic modelling. The stiffness of the problem rises with decreasing frequency as $1/\sqrt{\omega}$.

One answer to the problem of numerical stiffness and the resolution of the diffusion length is the application of parallel schemes that allow for the calculation of larger models, i. e. models with a finer discretisation and therefore a greater number of grid points and timesteps. The scalability test presented in this chapter proved the high efficiency of the poroelastic FD scheme even on larger computer clusters. However, on currently available supercomputers, the simulation of surface seismic surveys with frequencies around 50 Hz, wavelengths of 60–100m, diffusion lengths around 1 cm and domain sizes in the order of several kilometres would require tens of thousands of gridpoints per spatial dimension which is still beyond feasibility. The application of the FD method as a simulation tool is therefore restricted to the scales of borehole acoustics and laboratory experiments.

Chapter 5

Applications

There are two principal aims of applying numerical tools in the context of this work, that shall be subsequently called *experiment* and *simulation*. The goal of numerical experiments is the systematic determination of fundamental relationships between the material properties of the medium and the seismic response. Characteristic for this type of modelling philosophy is a certain degree of abstraction, simplification and reduction of the influential parameters to a minimum. The advantage of results from numerical experiments if compared to analytical estimates is that no assumptions have to be made beyond those inherent in the poroelastic description. Experiments provide means of verifying theoretical estimates and for evaluating the range of their applicability.

In contrast to experiments, numerical simulation aims at reproducing laboratory data and predicting the behaviour of particular rock types. Instead of considering a simplified synthetic representation of a real rock sample, the numerical setup is chosen such that the complexity of the sample geometry is reflected as much as it is possible. In combination or complementary to laboratory experiments, numerical simulation can provide insights onto the underlying physical mechanisms, thus contributing to the interpretation of measurements. Eventually, this may lead to substituting additional laboratory tests.

The purpose of this chapter is to give several numerical examples to show how poroelastic modelling contributes to solving modern problems in rock physics research. Beginning with finite-difference (FD) wave propagation experiments of wave scattering from porous inclusions, the conversion of different wave modes at internal interfaces is illustrated. Results are shown for the cases of partial saturation and cracked media. If the wavelength of the incident wave is much larger than the size of the inclusion, scattering from fast to slow waves is dominant and the overall behaviour is then described by the quasistatic approximation. This makes it possible to use finite-element (FE) relaxation experiments to estimate effective material properties. The scattering of elastic and poroelastic waves in

Table 5.1: Material properties used in the numerical applications.

	consolidated sandstone	unconsolidated sandstone	crack
K_s (GPa)	35	35	10^{-3}
K_d (GPa)	5	2.5	10^{-5}
μ (GPa)	11	1	0
ϕ	0.2	0.3	0.99
ν	2.0	2.0	1.01
κ (D)	1	1000	∞
ρ^s (t/m ³)	2.65	2.65	2.65
	water	gas	air
K_f (GPa)	2.25	0.10	0.00014
ρ^f (t/m ³)	1.0	0.1	0.001
η (mPas)	1.0	0.22	0.02

random media is the topic of the following sections. Finally, the simulation of an ultrasonic laboratory experiment is presented. An overview of the material parameters used in the numerical examples is given in Table 5.1.

The examples given in this chapter are based on publications of Wenzlau et al. (2007), Wenzlau and Müller (2008), Wenzlau et al. (2008) and for the ultrasonic wave simulation of Lebedev et al. (2009).

5.1 Scattering from porous inclusions

The influence of cracks on effective poroelastic parameters is a current research topic in rock physics. Mechanically, cracks are very thin, soft and highly permeable heterogeneities within a porous rock matrix. Usually, cracks and fractures are considered to be much larger than the average pore size of the surrounding medium (Gurevich et al., 2007). They are characterised by their thickness and shape as well as their distribution in the rock matrix. The presence of cracks and their geometry may cause characteristic frequency-dependent dispersion and attenuation of seismic waves (Brajanovski et al., 2006; Berryman, 2007). This is particularly important when during one wave cycle, there is an exchange of fluid between crack and matrix.

As an example, consider a 2-D model with a size of 400×400mm, surrounded by an absorbing layer of 100mm. The grid increment Δ_x is 1mm. A plane

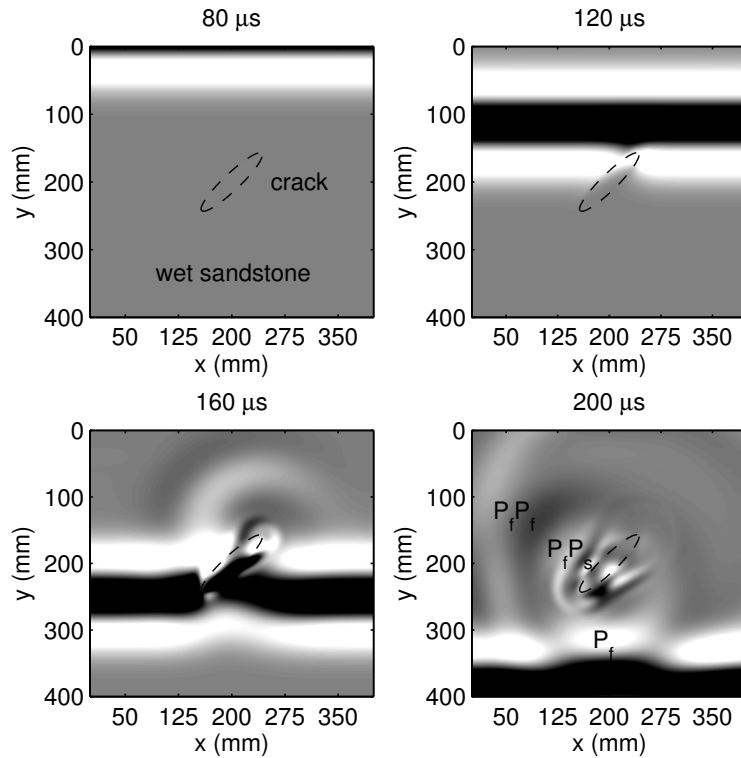


Figure 5.1: Scattering of a plane compressional wave from an elliptic crack. Snapshots of pore pressure fields at four different times.

fast P -wave with 25kHz centre frequency is used that encounters an elliptically-shaped crack, embedded within a water-saturated consolidated sandstone model (see Table 5.1).

The crack is modelled as a free fluid (see section 4.4) by setting the porosity to 99% and the matrix moduli to a very small value, according to relations 4.5–4.7. In order to fulfil condition 3.37, a time step Δ_t of $0.1\mu\text{s}$ is used.

Figure 5.1 shows pore pressure snapshots of a plane wave interacting with the elliptical inclusion. A slow P -wave is generated at the crack-matrix interface, slow modes are distinguished from the fast modes by their smaller wavelength. Induced fluid motions can also be emphasized by comparing the scattered pore pressure field with the corresponding elastic case, i. e. when permeability κ is considered to be zero (results not shown). Due to the wavemode conversion at the applied frequency of 25kHz, the wavefield around the crack shows a complex pattern.

A second example of plane wave scattering is now considered that is motivated by the typical observation that reservoir rocks show patchy saturation in the presence of two or more fluid phases, often liquid and gaseous. The term patchy refers to the situation when the fluid phases are not homogeneously dis-

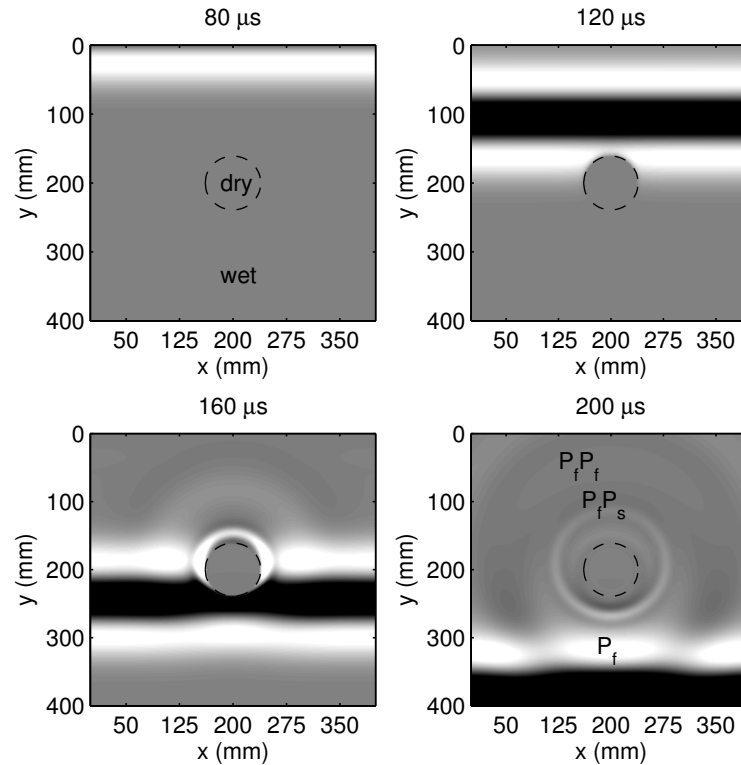


Figure 5.2: Same as figure 5.1, but for a circular gas inclusion.

tributed, but rather form isolated pockets of a characteristic size. Partial saturation is particularly relevant for waves in reservoirs, since it may significantly affect seismic velocities and attenuation (White et al., 1975).

2-D snapshots show plane wave propagation within a medium with an air saturated inclusion, embedded in water-saturated consolidated sandstone. The experiments are similar to those of Carcione et al. (2003). All material properties are given in Table 5.1. The general numerical setups are the same as in the previous example of a cracked medium. The model has a circular dry inclusion with a diameter of 7.5cm. Again, a plane fast P -wave is used to excite the medium. The wavelet is of Ricker type with 25kHz centre frequency.

For the partial saturation scattering experiment, pore pressure fields are given in Figure 5.2. The incident fast P -wave is almost perfectly transmitted through the inclusion. No pore pressure is built up within the dry inclusion during the passage of the incident wave. This has to be expected due to the low bulk modulus of the gaseous phase. Consequently, a pore pressure gradient appears that drives fluid flow across the interface and a slow P -wave arises at the interface between dry inclusion and wet surrounding. The slow waves are strongly dissipated, as is seen in the snapshots for larger propagation times.

5.2 Quasistatic relaxation experiments

Conventionally, dispersion and attenuation are estimated from numerical wave propagation experiments by using the spectral ratio or frequency shift method (e. g. Rubino et al., 2007, and references therein). In these experiments, wave signals are recorded along the propagation path, then dispersion and attenuation are calculated by measuring traveltime and the log-amplitude decay. A different approach was suggested by Masson and Pride (2007) where they simulate quasistatic experiments based on a finite differences solver for the dynamic Biot equations. Using their approach, the model size is considerably reduced to only one representative elementary volume (REV).

In this example, the idea of Masson and Pride (2007) is further developed and a new and simple strategy is proposed for estimating effective elastic moduli from quasistatic relaxation experiments. From the moduli, velocity dispersion and attenuation can be derived in a straightforward manner. The simulations are carried out using the commercial Abaqus finite-element solver, a package that allows to calculate consolidation processes based on the Biot theory. A synthetic rock model consisting of two porous layers serves as a benchmark test for the approach.

For the sake of clarity, first the one-dimensional case is considered, and then the idea is extended to the 3-D case. Consider a heterogeneous, fluid saturated, porous rock sample with the height L that is confined laterally, sealed hydraulically and represents an REV of a porous rock. Initially, a vertical uniaxial strain $\langle \varepsilon_{zz} \rangle$ is imposed instantaneously on the sample, resulting into an initial stress state $\langle \tau_{zz}^0 \rangle = \langle \tau_{zz}(t=0) \rangle$ within. The following pore pressure diffusion process governs the relaxation of the whole sample.

The simulations are carried out in the time domain. From the time signals, the limiting cases of relaxed and unrelaxed moduli are directly calculated from the time signals as

$$H_u = \frac{\langle \tau_{zz}(t) \rangle}{\langle \varepsilon_{zz} \rangle} \Big|_{t=0}, \quad (5.1)$$

$$H_r = \frac{\langle \tau_{zz}(t) \rangle}{\langle \varepsilon_{zz} \rangle} \Big|_{t \rightarrow \infty}. \quad (5.2)$$

In order to evaluate the frequency-dependence of the elastic modulus, one calculates the relaxation function ψ commonly used in the context of viscoelastic materials (Aki and Richards, 1980). It is expressed by

$$\psi(t) = \frac{\langle \tau_{zz}(t) \rangle}{\langle \tau_{zz}^0 \rangle} - 1, \quad (5.3)$$

The complex, frequency-dependent, effective P -wave modulus is then

$$\tilde{H}(\omega) = H_u \left[1 + \mathcal{F}\{\dot{\psi}(t)\} \right] \quad (5.4)$$

$$= H_u \left[1 + \int_0^{\infty} \dot{\psi}(t) \exp(i\omega t) dt \right]. \quad (5.5)$$

Here, the dot denotes the time derivative. P -wave velocity and attenuation are obtained from the effective modulus \tilde{H} and bulk density ρ by

$$v = \sqrt{\frac{\text{Re } \tilde{H}}{\rho^b}} \quad \text{and} \quad (5.6)$$

$$Q^{-1} = -\frac{\text{Im } \tilde{H}}{\text{Re } \tilde{H}}. \quad (5.7)$$

An elaborate explanation of this procedure is given in appendix A.

In order to exemplify the applicability and accuracy of the proposed method, results are shown for a porous rock (consolidated sandstone, see Table 5.1) with diffusivity D given by equation 2.75. The synthetic sample is saturated with two fluids, 50% water and 50% gas. A periodically layered fluid distribution with spatial period L is assumed. For this case, an analytical solution is provided by White et al. (1975). Results for the velocity dispersion and attenuation of a P -wave are shown in Figure 5.3. We find that our numerically obtained estimates are in excellent agreement with the predicted values.

As a consequence of Hill's theorem, a partially-saturated rock with isotropic matrix properties is always isotropic, regardless of the distribution of the fluid phases inside the sample. In the case of the previous example, this is easily verifiable by calculating the time-dependent shear modulus as

$$G(t) = \frac{1}{2} \frac{\langle \tau_{zz}(t) \rangle - \langle \tau_{xx}(t) \rangle}{\langle \varepsilon_{zz} \rangle - \langle \varepsilon_{xx} \rangle}, \quad (5.8)$$

where z denotes the vertical direction (loading direction) and x is one horizontal direction. Numerical results indeed show that in the example given in Figure 5.3, the shear modulus is time-independent, implying dispersion-free propagation of shear waves in partially-saturated rocks.

The situation changes if the matrix shear modulus is inhomogeneous, generally resulting in an anisotropic effective behaviour of the heterogeneous medium. In this case, multiple relaxation experiments are necessary to determine all effective elastic moduli. A special case of anisotropy is obtained, if the geometry of the heterogeneity has a symmetry plane in horizontal direction, as e. g. for horizontal layering. In this case, the corresponding effective medium possesses

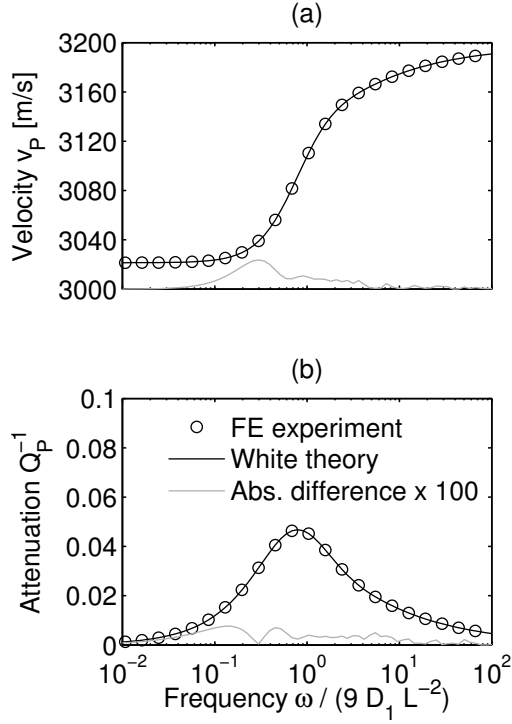


Figure 5.3: Velocity dispersion (a) and attenuation (b) for a partially saturated rock sample. Frequencies are normalised using the diffusivity D and spatial scale L .

vertical transverse isotropy (VTI) and it is described by five independent elastic constants c_{11} , c_{12} , c_{13} , c_{33} and c_{44} , as explained in appendix C.2. In order to determine all five moduli from numerical relaxation experiments, three deformation states are required. They are shown in Figure 5.4. Note that the vertical symmetry axis denotes the 3-direction. The components of the VTI elasticity tensor are then given in long and short notation by

$$c_{11} = c_{1111} = \frac{\langle \tau_{11} \rangle}{\langle \varepsilon_{11} \rangle}, \quad (5.9)$$

$$c_{12} = c_{1122} = \frac{\langle \tau_{22} \rangle}{\langle \varepsilon_{11} \rangle}, \quad (5.10)$$

$$c_{13} = c_{1133} = \frac{\langle \tau_{33} \rangle}{\langle \varepsilon_{11} \rangle}, \quad (5.11)$$

$$c_{33} = c_{3333} = \frac{\langle \tau_{33} \rangle}{\langle \varepsilon_{33} \rangle}, \quad (5.12)$$

$$c_{44} = c_{55} = c_{1313} = \frac{\langle \tau_{13} \rangle}{\langle \varepsilon_{13} \rangle}. \quad (5.13)$$

Additionally, the dependent elastic modulus for shear deformation within the symmetry plane is

$$c_{66} = \frac{c_{11} - c_{12}}{2}. \quad (5.14)$$

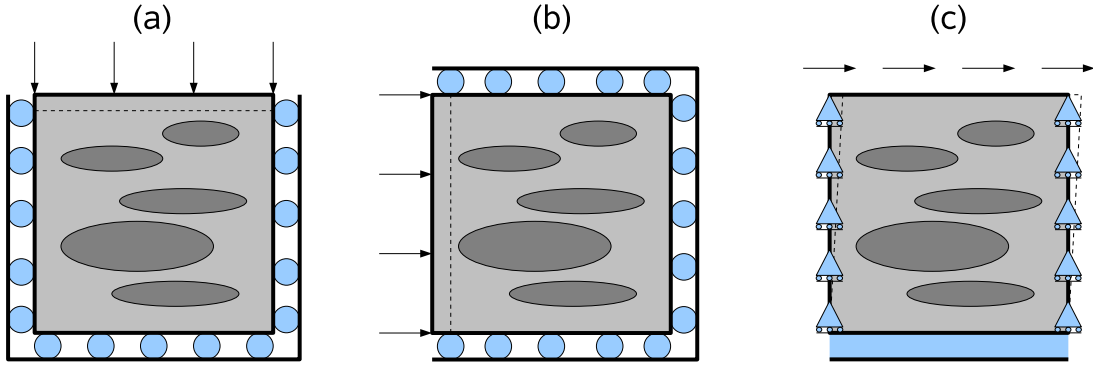


Figure 5.4: Three deformation states used to obtain all 5 effective elastic moduli (assuming effective transversal isotropy). (a) vertical compression or $\langle \varepsilon_{33} \rangle$ -deformation. (b) horizontal compression or $\langle \varepsilon_{11} \rangle$ -deformation. (c) simple shear or $\langle \varepsilon_{13} \rangle$ -deformation.

In the general, anelastic case, the elasticity tensor c_{IJ} derived such is a time-dependent quantity and one should better speak of $c_{IJ}(t)$ as a complete relaxation tensor. It can be transformed to the frequency domain by calculating a relaxation tensor ψ_{IJ} analogous to the unidimensional case.

$$\psi_{IJ}(t) = \frac{c_{(IJ)}(t)}{c_{(IJ)}^u} - 1, \quad (5.15)$$

where the index brackets denote elementwise division (no summation is applied). Transformation to the frequency-domain is done analogous to equations 5.3–5.5, but now carried out subsequently for every component of the relaxation tensor. According to Carcione (2001), velocity and attenuation are calculated from the complex stiffness matrix as

$$v_{IJ} = \sqrt{\frac{\text{Re } \tilde{c}_{IJ}}{\rho^b}}, \quad (5.16)$$

$$Q_{IJ}^{-1} = -\frac{\text{Im } \tilde{c}_{IJ}}{\text{Re } \tilde{c}_{IJ}}. \quad (5.17)$$

Note the formal similarity of equations 5.16 and 5.17 with equations 5.6 and 5.7.

In order to exemplify the anisotropic case, two heterogeneous double-porosity media will now be considered, both with an effectively anisotropic, viscoelastic material behaviour. The first medium is a water-saturated, consolidated sandstone with thin, soft embedded porous unconsolidated layers with higher porosity. Material parameters for these two rock types are given in Table 5.1. A second model is considered with the same materials, but with a soft ellipsoidal inclusion instead of the porous layer. Both models are chosen such that the volume fraction

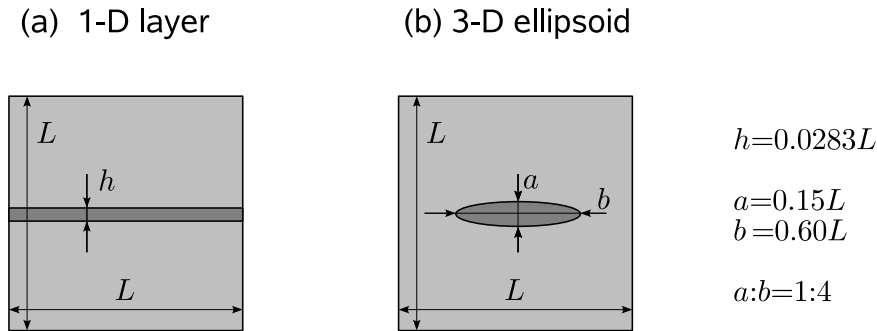


Figure 5.5: Two model geometries for double porosity relaxation experiments. (a) Layered model with layer thickness h , (b) ellipsoidal inclusion with semiminor and semimajor axes a and b , respectively. Total model dimension is $L \times L \times L$.

of the inclusion is 2.83%. The model geometries of the representative elementary volumes are shown in Figure 5.5. Due to the model geometries, both models are effectively vertically transverse isotropic (VTI).

For the layered case, exact theoretical solutions are available for the effective P -wave modulus $\tilde{H}(\omega)$ for normal incidence (Norris, 1993; Brajanovski et al., 2005). In addition to that, the poroelastic Backus averaging gives the high- and low-frequency limits for all three wavemodes (qP , qSV , SH), see section 2.7 and appendix C.2. For the case of the ellipsoidal inclusion, a theoretical solution for the effective P -wave modulus has been reported recently by Galvin and Gurevich (2006). Their model includes fast-to-slow mode conversion but similar to theories for layered models it is restricted to the case of normal incidence. In addition to that, the solution assumes a fluid-filled inclusion and a weak shear modulus of the surrounding rock matrix, such that $G/K^f < a/b$.

The advantage of numerical results if compared to the previously mentioned theoretical solutions is that it is possible to obtain the total complex, frequency-dependent VTI stiffness tensor. Using numerical modelling, dispersion and attenuation of all three wave modes are obtained for arbitrary angle of incidence.

Results for the attenuation of qP - and qSH -waves at normal and grazing incidence are depicted in Figure 5.5. The attenuation is derived using equation 5.17 and the depicted attenuation values correspond to the diagonal entries of the Q_{IJ} matrix, i. e. Q_{11} and Q_{33} for qP -waves, Q_{44} and Q_{66} for SH -waves. The first observation is that maximum attenuation throughout the whole frequency band is encountered for the qP -wave at normal incidence ($\theta = 0^\circ$) for both models, but the values are higher for the layered case by a factor of 2.5 (note the different axes scaling in the two subfigures). Second, the depicted shear wave attenuation is zero for the layered case. This should be expected, since the Backus averaging formulas provide zero dispersion for horizontally polarised shear waves.

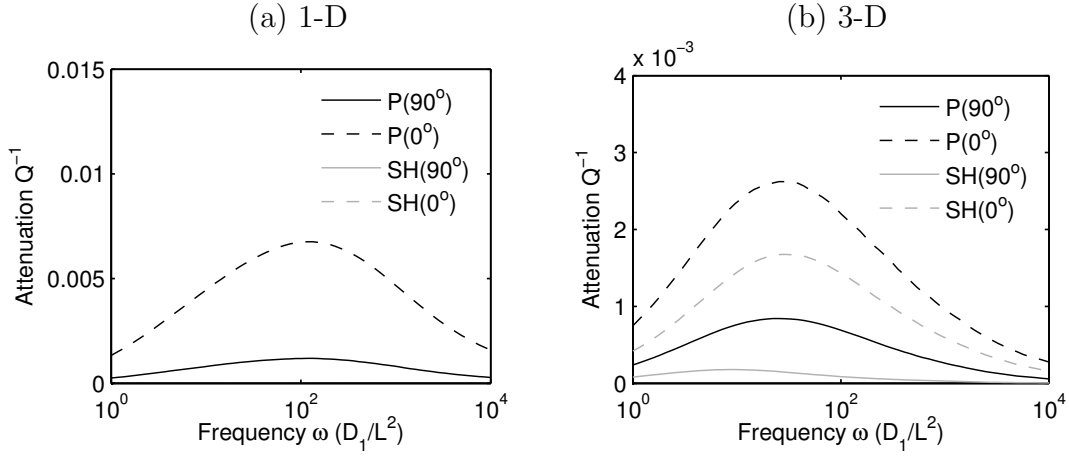


Figure 5.6: Frequency-dependent attenuation Q^{-1} derived from double porosity relaxation experiments, (a) for the layered model, (b) for the model with an ellipsoidal inclusion. P - and SH -waves are considered with normal (0°) and grazing (90°) angle of incidence. In contrast to the layered case, where shear wave attenuation is zero, it is non-zero for the 3-D geometry.

Interestingly, shear wave attenuation is non-zero in the 3-D case of a model with the elliptical inclusion. Actually, the shear wave attenuation of normal incident waves is comparable to that of normal incident qP -waves, attaining a value of $Q_{SH}^{-1} = 0.0018$ if compared to $Q_{qP}^{-1} = 0.0028$. Third, the attenuation curves show a similar frequency-dependence, such that the main difference e. g. between the two curves in Figure 5.5a is the amplitude of the attenuation effect.

This similarity can be further analysed by considering the time-dependence of the relaxation tensor. In the unrelaxed state, the relaxation tensor is zero as can be seen by inserting the undrained limit $c_{IJ}(t = 0) = c_{IJ}^u$ into expression 5.15. On the other hand, in the unrelaxed limit, $c_{IJ}(t \rightarrow \infty) = c_{IJ}^r$ and inserting this in equation 5.15 yield the low-frequency-limit of the relaxation tensor

$$\psi_{IJ}^0 = \frac{c_{IJ}^r}{c_{IJ}^u} - 1. \quad (5.18)$$

Normalisation of the relaxation tensor with its low-frequency limit yields a normalised ψ_{IJ}^n such that one can decompose ψ_{IJ} as

$$\psi_{IJ}(t) = \psi_{(IJ)}^n(t) \psi_{(IJ)}^0 \quad (5.19)$$

with $0 < \psi_{IJ}^n(t) < 1$ and a time-independent tensor ψ_{IJ}^0 that is completely determined by the high- and low-frequency limits of the stiffness tensor \tilde{c}_{IJ} .

Normalised relaxation ψ_{IJ}^n as obtained from the numerical experiments is depicted in Figure 5.7 for the 1-D layered model as well as for the 3-D model with the elliptical inclusion.

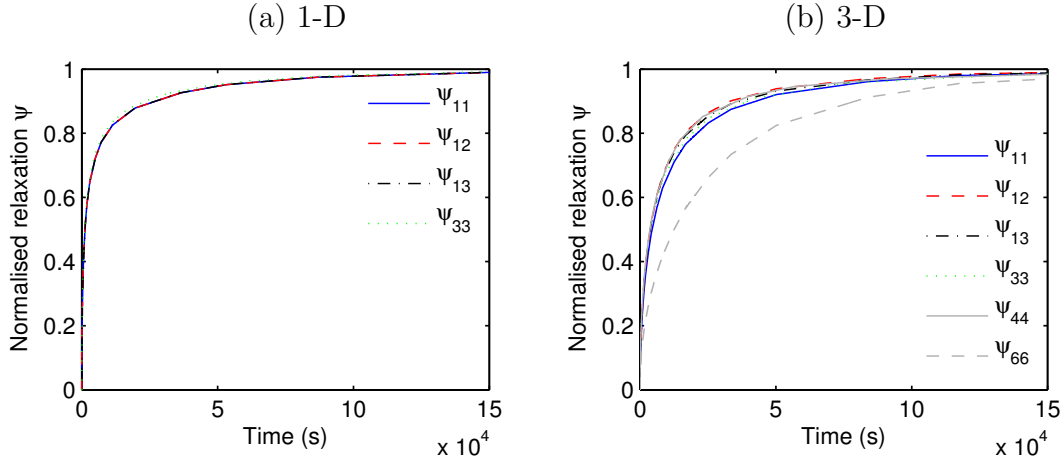


Figure 5.7: Normalised relaxation functions obtained from double porosity experiments. In the 1-D layered case (a) all relaxation functions coincide, while in the 3-D case (b), small deviations are observed.

In the 1-D case, the relaxation due to shear deformation is immediate, or $\psi_{44} = \psi_{66} = 0$, and therefore, only four components are plotted in the corresponding Figure 5.7a. Interestingly, the curves for all four remaining relaxation functions coincide. In other words, the frequency-dependence of all corresponding complex moduli is the same and one has

$$\psi_{IJ}^n(t) = \psi^n(t) \delta_{IJ} \quad (5.20)$$

As a consequence, one can generalise the theoretical results of Norris (1993) and Brajanovski et al. (2006) simply by combining the frequency-dependence obtained for the normal incident P -wave modulus and the frequency limits obtained from Backus averaging (Gelinsky and Shapiro, 1997). Hence first, c_{IJ}^u and c_{IJ}^r are calculated according to equations given in appendix C.2 and combined to equate ψ_{IJ}^0 . Then, the normalised relaxation is calculated by

$$\mathcal{F}\{\dot{\psi}^n\}(\omega) = \frac{\tilde{H}(\omega)/H_u - 1}{H_r/H_u - 1}. \quad (5.21)$$

Finally, the complex stiffness tensor is computed according to

$$\tilde{c}_{IJ}(\omega) = c_{IJ}^u \left(1 + \mathcal{F}\{\dot{\psi}^n\} \psi_{IJ}^0 \right). \quad (5.22)$$

In appendix C.2, this procedure is explained in more detail and it is shown how angle-dependent attenuation can be derived theoretically for the layered model.

The relaxation in the 3-D case differs from the 1-D case insofar as relation 5.20 does not apply exactly. Instead, the normalised relaxation is slightly different

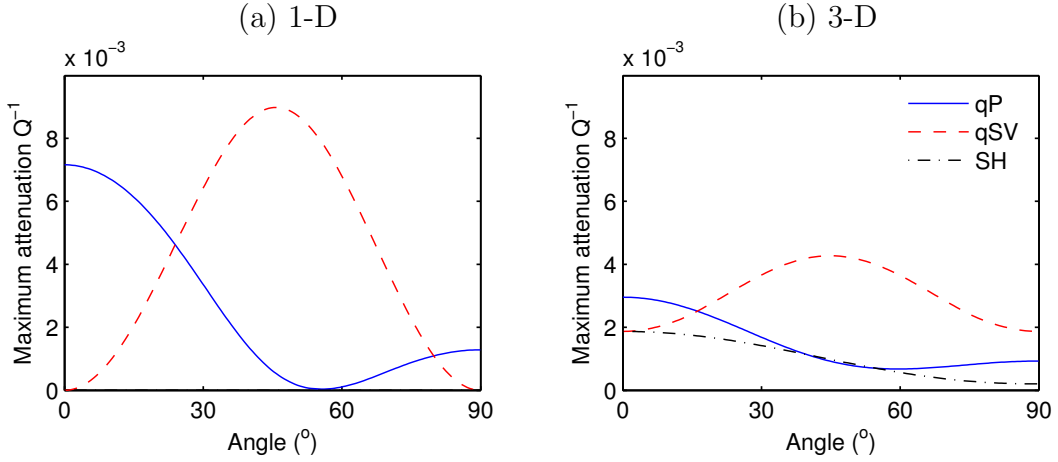


Figure 5.8: Maximum wave attenuation as a function of incidence angle θ for two double porosity relaxation experiments. Results are given for the 1-D layered model (a) and the 3-D model (b). An angle $\theta = 0^\circ$ corresponds to normal incident wave while $\theta = 90^\circ$ corresponds to grazing incidence.

for the different relaxation functions, as seen in Figure 5.7. In particular, the relaxation due to pure horizontal shearing, ψ_{66}^n deviates significantly from the other relaxation functions. The dispersion and attenuation characteristics of the 3-D model must therefore be computed directly from the full stiffness tensor \tilde{c}_{IJ} . This is done by inserting the complex modulus into equations C.23–C.25 given in appendix C.2 yielding three complex velocities \tilde{v}_{qP} , \tilde{v}_{qSV} and \tilde{v}_{SH} as a function of angle of incidence θ . From the complex velocities, dispersion and attenuation are derived as

$$v(\omega, \theta) = [\text{Re}(\tilde{v}^{-1})]^{-1} \quad (5.23)$$

$$Q^{-1}(\omega, \theta) = 2v\text{Im}(\tilde{v}^{-1}) \quad (5.24)$$

Results for the maximum attenuation of compressional and shear waves are given as a function of incidence angle in Figure 5.8. In the 1-D case, only qP - and qSV -waves are attenuated, while the attenuation of the pure shear wave mode is zero, independent of the incidence angle. P -wave attenuation attains zero at approximately 55° and qSV -wave attenuation is zero at $\theta = 0^\circ$ and at $\theta = 90^\circ$.

In the 3-D case, the qP - and qSV behave qualitatively like in the 1-D case. However, there is neither for the qP - nor for the qSV -wave an angle of incidence where no attenuation occurs. In addition to that, a smaller amount of attenuation is also observed for the horizontally polarised SH -wave. For a further discussion and explanation of the results, it is referred to section 5.6.

5.3 Elastic scattering in random media

Earth materials are often described by random fields, where the heterogeneity of the material parameters is characterised by global mean values, variance and correlation properties. If the wave frequencies are much lower than the Biot frequency ω_B and the wavelengths are comparable to the correlation length of the medium, the attenuation and dispersion behaviour is dominated by purely elastic scattering. Therefore, in this limit, it is not necessary to take into account the effects of wave-induced flow and for wave propagation experiments, an elastic formulation is sufficient to describe the scattered wavefield.

As already introduced in section 1.2, in random heterogeneous media, wave field energy is transferred from the vicinity of the first arrival to later arriving signals, i. e. from the primary to the seismic coda. This effect is related to the randomness of wave field attributes and causes scattering attenuation. Using numerical experiments in 2-D elastic, anisotropic, random media, the amplitude fluctuation of plane waves are analysed in order to quantify the attenuation behaviour. The results are then interpreted on the basis of theoretical scattering estimates.

Scattering theory

For a simplified analytical treatment of scattering problems in random media consider the stochastic wave equation

$$\ddot{\mathbf{u}}(\mathbf{x}, t) = \frac{c_0^2}{1 + 2n(\mathbf{x})} \nabla^2 \mathbf{u}(\mathbf{x}, t) \quad (5.25)$$

with a heterogeneous, random field of propagation velocity c that has a mean part c_0 and a fluctuating part n . The mean of n is zero, its variance is σ_{nn}^2 , spatial correlation is described by the correlation function $B(\mathbf{r})$.

The solution of 5.25 is a random wavefield that is characterised by on its part by statistical properties, i. e. mean and variance. For theoretical estimation of wave scattering the relative, logarithmic wavefield amplitude χ is used

$$\chi = \ln \left| \frac{A}{A_0} \right|. \quad (5.26)$$

Scattering coefficients and quality factor can then directly be related to the mean and the variance of χ as (Müller and Shapiro, 2004)

$$\alpha = \frac{\sigma_\chi^2}{L}, \quad (5.27)$$

$$Q^{-1} = \frac{2\alpha}{k} \quad (5.28)$$

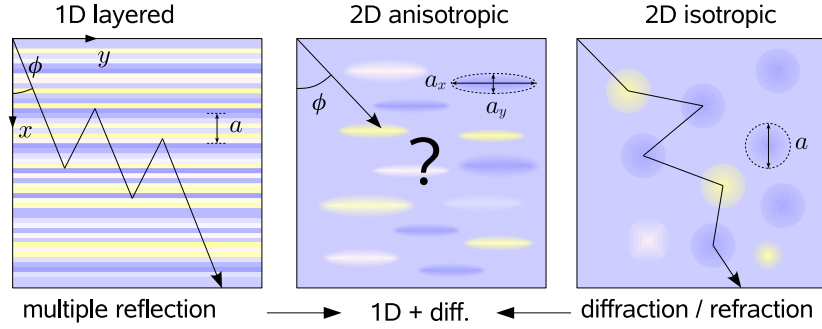


Figure 5.9: Backscattering and random diffraction in layered and in 2-D random media. How do anisotropic heterogeneities behave? How large is the (anisotropic) scattering attenuation?

with the propagation distance L and the wavenumber k . Consequently, knowing the wavefield log-amplitude fluctuations, the scattering attenuation can be inferred directly.

There are various theoretical approaches that describe amplitude fluctuations of seismic waves in random media. Shapiro and Hubral (1999) found that in layered media, propagating waves are subjected exclusively to multiple backscattering and stratigraphic filtering. They propose a model to quantify these effects based on the O'Doherty Anstey formalism. Influential parameters are the characteristic layer period a , the wave number k and the angle of incidence ϕ , shown in Figure 5.9. According to their model, the amplitude variance σ_χ^2 of backscattered waves in 1-D media rises linearly with propagation distance L and can be estimated as

$$\sigma_{\chi,1D}^2 = \sigma_{nn}^2 \frac{\sqrt{\pi}}{2} a_x L k^2 \exp(-k^2 a_x^2 \cos^2 \phi), \quad (5.29)$$

where σ_{nn}^2 is the variance of the medium heterogeneities and a_x is correlation length and ϕ is the angle of incidence.

Wave scattering in media with isotropic correlation function differs significantly from the case of layered media. Instead of dominant backscattering, the wavefield is diffracted and refracted around the medium heterogeneities and the product of wavenumber and correlation length ka mainly governs the dominant scattering direction. For high frequencies or $ka \gg 1$, the wavefield is mainly scattered in forward direction as depicted in the right figure of 5.9. Using the Rytov transformation, the amplitude variance due to diffraction and refraction can be estimated in the case of weak scattering in 2-D media (Müller and Shapiro, 2001, 2004). It rises faster than linear with propagation distance

$$\sigma_{\chi,\text{diff}}^2 = \sigma_n^2 \frac{\sqrt{\pi}}{4} \frac{a_\xi}{a_\eta} k^3 a_\eta^3 D \left(1 - \frac{1}{\sqrt{2D}} \sqrt{\sqrt{1+4D^2}-1} \right) \quad (5.30)$$

with the wave parameter

$$D = \frac{2L}{ka_\eta^2} \quad (5.31)$$

serving as a dimensionless length of the propagation path. Note that the model of Müller and Shapiro considers only the case of isotropic heterogeneities described by one single correlation length a , while in equation 5.30, two correlation lengths a_ξ and a_η are used to describe the effects of anisotropic correlation on the scattered wave field statistics. These effective longitudinal and lateral correlation lengths are given as a function of incidence angle ϕ and the axes of the heterogeneity a_x and a_y

$$a_\xi = a_x a_y (\cos^2 \phi a_x^2 + \sin^2 \phi a_y^2)^{-1/2}, \quad (5.32)$$

$$a_\eta = (\sin^2 \phi a_x^2 + \cos^2 \phi a_y^2)^{1/2}. \quad (5.33)$$

The ratio of correlation lengths $\gamma = a_x/a_y$ provides an estimate of the degree of anisotropy. If the anisotropy is very strong, diffraction for small angles is negligible and backscattering dominates. For weak anisotropy the relationship is vice versa.

Therefore, by combining the theories for backscattering in layered media with diffraction and refraction in 2-D random media, a hybrid model is obtained, see Figure 5.9. If the medium heterogeneities are not isotropic, the scattering depends considerably on the angle of incidence.

Numerical experiments

In order to verify the theoretical estimates of wavefield scattering, numerical experiments of elastic wave propagation in random media are applied. For this purpose, random media realisations are created with a small fluctuation in P -wave velocity $\sigma_{nn}^2 = 5\%$. The background velocities are 3000m/s for the P -waves and 1800m/s for the shear waves. Two examples of the considered random media realisations are given in Figure 5.10. They show a lower homogeneous margin where a plane wave excited that propagates in upward direction. The size of the models is 8194×1100 m with spatial sampling of $\Delta_x = 1$ m.

The wavefields are modelled using a higher-order FD solver (Bohlen, 2002; Cohen, 2002) and in order to fulfil the stability requirement, a time step of $\Delta_t = 2$ ms is applied. Synthetic seismic signals are recorded at 21 geophone lines along the propagation path at every 50m. Each geophone line is equipped with 156 geophones. Examples of recorded synthetic wavefields in the case of $\gamma = 40m : 120m = 1 : 3$ are given in Figure 5.11. From the seismic signals it is clearly

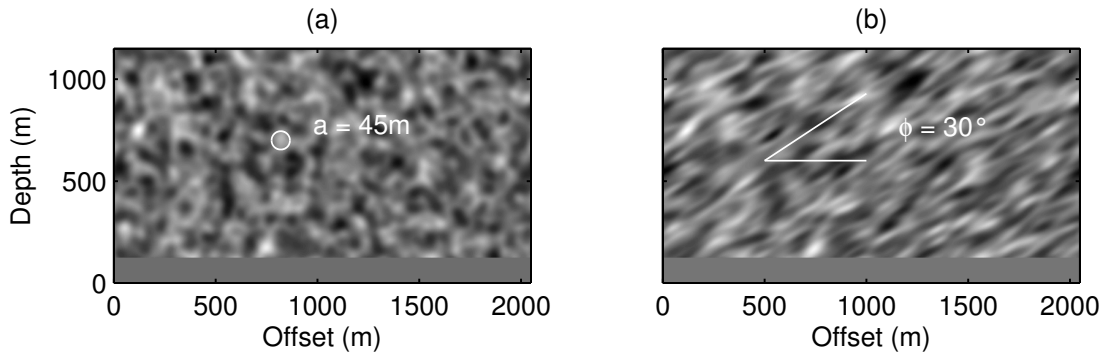


Figure 5.10: Examples of isotropic and anisotropic velocity models used for numerical scattering experiments.

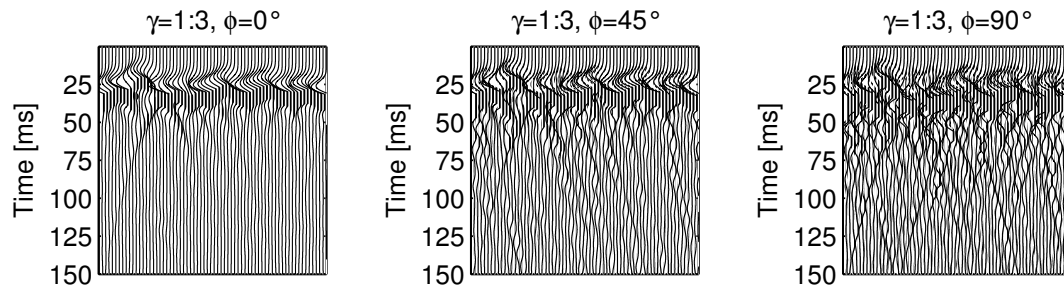


Figure 5.11: Synthetic seismograms of plane compressional waves after passing a heterogeneous effectively anisotropic medium. With increasing angle of incidence ϕ diffraction is becoming dominant.

observed that at normal incidence ($\phi = 0^\circ$, the wave vector is perpendicular to the long correlation axis), small diffraction occurs. However, the effect is considerably stronger in the case of larger angles of incidence where different diffraction hyperbolas are visible.

The quantitative analysis of the random wavefields contains three steps:

1. The signals are tapered in order to separate the amplitude information of the seismic primary from that of the seismic coda.
2. Remnant seismograms are transformed into the frequency domain in order to evaluate the amplitude fluctuation along each geophone line, i. e. for different propagation distances. Figure 5.12 shows an example of calculated amplitude spectra from a scattering experiment in isotropic media. In the first plot, corresponding to a propagation distance $L = 0\text{m}$, the plane wave is coherent and the amplitude spectrum appears as one line. With increasing L , the coherence is lost and the variance of the amplitude

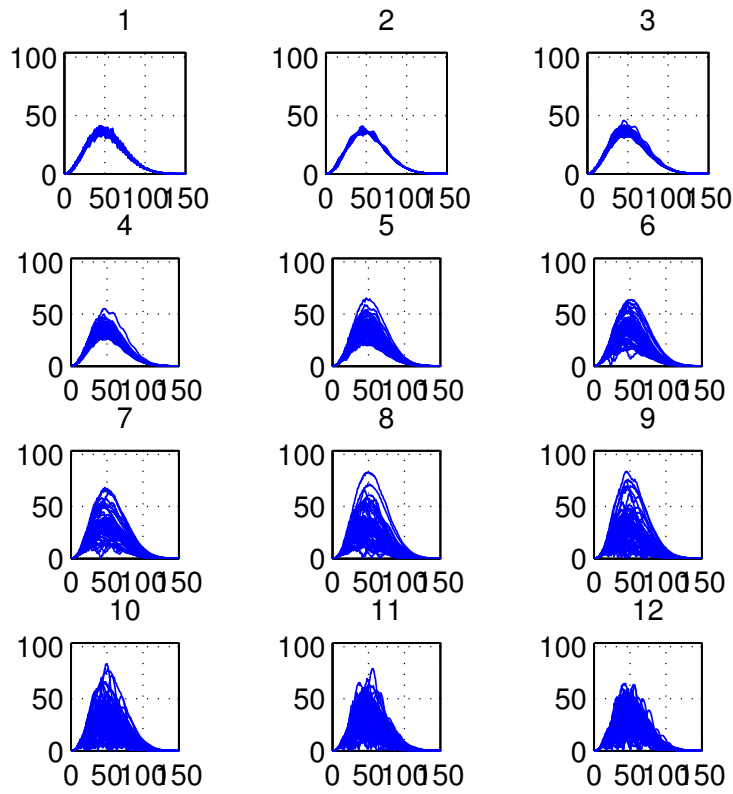


Figure 5.12: Amplitude spectra of scattered wavefields in isotropic media. The signals are recorded at 12 receiver lines with increasing propagation distance L (100 m per line). While for small L (subplot 1), the wavefield is coherent, coherence is lost as L increases, the variance increases and the mean amplitude diminishes

spectra increases. At the same time, one clearly observes a decrease in mean wave amplitude around the central frequency.

3. From the amplitude spectra, the relative log-amplitude variance χ is calculated, where only the contribution from the dominant frequency is considered. The procedure finally yields mean and variance of χ for every geophone line or propagation distance, respectively.

Results of the numerical experiments are shown in Figure 5.13. For varying angle of incidence and for two different degrees of anisotropy, the log-amplitude mean and variance are plotted as a function of propagation distance. In this 2-D anisotropic case and for small angles of incidence, the amount of amplitude variance can be quite well described by a combination of theoretical models for

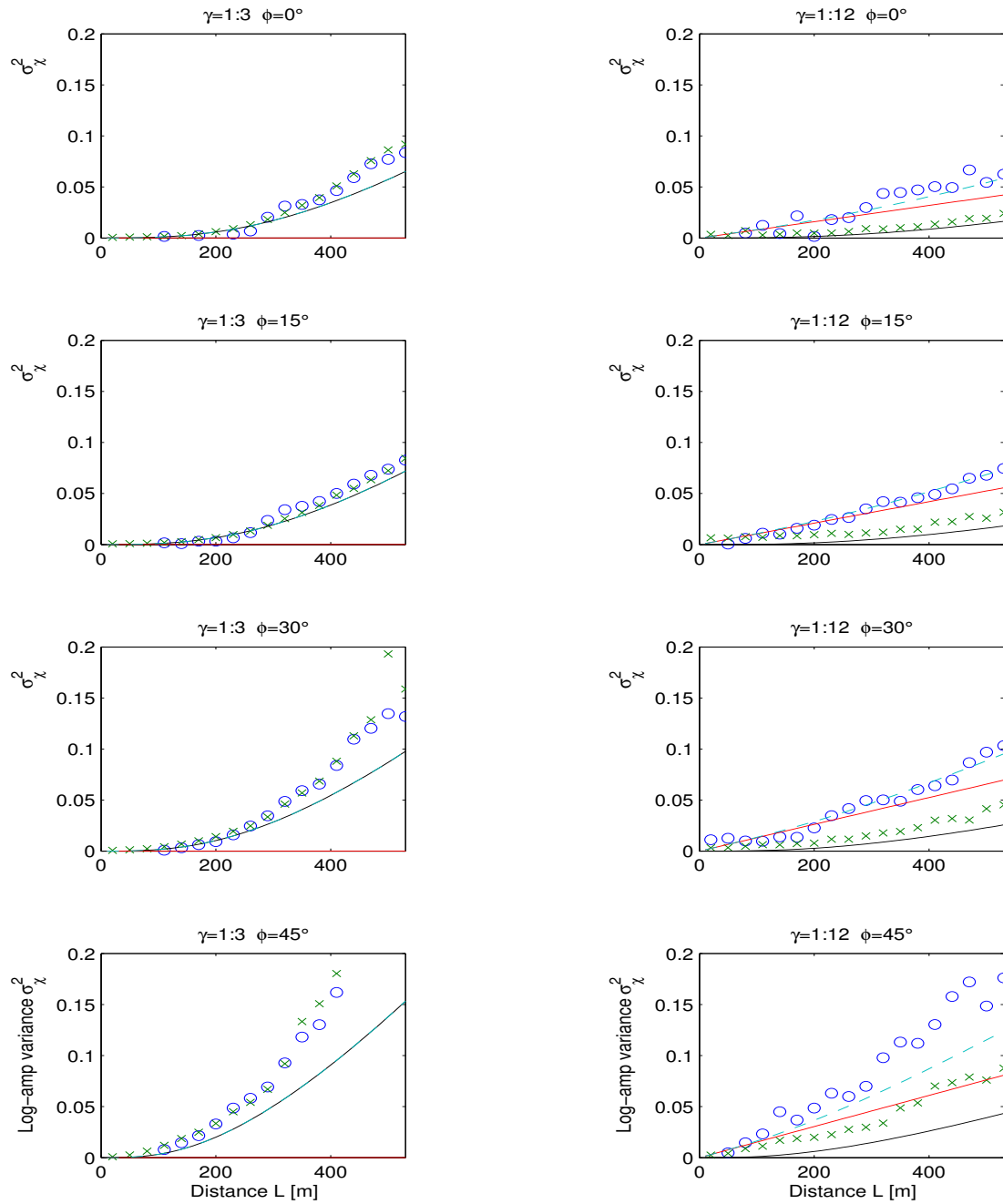


Figure 5.13: Log-amplitude variance of different angles of incidence ϕ and different degrees of anisotropy γ . Black lines are theoretical estimations, red lines show the contribution due to backscattering, blue dashed lines show the sum of both effects. The dots are mean values $-\langle\chi\rangle$ obtained from numerical computations and crosses are the corresponding variances.

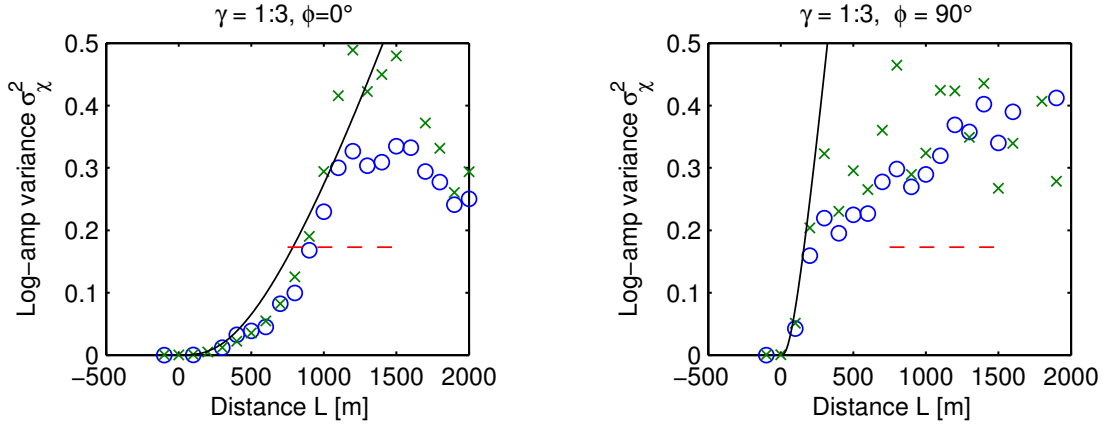


Figure 5.14: Behaviour of the log-amplitude variance for large propagation distances. Symbols and lines as in figure 5.13 but the red dashed line shows the theoretical saturation value that is attained in the long range limit.

backscattering and scattering attenuation due to diffraction. If the angle becomes larger, the initially plane wavefront is strongly perturbed and it becomes more and more difficult to extract the seismic primary from the whole wavefield. Hence, an evaluation of amplitude variance is not possible for large angles of incidence.

Furthermore, the application of the scattering theory is restricted to the regime of weak scattering, i. e. to short propagation distances. This condition is fulfilled if

$$\sigma_n^2 \frac{a_\xi}{a_\eta} (ka_\eta)^2 \frac{L}{a_\eta} < 1. \quad (5.34)$$

The evolution of the wavefield fluctuations at larger propagation distances is shown in Figure 5.14. While at small propagation distances, a strong increase of σ_{nn}^2 is observed that can be well described by the theoretical estimate, the numerically obtained values deviate from the theoretical prediction at larger propagation distances. Although there is a strong uncertainty in the numerical results, it seems that the amplitude variances saturate around a finite value.

Conclusions

Random poroelastic media are well-described by equivalent random elastic media if the frequency of the propagating fast wavemode is much below the critical relaxation frequency of wave-induced flow. In this case, the medium is unrelaxed and the elastic parameters are obtained by fluid substitution.

Attenuation effects in elastic random media with an anisotropic correlation function are governed by random diffraction and backscattering of the seismic wavefield. The theoretical description of scattering attenuation is based on esti-

inating the log-amplitude variance of the random wavefield.

In the case of strong anisotropy and for layered media, the effect of backscattering dominates for small angles of incidence or in other words if the wave hits the heterogeneities perpendicular to the long correlation axis. Diffraction and refraction occur dominantly in isotropic media and in anisotropic media at large angles of incidence, i. e. if the wave propagates along the long axis of the heterogeneity. Backscattering does not occur in isotropic and weak anisotropic media.

Using a superposition of theoretical estimates for diffraction and backscattering, the scattering attenuation in random media can be estimated for arbitrary angles of incidence. The theoretical estimates are, however, restricted to the weak fluctuation regime.

5.4 Wave-induced flow in random media

In the previous sections, wave-induced flow effects around poroelastic inclusions and elastic scattering in random media have been presented. The aim in this section to investigate both effects in a partially-saturated porous medium with fractal distribution of the fluid phases. The correlation function and correlation spectrum of fractal media is given in equations 2.103 and 2.106. A continuous random medium (CRM) realisation with dimension $L \times L = 256 \times 256$ cm, correlation length $a = 10$ cm and Hurst exponent $\nu = 0.3$ is shown in Figure 5.15b. The water saturation in this model varies between 0 and 100% with a mean saturation of 50%. Since the poroelastic FD solver does not explicitly include local saturation as a model parameter, the saturation maps are used to obtain a locally averaged effective fluid by arithmetic averaging the fluid density and viscosity as well as by geometrical Wood averaging of the fluid bulk modulus. This approach assumes that at scales not resolved by the FD grid, the pore pressure is locally equilibrated. By applying a threshold value at 0.5 to the continuous model, the binary medium (BRM) depicted in Figure 5.15a is obtained. This binary medium has piecewise 100% water or 100% gas saturation with a total saturation of 50%, like the continuous model. Material parameters for the fluids are given in Table 5.1 together with the parameters of the rock matrix that is assumed as a consolidated sandstone. Spatial resolution is $\Delta_x = 1$ cm, implying a minimum time step of 2μ s in order to ensure numerical stability.

For both models, two numerical FD experiments are carried out that are subsequently referred to as dynamic and quasistatic. While for the dynamic experiments, the source excitation is a short pulse with a wavelength λ smaller than the size of the model domain L , in the quasistatic experiments, a wavelength considerably larger than the model domain is chosen.

Therefore, the dynamic experiment is a plane wave propagation experiment,

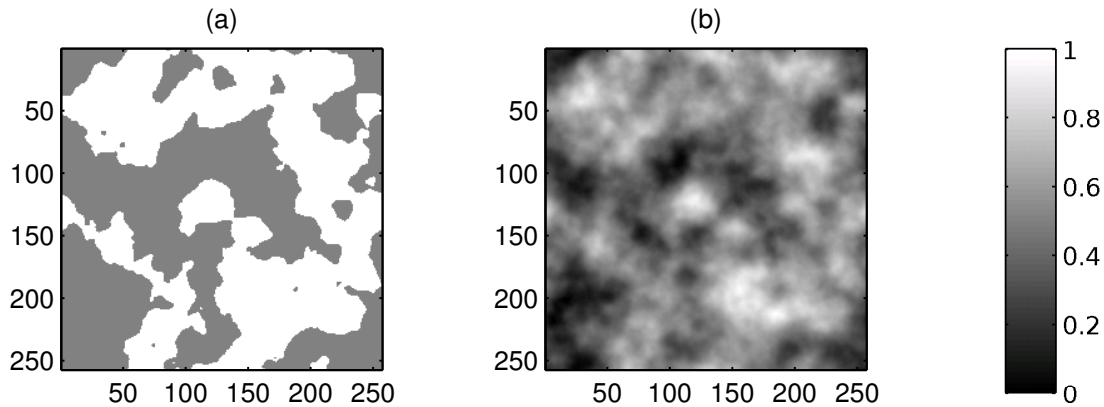


Figure 5.15: Synthetic saturation maps with fractal pore fluid distributions. (a) is a discrete distribution with white indicating water and grey indicating gas. It is derived from (b), showing water saturation with a continuous fractal distribution ($\nu = 0.3$).

similar to the scattering experiments presented in section 5.3. The applied source is a pure pressure pulse with source distribution parameter $q_p = 0$ and source time $t_s = 100\mu\text{s}$. As a source time function, a cubed sine is applied given by

$$\varphi_s(t, t_s) = \begin{cases} 0 & \text{if } t < 0 \vee t > t_s \\ \sin^3(\pi t/t_s) & \text{if } 0 < t < t_s \end{cases}. \quad (5.35)$$

Assuming a P -wave propagation velocity of approximately $c = 3000$ m/s, the dominant wavelength of the pulse is $\lambda = c/f = ct_s = 30\text{cm}$, which approximately equals the size of the medium heterogeneities.

Three snapshots of the pulse propagation are given Figure 5.17 for the binary random model and in Figure 5.16 for the continuous random model. Pore pressure is chosen to visualise the wave excitation. In the plots, white colour indicates negative pore pressure, while positive pressures appear in black. The lowermost subfigures show pore pressure profiles (grey lines) together with a stacked profile (solid black line) corresponding to the snapshot at $70\mu\text{s}$. From the snapshots, it is observed that the plane wave is scattered where the scattering is considerably stronger in the case of the binary medium if compared to the continuous medium.

In contrast to the dynamic wave propagation experiment, the quasistatic experiment uses a source excitation with a frequency content lower than the model resonance frequency $\omega_R = 2\pi c/L$. The setup is therefore comparable to the experiments presented in section 5.2. However, in order to avoid resonance effects included in the dynamic FD solution, a smoothed step load is applied at the model edge. In the quasistatic experiments presented here, a loading time of

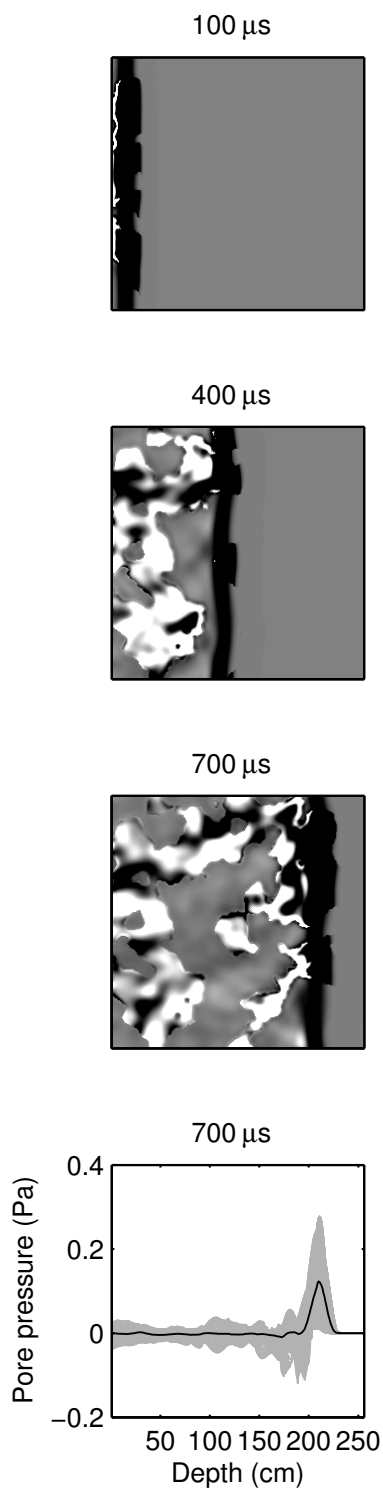


Figure 5.16: Pore pressure snapshots of dynamic wave propagation in the BRM model.

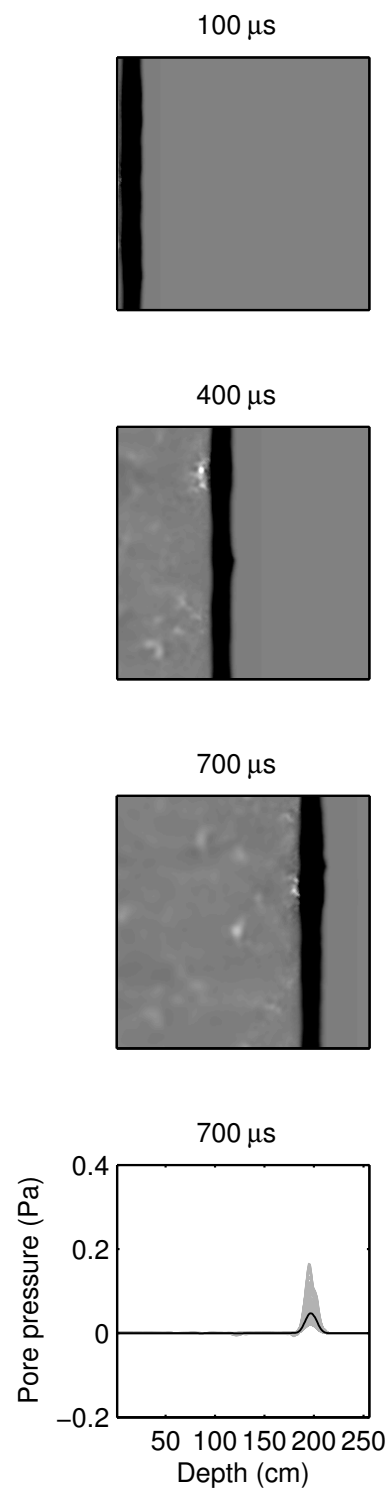


Figure 5.17: Same as 5.16 but for the CRM model. (Clipping also as in 5.16)

$t_s = 10\text{ms}$ is chosen with a source time function

$$\varphi_s^{\text{qs}}(t, t_s) = \varphi_s(t, t_s) * H(t) = \begin{cases} 0 & \text{if } t < 0 \\ \int_0^t \sin^3(\pi \tau / t_s) d\tau & \text{if } 0 < t < t_s \\ 1 & \text{if } t > t_s \end{cases} \quad (5.36)$$

In Figure 5.19 and 5.18, two snapshots of pore pressure distributions are shown for the binary random medium and the continuous random medium, respectively. For comparison, the pore pressure distributions of the unrelaxed states are given in the uppermost plot of each figure. Such an unrelaxed state is obtained by carrying out the same experiment under locally unrelaxed conditions, or in other words by setting the matrix permeability κ to zero such that no fluid flow may occur and the model behaves effectively elastic. The lowermost plots show profiles of the pore pressure distribution (grey lines) as well as a mean pore pressure profile (black line).

It is clearly observed that at the end of the loading stage ($t = t_s = 10\text{ms}$), internal pore pressure differences appear throughout the model. In regions with high water saturation, the pore pressure is high, while in areas with low water saturation, only little pore pressure is built up. The pore pressure distribution at $t = 10\text{ms}$ appears smoother than in the totally unrelaxed reference state, indicating that during the loading stage, a significant amount of fluid flow occurs, leading to a partial relaxation. During the equilibration stage ($t > t_s$) pore pressure differences decay with increasing time and eventually an equilibrium is attained. Characteristic for the pore pressure relaxation process is that small structures disappear quickly while larger structures persist longer. In order to incorporate the whole equilibration process, a simulation time of $100t_s = 1\text{s}$ is chosen. A comparison of the binary and the continuous modelling results reveals that in the latter case, the pore pressure distribution is qualitatively similar but the local differences in pore pressure are less pronounced. As the effective local bulk modulus of the CRM model is obtained by Wood averaging, this has to be expected. One should consider the CRM model to be partly relaxed from the very beginning of process, which is why the CRM model and the corresponding pore pressure distributions appear smoother.

In order to numerically quantify the effect of dynamic wave scattering and local flow on P -wave dispersion and attenuation, dynamic and quasistatic experiments are analysed by two different methods. Results are given in Figures 5.20 for the binary random medium and in Figure 5.21 for the continuous model.

First, from the seismograms of the dynamic wave propagation experiments, traveltimes are picked and mean wave amplitudes are assessed as a function of propagation distance. An attenuation estimate is obtained by linear regression of the relative log-amplitude decay (spectral ratio method). For this purpose, the confining pressure is chosen as the field parameter, since it shows less variance

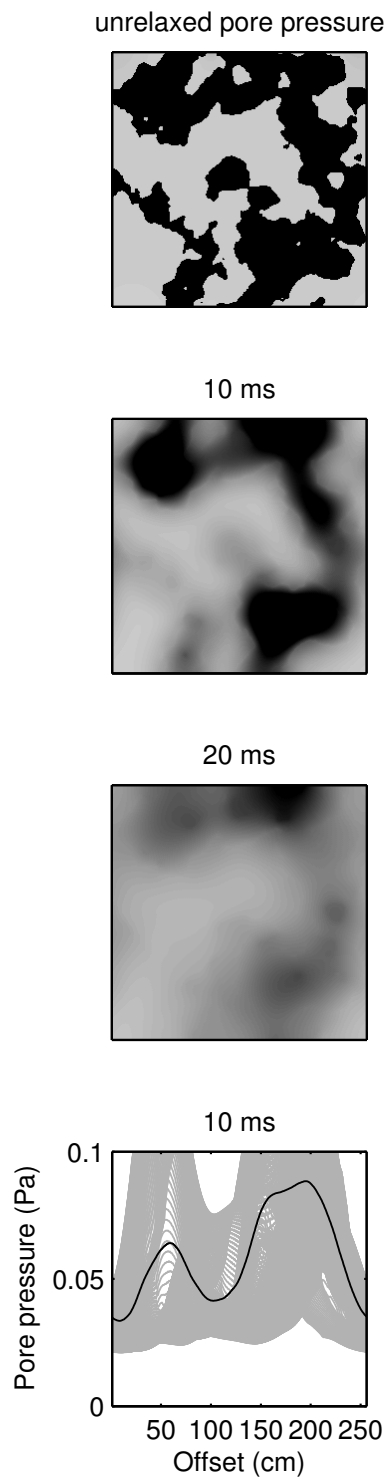


Figure 5.18: Quasistatic pore pressure relaxation in the BRM model.

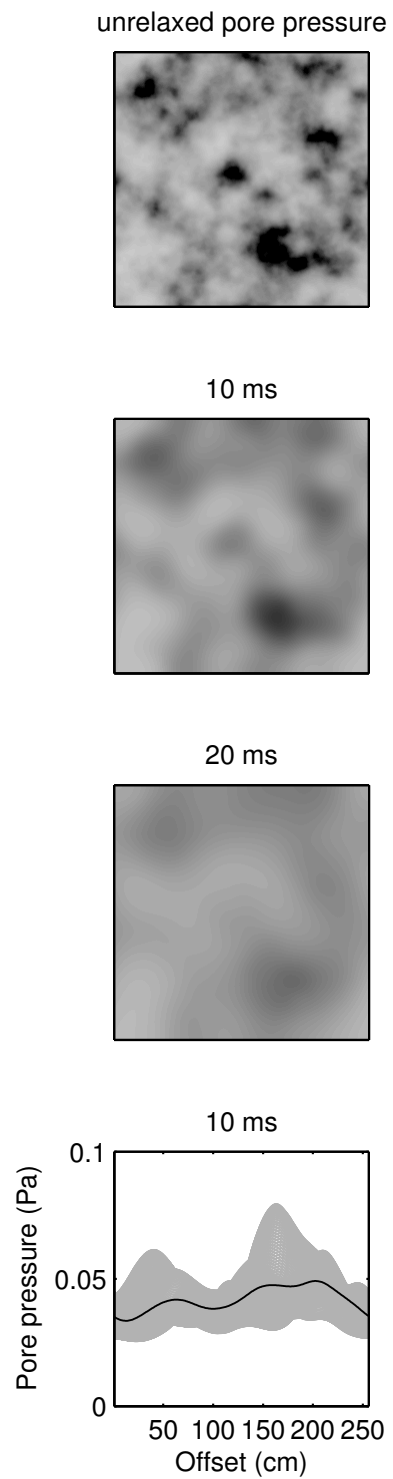


Figure 5.19: Same as 5.18 but for the CRM model. (Clipping also as in 5.18)

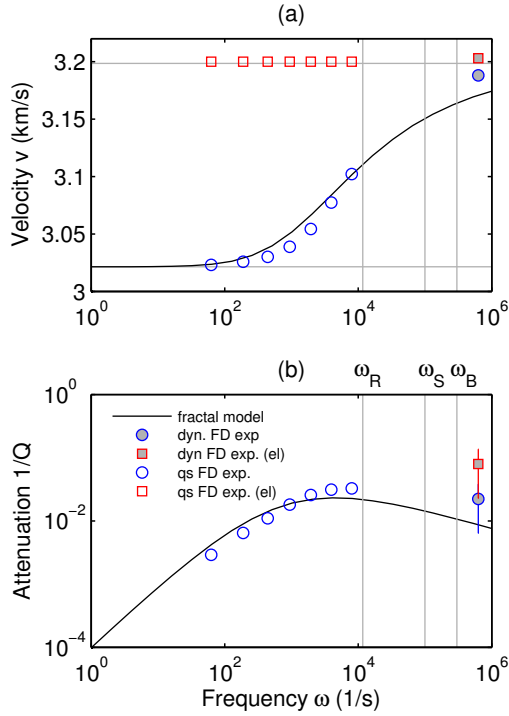


Figure 5.20: P -wave dispersion and attenuation in fractal media derived from quasi-static and dynamic FD experiments (BRM model). Numerical results – poroelastic and corresponding elastic – are compared to the theoretical model of fractal partial saturation. Dynamic scattering attenuation estimates are plotted with errorbars.

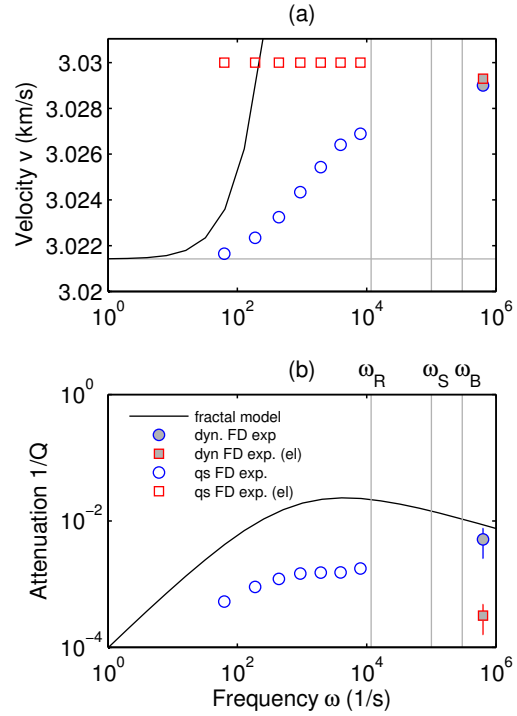


Figure 5.21: Same as 5.20 but for the CRM model. Note the different scaling of the vertical axis in (a). The horizontal lines in (a) show the Gassmann-Wood and Gassmann-Hill limits, vertical lines show the characteristic frequencies for resonance (ω_R), scattering (ω_S) and Biot global flow (ω_B).

due to saturation variations if compared to fluid pressure or particle velocities. Dispersion and attenuation values derived such are shown in Figures 5.20 and 5.21 as filled circles. Filled squares show dispersion and attenuation for the same dynamic experiment, but under unrelaxed conditions ($\kappa = 0m^2$). This corresponds to a wave propagation experiment in an equivalent elastic medium. For all scattering attenuation values, errorbars indicate variance of the numerical estimates.

Second, from mean stress and strain evolution during the quasistatic creep experiments, effective elastic properties are inferred that allow to quantify dispersion and attenuation at sub-resonant frequencies. For this purpose, stress and strain are averaged throughout the model domain. Following Masson and Pride (2007), effective shear, bulk and P -wave moduli are calculated from the complex Fourier spectra of stress and strain rates as

$$K^{2D}(\omega) = \frac{1}{2} \frac{\langle \dot{\tau}_{xx} \rangle + \langle \dot{\tau}_{zz} \rangle}{\langle \dot{\epsilon}_{xx} \rangle + \langle \dot{\epsilon}_{zz} \rangle}, \quad (5.37)$$

$$G^{3D}(\omega) = \frac{1}{2} \frac{\langle \dot{\tau}_{xx} \rangle - \langle \dot{\tau}_{zz} \rangle}{\langle \dot{\epsilon}_{xx} \rangle - \langle \dot{\epsilon}_{zz} \rangle}, \quad (5.38)$$

$$K^{3D}(\omega) = K^{2D} - \frac{1}{3}G^{3D}, \quad (5.39)$$

$$H^{3D}(\omega) = K^{3D} + \frac{4}{3}G^{3D}, \quad (5.40)$$

where for the calculation of 3-D moduli from 2-D fields, plane strain conditions are assumed. From the effective P -wave modulus H^{3D} , velocity dispersion and attenuation are derived according to equations 5.6 and 5.7. In Figures 5.20 and 5.21 they are denoted by unfilled circles. The unfilled squares in the dispersion subfigure correspond to the quasistatic response under unrelaxed conditions (see Figures 5.18a and 5.19a). Vertical lines show the frequencies corresponding to model resonance ω_R , characteristic scattering at medium heterogeneities ω_s and to the Biot frequency of the fully water-saturated rock ω_B . These frequencies are given by

$$\omega_R = \frac{2\pi c}{L}, \quad (5.41)$$

$$\omega_s = \frac{2\pi c}{a}, \quad (5.42)$$

$$\omega_B = \frac{b}{\rho^m}. \quad (5.43)$$

Eventually, the estimates of dynamic and quasistatic FD experiments are compared to an analytical solution for wave-induced flow in partially-saturated rock with fractal distribution of the pore fluids (Müller et al., 2008), as presented

in section 2.8. The predicted P -wave velocity varies between the theoretical limits of Gassmann-Wood and Gassmann-Hill that are shown as horizontal grey lines in the dispersion plots.

In Figure 5.20a, the dispersion behaviour obtained from the quasistatic experiment in the BRM is reasonably well described by the theoretical model of Müller et al. (2008). The Gassmann-Wood limit is obtained at low frequencies corresponding to the state of fully equilibrated pore pressure. As should be expected, for the unrelaxed elastic P -wave velocity, denoted by unfilled squares, the Gassmann-Hill limit is recovered. The velocities obtained from the dynamic experiments both are higher than the predicted effective velocity as indicated by the theoretical model and the velocity is highest for the equivalent elastic (unrelaxed) experiment. The bias in heterogeneous media towards higher propagation velocities is known as the fast path effect or velocity shift (e. g. Samuelides, 1998). As seen in Figure 5.20b, the quasistatic FD results for the BRM model also provide attenuation estimates that are comparable to that predicted by the theory. The characteristic frequency of maximum attenuation is approximately the same as well as the asymptotical behaviour at low frequencies. The quasistatic experiment of the corresponding elastic model does not show any attenuation. A possible explanation for the deviations of the numerically obtained attenuation values from the theoretical predictions may be the insufficient total size of the random medium realisation so that it may not be fully statistically representative.

The snapshots of the dynamic FD experiment shown in Figure 5.17 indicate that a considerable amount of scattering attenuation should be expected at these high frequencies. This is indeed observed, since the attenuation estimates derived from the poroelastic experiments are higher than the predicted attenuation due to wave-induced flow. The efficiency of scattering effects are also indicated by the observation that the scattering in the equivalent elastic BRM is stronger than in the poroelastic case.

Comparing the velocities and attenuation estimates of the CRM and the BRM model, one finds qualitatively similar behaviour but the amplitude of dispersion and attenuation are one order of magnitude smaller, see Figure 5.21. The reason for this is the usage of a locally averaged fluid bulk modulus as a model parameter. Consequently, in the unrelaxed state, the velocity is not in agreement with the Gassmann-Hill limit. The low-frequency Gassmann-Wood limit, however, is recovered by the quasistatic FD experiment. In addition to that, the medium heterogeneities appear much smoother in the CRM model and scattering attenuation is therefore reduced if compared to the BRM model.

The main purpose of the examples presented in this section is to show, how dispersion and attenuation are assessed over a large range of frequencies. Depending on the frequency range, the dominant loss effects in random porous media

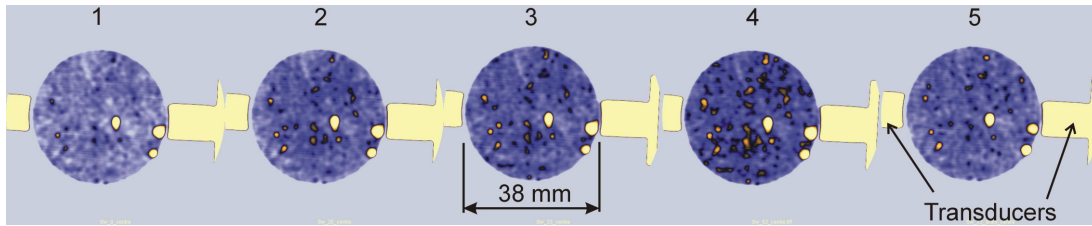


Figure 5.22: CT images of the Casino Otway Basin sandstone showing the evolution of fluid patches during a slow saturation experiment. The scans are taken at the same position for the dried sample (1), the sample at $t = 1\text{h}$ (2), at $t = 1\text{d}$ (3) up to 3d (4).

are wave-induced flow (at low frequencies with $\omega \ll \omega_s$) while at higher frequencies ($\omega \approx \omega_s$), classical scattering attenuation may also occur. The dynamic FD model does not only describe the quasistatic behaviour of heterogeneous porous rocks but allows also to simultaneously estimate scattering attenuation. If the frequencies are as high as the critical Biot frequency ω_B , inertial effects on the pore fluid flow are automatically included.

5.5 Simulation of ultrasonic laboratory experiments

The final application of poroelastic FD modelling presented in this thesis is concerned with an ultrasonic laboratory experiment carried out at CSIRO Petroleum, Perth, Australia. The scope of the experiment is to measure the development of fluid patches during water injection into an initially dry Casino Otway sandstone sample. Using 3-D computer tomography (CT) images of the fluid distribution are obtained and allow to experimentally study the parameters influencing the fluid distribution. Figure 5.22 shows an example of the evolution of transmissivity during a slow saturation experiment.

One experimental observation is that the characteristic scale of the fluid patches depends on the saturation level and on the fluid injection rate. This has a significant impact on the measured ultrasonic velocities, as shown in Figure 1.11 on page 13. In particular, the velocity-saturation relation shows a transition from the lower Gassmann-Wood bound to the upper Gassmann-Hill bound. Lebedev et al. (2009) interpreted the transition by the process of wave-induced fluid flow, i. e. by the interplay of slow P -wave creation at internal fluid-gas interfaces and the characteristic size of the fluid patches.

The interpretation of the laboratory results is further validated by FD simulation of quasistatic creep, similar to the example given in the preceding section

Table 5.2: Petrophysical properties of the dry Casino Otway sandstone sample used in the laboratory.

Bulk density ρ^b	(g/cm ³)	2.2
Grain density ρ^g	(g/cm ³)	2.65
Porosity ϕ		0.167
Permeability	(mD)	7.26

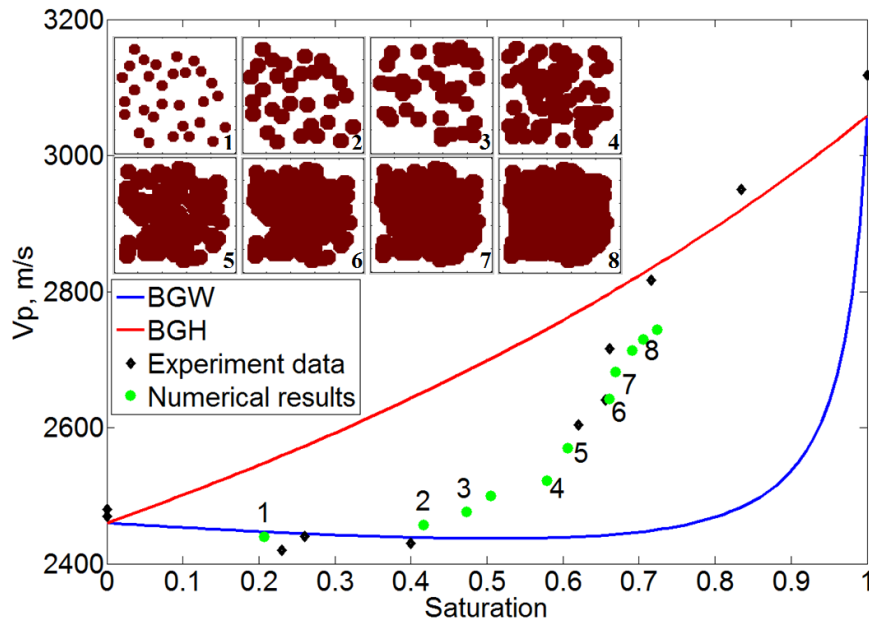


Figure 5.23: Velocity-saturation relation for partially saturated rock with random distribution of the fluid patches. Dispersion and attenuation in partially saturated rock.

5.4. Material properties in the simulation were chosen in accordance with the rock properties of the sandstone sample measured in the laboratory. Some of the properties are given in Table 5.2. The fluid geometry is represented by a random distribution of spherical water patches, where the saturation level is changed by increasing the diameter of the single patches. Eight different models are shown in Figure 5.23. While at low saturation, the fluid phase forms isolated pockets, the fluid patches start to cluster at higher saturation. This behaviour was chosen so that it resembles the saturation maps observed by CT scans. Numerically obtained propagation velocities are also given in Figure 5.23 together with the experimental results and the theoretical Gassmann-Wood and Gassmann-Hill bounds. Interestingly, although the simplified simulations are carried out in 2-D and although the fluid patch distribution was not derived directly from the CT scans, the numerical results show the same overall transitional behaviour from low

to high water saturations as the laboratory measurements. This indicates that ultrasonic velocities in partially-saturated rocks are governed by poroelastic effects as described by Biot theory. More precisely, transitional behaviour observed in the laboratory experiments is caused by the mechanism of wave-induced fluid flow.

5.6 Discussion

In this section, various numerical examples have been given that allow the quantitative description of wave-induced fluid flow and wave scattering in heterogeneous poroelastic media. For this purpose, a dynamic FD solver and a quasistatic FE tool have been applied for elastic and poroelastic rheologies. Here, the computational effort of the different experiments is briefly discussed. In addition to that, an explanation is given for the difference in the quasistatic relaxation behaviour of the 1-D and 3-D double porosity media presented in section 5.2.

In the seismic frequency range, the Biot slow wave degenerates to a purely diffuse wave mode. A numerical configuration to quantitatively estimate corresponding mesoscopic flow effects on velocity dispersion and attenuation has been presented in section 5.2 using a poroelastic FE solver. The approach is based on the relaxation of a heterogeneous rock sample and the results confirm that this modelling strategy is suitable for determining effective material properties. In order to obtain accurate results, it is necessary to resolve steep gradients of the pore pressure and stress fields occurring in the vicinity of internal boundaries. The gradients are strongest at the beginning of the relaxation experiment, and therefore the relaxation is also fastest at the beginning of the simulation and a small initial time step is required to ensure a sufficient temporal resolution. During the relaxation process, the time step can be increased. For a 3-D model where approximately 135000 linear tetrahedral elements are needed to discretise the elliptical inclusion, the CPU time for one simulation (60 time steps) is 14 hours on 10 nodes of the SGI Altix 350 located at the Geophysical Institute of Karlsruhe University. The model demands 8.9GB main memory.

The quasistatic experiment for estimating the effective properties of a random medium (section 5.4) was carried out on a regular 256×256 grid and took 2 hours on a four-way node of the HP-XC6000 Linux cluster of the Scientific Supercomputing Center Karlsruhe. Due to stability requirements a total of 500000 time steps is required, showing the problem of numerical stiffness as already discussed in sections 3.1.5 and 4.6. A corresponding FD experiment in a 3-D domain is not feasible and therefore, if the main interest is to quantify the induced diffusion process associated with compression and dilatation, numerical implementations of the quasistatic Biot equations are advantageous over explicit schemes

solving the fully dynamic equations. However, additional aspects such as wave scattering and inertial pore pressure effects are not modelled by a quasistatic solver. In summary, dynamic FD simulation tools are valuable for estimating high-frequency poroelastic scattering and diffusion. At low frequencies where diffusive pore pressure relaxation effects govern the dispersion and attenuation behaviour of poroelastic materials, the quasistatic FE solver should be applied.

In the elastic scattering experiments (section 5.3) the wavelengths are smaller than the medium correlation length and for one wavelength, 12 gridpoints are applied in order to prevent numerical dispersion. Furthermore, a sufficiently high number of heterogeneities is required for the statistical evaluation to be representative. This results into model sizes of about $2150 \times 8192 = 17.6$ Mio. gridpoints and with a time step size of 0.2ms a calculation of about 5000 timesteps is needed. On four two-way nodes of the HP-XC6000 Linux cluster, the computing time for one simulation is about 45 minutes. The computational effort of poroelastic wave propagation if compared to the elastic case is larger by a factor of about two, while the memory requirements are four times higher due to the larger number of field variables and material constants.

In section 5.2, a unidimensional layered double-porosity model and a 3-D model with an elliptical inclusion have been presented. One fundamental observation is that in the case of the layered medium, the normalised relaxation tensor ψ_{IJ}^n is isotropic. This can be explained by considering the possible paths of pore pressure equilibration. In the 1-D case, equilibration can only occur vertically between internal layers within the model, independent of what kind of deformation has been causing the pore pressure disequilibrium in the unrelaxed state. Consequently, there exists only one characteristic timescale of pore pressure relaxation, scaling with the characteristic layer period.

The situation is different in the case of a 3-D inclusion, which can be seen from the unrelaxed pore pressure distributions corresponding to the different applied deformation states. In Figure 5.24, these distributions are given for uniaxial compression and pure shear deformation such as associated with qP - and SH -waves under normal and grazing angles of incidence. The $\langle \varepsilon_{12} \rangle$ deformation state was obtained as the difference between the two horizontal uniaxial compression states as $p^{(\varepsilon_{12})} = p^{(\varepsilon_{11})} - p^{(\varepsilon_{22})}$. While in the case of uniaxial compression, pore pressure gradients appear mainly across the interface between the inclusion and the surrounding matrix, in the case of shear deformation, double couple distributions of pore pressure appear and fluid flow is induced mainly between different poles within the rock matrix. In addition to that, the spatial scale of pore pressure distribution under horizontal shear is larger than in the case of vertical shear, thus explaining the greater characteristic relaxation time of the corresponding relaxation function ψ_{66} , shown in Figure 5.7b.

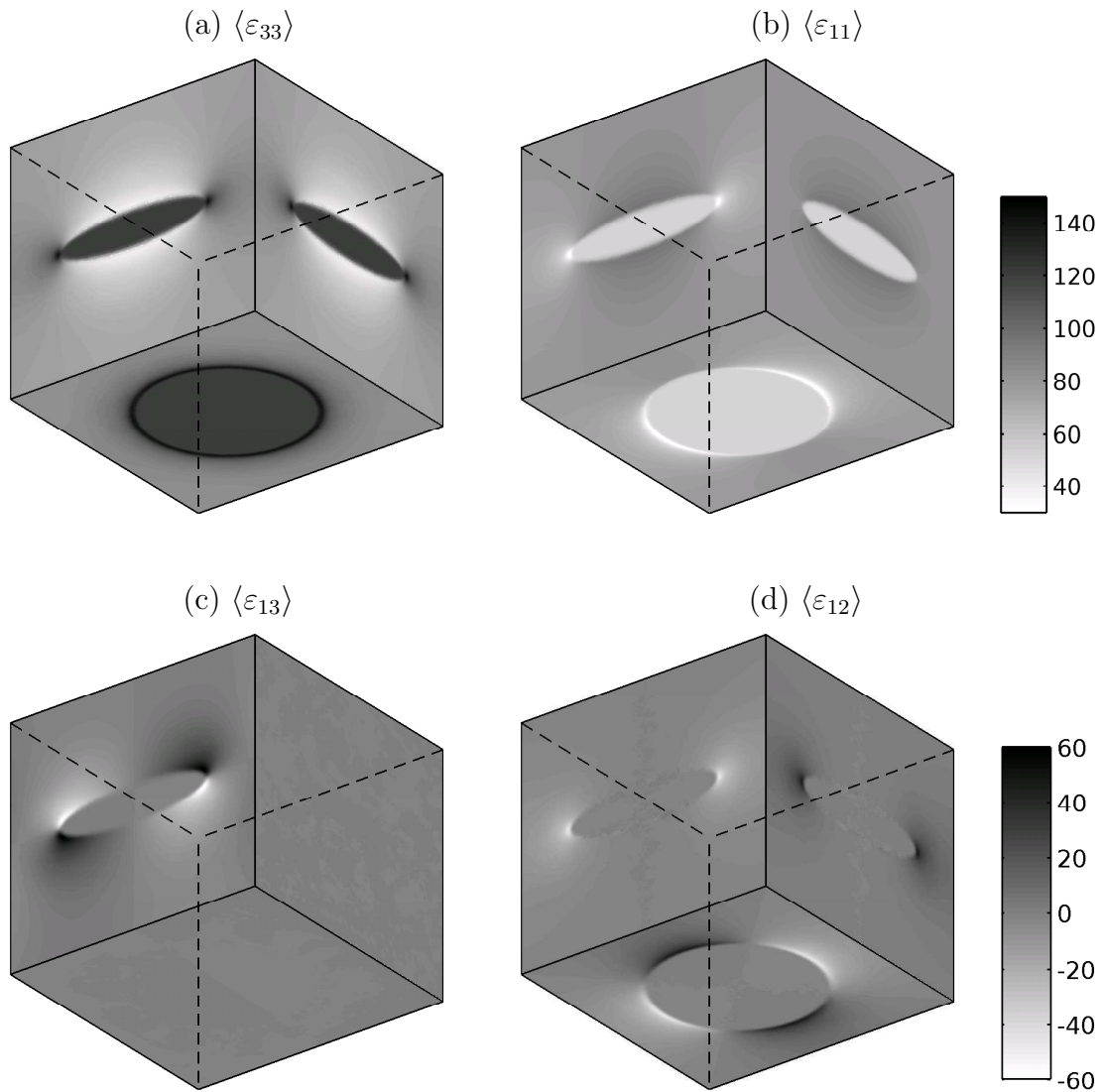


Figure 5.24: Unrelaxed pore pressure distributions in the 3-D FE model for different deformation states. The figures show profile cuts through the symmetry planes of the ellipsoidal inclusion, projected to the edges of modelling domain. Pore pressure response due to uniaxial compression in vertical (a) and horizontal (b) direction are shown as well as pure shear within the vertical (c) and horizontal (d) plane. The pore pressure distribution correspond to qP^0 -, qP^{90} -, SH^0 - and SH^{90} -waves, respectively.

Chapter 6

Conclusions and outlook

Wave scattering and mesoscopic flow of pore fluids are the main seismic attenuation mechanisms within geological reservoirs. Both mechanisms are described by the Biot equations of dynamic poroelasticity, i. e. by a set of two coupled, linear wave equations.

A new theoretical contribution to the rock physical description of porous rocks is made in the field of wave-induced flow in continuous random media (CRM). The CRM model has been extended such that it is now possible to estimate effective phase velocities and attenuation due to wave-induced flow in partially saturated media with a random fractal distribution of the pore fluids. This fractal distribution is described by the von-Kármán correlation function. If compared to CRM models with exponential or Gaussian correlation function, the fractal CRM model uses the Hurst exponent ν in addition to the medium variance and correlation length. It can be considered as an extension of the exponential CRM model.

The main achievement of this thesis is the development and implementation of a new velocity-stress finite-difference scheme for simulating wave propagation in heterogeneous, poroelastic structures. It solves Biot's equations of poroelasticity for a wide range of frequencies. The scheme is second order in time and includes higher-order spatial differentiation operators both on standard and rotated staggered grids. The scheme provides stable and accurate solutions even for strongly heterogeneous media. A poroelastic stability condition $\nu/\phi < \rho^f/\rho^b$ needs to be fulfilled in addition to the condition in elastic models. It has been shown that this condition is only critical when highly-porous inclusions such as cracks are modeled as free fluids.

In order to obtain accurate results, small-scale diffusion processes must be resolved, since the Biot equations behave numerically stiff at frequencies much below the critical Biot frequency ω_B . An appropriate estimate of the smallest process is given by the diffusion length λ_D , which has been introduced in the

context of numerical accuracy for the first time in this work. Insufficient resolution of internal diffusion processes results in a bias of the material behaviour towards the equivalent elastic response. The accuracy of the scheme is demonstrated by a series of numerical benchmark examples that show poroelastic effects occurring especially on the scale of several centimetres. The effects are thus mesoscale within the seismic frequency range.

It has been proved that the scalability of a poroelastic wave simulation is approximately linear. A test series revealed that the efficiency of the poroelastic wave simulation decreases with increasing parallelisation. However, an efficiency of 91% was obtained for a simulation involving 64 processes.

In the numerical investigation of purely mesoscopic phenomena such as wave-induced local flow, I found that a quasistatic FE solver that excludes inertial effects is usually advantageous if compared to a fully dynamic FD code. The problem of numerical stiffness, inherent in the dynamic description, can be circumvented this way. Effective, frequency-dependent elastic properties of heterogeneous poroelastic media can be efficiently and accurately determined from quasistatic relaxation or creep experiments. This has been successfully demonstrated in the case of partial saturation and for double porosity media, where the full, complex, frequency-dependent VTI stiffness tensor could be obtained. A fundamental observation for a layered double porosity medium is that the normalised relaxation tensor ψ_{IJ}^n is isotropic. This result has been used to generalise the theory of wave-induced fluid flow in layered porous structures at seismic frequencies. The suggested approach, however, allows to consider more general cases of arbitrary 3-D geometries.

Finite-difference modelling of the dynamic Biot equations contributes essentially to investigating the combined effects of macroscopic scattering and coupled fluid flow within heterogeneous reservoir rocks. This is particularly important at sonic frequencies used in acoustic borehole measurements and at ultrasonic frequencies such as applied for laboratory measurements. Finite-difference modelling has been indeed successfully applied for simulating a velocity-saturation relation measured in the laboratory, thus contributing to the interpretation of the measured data. Macroscopic scattering in the seismic frequency range is mainly due to purely elastic effects. Therefore, in this regime, an elastic FD solver can be applied for studying the scattering attenuation.

In summary, the results confirm that finite-difference and finite-element modelling are valuable tools to simulate wave propagation and coupled diffusion processes in heterogeneous poroelastic media, provided that all relevant temporal and spatial scales, in particular the scales of the diffusion process, are resolved properly. The applied numerical method should be chosen after careful analysing the characteristic frequency range of the investigated process.

In the near future, the most promising direction of poroelastic modelling is the direct numerical simulation of wave response within heterogeneous rock samples measured in the laboratory, of which an example was already presented in section 5.5. Recent developments show that x-ray tomography and digital core technology are increasingly used to characterise real rocks. Depending on the applied technology, the spatial resolution of these techniques varies between the pore scale to the scale of complete core samples. Obviously, 3-D images of real rock structures might be used as an input model for numerical tools such that propagation velocities, effective elastic parameters and hydraulic properties can be predicted by numerically solving the governing equations of poroelasticity. This represents a step beyond the synthetic heterogeneous rock samples constructed using random medium realisations with defined statistical properties. An important requirement for simulation of rock samples is the implementation of the presented poroelastic FD scheme in 3-D. This work is currently in progress.

Numerical experiments may furthermore allow to study combined effects of wave scattering and fluid flow in random porous media. The combination of quasistatic and dynamic experiments has a potential to separate the intrinsic and scattering attenuation. Another objective in current rock physics research is the quantification the interplay between elastic or hydraulic anisotropy and wave-induced flow. From a numerical point of view this requires additional work. Guided borehole waves or tube waves in the context of poroelasticity are increasingly used to characterise the permeability of fracture zones. Numerical tools may contribute to this field as well.

Finally, the simulation of poroelastic waves within double porosity structures surely deserves further consideration in the future, in particular for models with multiscale heterogeneities. One may even include poroelastic effects on the pore scale (Saenger et al., 2007), requiring the full resolution of the pore space. Although due the fine discretisation, pore scale modelling is restricted to very small domains on the millimetre scale, it may contribute to quantifying effects of grain scattering, pore space tortuosity and squirt flow or other effects that are beyond the description of Biot theory.

Appendix A

Viscoelasticity and quality factor

A material is called linear elastic, if stress and strain are proportional as described by Hooke's law $\tau = M\varepsilon$ and if deformation is fully reversible. Usually, in the case of wave propagation, the deformations are usually very small and the assumption of linearity is applicable. However, there is always a small amount of energy dissipated, resulting in a decay of wave amplitude. Such a behaviour can be macroscopically described by the concept of linear viscoelasticity. A constitutive law for this case is written (Aki and Richards, 1980)

$$\tau(t) = \dot{r}(t) * \varepsilon(t), \quad (\text{A.1})$$

where r is the relaxation function and the asterix denotes time convolution. A fundamental property of \dot{r} is causality ($\dot{r} = 0 \forall t < 0$) to ensure that future deformation states may not affect the present stress state. In addition to that, the more recent a deformation states is the larger is the impact on the stress and therefore $|\dot{r}|$ is a monotonically decreasing function of time. Finally, the principle of limited memory states that $\dot{r} \rightarrow 0$ for $t \rightarrow \infty$.

Using the convolution theorem $\mathcal{F}\{a * b\} = \mathcal{F}\{a\} \cdot \mathcal{F}\{b\}$, one writes in the frequency domain

$$\tau(\omega) = \tilde{M}(\omega) \varepsilon(\omega). \quad (\text{A.2})$$

A linear, viscoelastic material is therefore described by its relaxation function r or a complex, frequency-dependent modulus \tilde{M} being the spectrum of the relaxation rate \dot{r} . An elastic material is a special case of a viscoelastic material and it is characterised by instantaneous relaxation with $\dot{r}(t) = M_0\delta(t)$. Since $\delta(t) * \varepsilon = \varepsilon$ Hooke's law $\tau = M_0\varepsilon$ is recovered.

From time-domain numerical modelling, the effective complex modulus \tilde{M} of a heterogeneous sample can be obtained by a so-called relaxation experiment. For this purpose, a deformation $\varepsilon = H(t)$ is imposed on the sample, where $H(t)$ is the Heaviside step function. Inserting this into the constitutive relation A.1

and recalling that $a * H = \int a \, dt$ yields

$$\tau = \dot{r} * H = \int_0^t \dot{r} \, dt = r, \quad (\text{A.3})$$

i. e. the relaxation function is nothing but the stress response to a relaxation test! Therefore, the complex modulus \tilde{M} can be obtained by time differentiation of the stress response followed by a Fourier transform. This strategy is depicted in Figure A.1, showing strain, stress and rate-of-change of stress as a function of time. The counterpart of the relaxation test – the creep test – is also depicted in the same figure: Applying instantaneously a constant load $\tau = H(t)$ results in a strain response that equals the creep function f . Note that the numerical evaluation of \dot{r} at $t = 0$ requires special care due to the step change in the stress response. It is convenient to write the relaxation function r as a sum of instantaneous (elastic) and delayed (viscoelastic) relaxation such that

$$r(t) = M_u[H(t) + \psi(t)], \quad (\text{A.4})$$

$$\dot{r}(t) = M_u[\delta(t) + \dot{\psi}(t)]. \quad (\text{A.5})$$

M_u is the so-called unrelaxed modulus, while the relaxed modulus is M_r , see Figure A.1. Applying the Fourier transform to equation A.5 provides the modulus \tilde{M} as

$$\tilde{M}(\omega) = \mathcal{F}\{\dot{r}(t)\} = M_u[1 + \mathcal{F}\{\dot{\psi}(t)\}]. \quad (\text{A.6})$$

In order to quantify the energy dissipation associated with linear viscoelasticity, the time-harmonic deformation $\varepsilon = \varepsilon_0 \exp(i\omega t)$ is inserted into equation A.2. Writing $\text{Re } \tilde{M} = \tilde{M}_R$ and $\text{Im } \tilde{M} = \tilde{M}_I$, the energy dissipated in one cycle is

$$\Delta W = \int_{\omega t=0}^{2\pi} \tau \, d\varepsilon = \pi \tilde{M}_I \varepsilon_0^2, \quad (\text{A.7})$$

while the maximum stored energy is

$$W = \int_{\omega t=0}^{\pi/2} \tau \, d\varepsilon = \frac{\tilde{M}_R}{2} \varepsilon_0^2. \quad (\text{A.8})$$

The relative dissipated energy per one cycle is therefore

$$\frac{\Delta W}{W} = 2\pi \frac{\tilde{M}_I}{\tilde{M}_R} \quad (\text{A.9})$$

and the fraction of imaginary and real part of the complex modulus is used as a definition for the inverse quality factor

$$Q^{-1} = -\frac{\tilde{M}_I}{\tilde{M}_R}. \quad (\text{A.10})$$

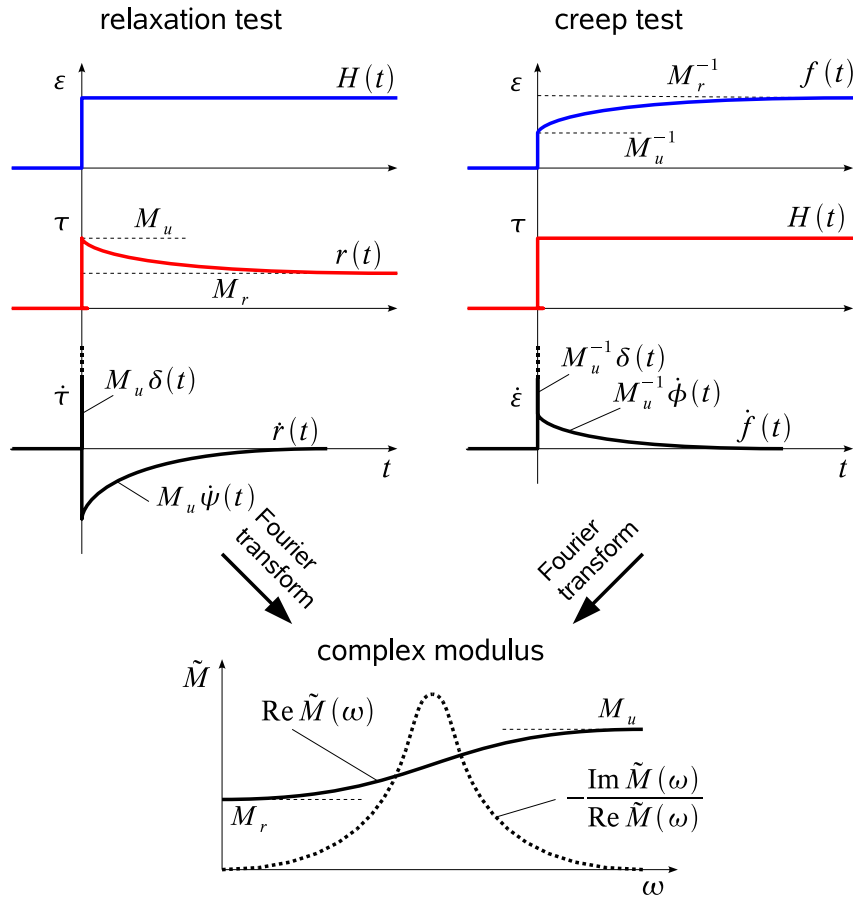


Figure A.1: Relaxation and creep test for the evaluation of the complex modulus $\tilde{M}(\omega)$. The curves show the applied stress and strain, as well as stress and strain rates, respectively. In the relaxation test, the stress response is identified as the relaxation function r and its derivative can be presented according to equation A.4. In the creep test, the strain response is called creep function f . The complex modulus is obtained alternatively from the creep rate \dot{f} or relaxation rate \dot{r} by Fourier transform.

For non-dissipative media, \tilde{M}_I is zero and the dimensionless quality factor vanishes.

As already mentioned, the absorbing behaviour of viscoelastic materials leads to attenuation of seismic waves. This is easily exemplified by considering the viscoacoustic wave equation

$$\rho \ddot{u} = \dot{r} * \nabla^2 u \quad (\text{A.11})$$

that can be solved by the inserting the plane wave ansatz

$$u = u_0 \exp[i(\tilde{k}x - \omega t)]. \quad (\text{A.12})$$

Here, \tilde{k} is the complex wavenumber with real part k and imaginary part α . The quantity α is referred to as attenuation coefficient since substituting $\tilde{k} = \kappa + i\alpha$ into equation A.12 yields

$$u = u_0 \exp[-\alpha x] \exp[i(\kappa x - \omega t)], \quad (\text{A.13})$$

revealing that α describes an exponential decay of wave amplitude with propagation distance x . By inserting A.13 into the wave equation A.11 it can be shown that the relation between real and imaginary part of the wavenumber \tilde{k} is related to the real and imaginary parts of the complex modulus \tilde{M} (and therefore Q^{-1}) as

$$Q^{-1} = -\frac{\tilde{M}_I}{\tilde{M}_R} = -\frac{\text{Im } \tilde{k}^{-2}}{\text{Re } \tilde{k}^{-2}} = \frac{\text{Im } \tilde{k}^2}{\text{Re } \tilde{k}^2} = \frac{2\alpha\kappa}{\kappa^2 - \alpha^2} \stackrel{\alpha \ll \kappa}{\approx} \frac{2\alpha}{\kappa} = 2 \frac{\text{Im } \tilde{k}}{\text{Re } \tilde{k}}. \quad (\text{A.14})$$

The quality factor Q is either calculated from the complex modulus \tilde{M} or from the complex wavenumber \tilde{k} .

A final remark is now made on the relation between wave attenuation and velocity dispersion. The causality of \dot{r} implies that its spectrum is hermitian, such that the real and imaginary parts of \tilde{M} form a Hilbert transform pair. Abbreviating $\tilde{M}_0 = \tilde{M}_R(0)$, one obtains the Kramers-Kronig relations (Mavko et al., 1998)

$$\tilde{M}_R(\omega) - \tilde{M}_0 = -\frac{\omega}{\pi} \int_{-\infty}^{\infty} \frac{\tilde{M}_I(\omega')}{\omega'} \frac{d\omega'}{\omega' - \omega}, \quad (\text{A.15})$$

$$\tilde{M}_I(\omega) = \frac{\omega}{\pi} \int_{-\infty}^{\infty} \frac{\tilde{M}_R(\omega') - \tilde{M}_0}{\omega'} \frac{d\omega'}{\omega' - \omega}. \quad (\text{A.16})$$

The meaning of the Kramers-Kronig relations is that real and imaginary parts of the relaxation spectrum are not independent. Since in the context of wave propagation, \tilde{M}_I is related to wave attenuation and \tilde{M}_R to wave dispersion, the important implication is that attenuation is always accompanied by velocity dispersion. In many theoretical models, the causality principle is used to constrain the solution for the complex wavenumber.

Appendix B

Statistical characterisation of random media

In several parts of this work, elastic and poroelastic parameters as well as scattered waves have been considered as random fields. E. g. in section 2.8.2, the complex wavenumber of compressional waves in random porous media may depend on the statistical properties of the underlying medium. In this appendix, a short summary of the applied statistical notation is given.

Consider a random field $X(\mathbf{x})$. By defining the averaging operator as in equation 2.82, one obtains the mean value of X as

$$\langle X \rangle = \frac{1}{V} \int_{\text{REV}} X(\mathbf{x}) \, dV. \quad (\text{B.1})$$

The integration volume V in this case must be sufficiently large so that it can be considered as representative for the whole medium. It is then referred to as representative elementary volume (REV). Averaging is a linear operation, such that commutative and associative laws apply. The variance of X are defined as

$$\tilde{\sigma}_{XX}^2 = \langle (X - \langle X \rangle)^2 \rangle = \langle X^2 \rangle - \langle X \rangle^2. \quad (\text{B.2})$$

It is usually presented in normalised form as

$$\sigma_{XX}^2 = \frac{\tilde{\sigma}_{XX}^2}{\langle X \rangle^2} = \frac{\langle X^2 \rangle}{\langle X \rangle^2} - 1 \quad (\text{B.3})$$

and is used as a measure of the strength of fluctuation of the random field X . The variance can also be written in terms of the normalised square fluctuation

$$n = \frac{X}{\langle X \rangle} - 1 \quad (\text{B.4})$$

as

$$\sigma_{XX}^2 = \langle n^2 \rangle. \quad (\text{B.5})$$

The autocorrelation function (or simply correlation function) characterises the spatial distribution of X and is calculated as

$$B(\mathbf{r}) = \langle n(\mathbf{x}) n(\mathbf{x} + \mathbf{r}) \rangle . \quad (\text{B.6})$$

A random medium is called isotropic (sometimes isomeric to avoid confusion with the material isotropy) if B only depends on the absolute value of $\mathbf{r} = r$. Otherwise the medium is anisotropic or more precisely it is anisotropically correlated. It has the property $B(\mathbf{0}) = \sigma_{XX}^2$ and usually $B(\mathbf{r}) \rightarrow 0$ for large values of \mathbf{r} . Examples of typical correlation functions are the Gaussian bell or exponential function as depicted with associated random media realisations in Figure 2.9 on page 37. The Gaussian correlation function is given by

$$B^{\text{gauss}}(r) = \sigma_{XX}^2 \exp\left(-\frac{r^2}{a^2}\right) \quad (\text{B.7})$$

where a is the so-called correlation length. It is the characteristic lengthscale of the medium, since the two points are correlated if $r = |\mathbf{x}_1 - \mathbf{x}_2| \approx a$, but for $r \gg a$ the two points are uncorrelated.

Obviously, in anisotropic random media as applied in section 5.3, two or more correlation parameters are required to describe the degree of anisotropy. In this case, B also depends on the orientation of the main axes of the correlation function with respect to the global coordinate system. In 2-D, the anisotropic Gaussian correlation function is

$$B^{\text{gauss}}(r_x, r_y, \phi) = \sigma_{XX}^2 \exp\left(-\frac{r_x^2}{a_\xi^2} - \frac{r_y^2}{a_\eta^2}\right) . \quad (\text{B.8})$$

with

$$\begin{pmatrix} X_\xi \\ X_\eta \end{pmatrix} = \begin{pmatrix} \cos \phi & \sin \phi \\ -\sin \phi & \cos \phi \end{pmatrix} \begin{pmatrix} X_x \\ X_y \end{pmatrix} . \quad (\text{B.9})$$

For exponentially or fractal correlated media, the anisotropic formulation is done accordingly. More details on the characterisation of random media in the context of wave field scattering are found in the textbooks of Uscinski (1977), Ishimaru (1978), Rytov et al. (1989) or Sato and Fehler (1998).

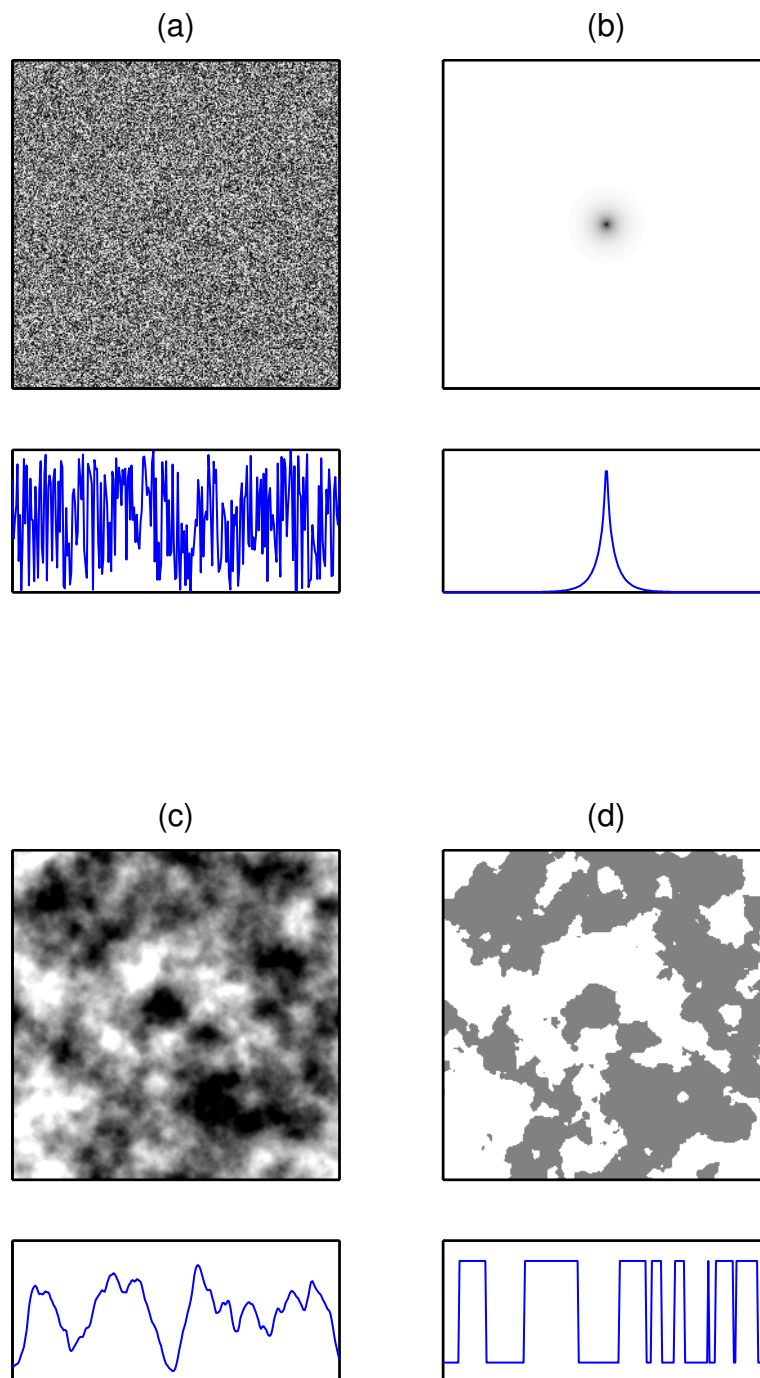


Figure B.1: Procedure of creating random media realisations. Beginning with a random medium with uncorrelated properties (a), a continuous random medium with defined correlation properties (c) is obtained by convolution of the uncorrelated medium with the spatial correlation function (b). A binary random medium (d) is obtained from the CRM by applying a threshold value, in this case the mean of the CRM.

Appendix C

Supplementary rock physics formulas

Mathematical models describing waves in porous media have been presented in chapter 2. In this appendix, some additional rock physics formulas are given without derivation or extensive discussion. This includes the high-frequency Biot theory, poroelastic Backus averaging and further remarks on models for wave-induced fluid flow.

C.1 High frequency correction for the Biot equations

At frequencies higher than the Biot frequency ω_B , the evolution of boundary layers on the scale of the pore diameter. For completeness, an expression for the viscodynamic operator as derived by Biot (1956b) is provided here. It reads

$$\tilde{Y}(\iota\omega) = \rho^m \iota\omega + bF(\xi), \quad (\text{C.1})$$

where the operator $F(\xi)$ incorporates the frequency dependence of viscous drag in the pore channels. It is defined as (Mavko et al., 1998)

$$F(\xi) = \frac{1}{4} \frac{\xi T(\xi)}{1 + 2\iota T(\xi)/\xi} \quad (\text{C.2})$$

$$T(\xi) = \frac{\text{ber}'(\xi) + \iota \text{bei}'(\xi)}{\text{ber}(\xi) + \iota \text{bei}(\xi)} = \exp(\iota\pi 3/4) \frac{J_1(\xi \exp(-\iota\pi/4))}{J_0(\xi \exp(-\iota\pi/4))} \quad (\text{C.3})$$

$$\xi = \left(\frac{\omega a^2 \rho^f}{\eta} \right)^{1/2} \quad (\text{C.4})$$

Here, bei and ber denote the imaginary and the real parts of the Kelvin function and J_n denotes the Bessel function of order n . The quantity a is the pore

size parameter that depends on dimensions and the shape of the pore space. At frequencies below ω_c , the operator F approaches 1 and the low-frequency approximation of the viscodynamic operator \tilde{Y} is recovered.

C.2 Poroelastic Backus average

Due to their genesis, sedimentary rocks are often found to have strong variations in vertical direction while they are laterally more or less homogeneous. Therefore, it is reasonable to describe such rocks as a stack of layers and the effective elastic properties of a layered rock are calculated by using the Backus average (Backus, 1962). In the case of poroelastic layering, Backus-type formulas have been given by Gelinsky and Shapiro (1997). The authors provide averaging formulas for the two limiting cases of unrelaxed and relaxed effective material response, where the unrelaxed response is identical with the elastic Backus average. They refer to these limits as no-flow and quasistatic, respectively. In this section, the presentation is restricted to the case of isotropic layers that result in overall VTI material behaviour.

Such a VTI medium is characterised by five independent elastic moduli that determine the stiffness effective tensor c_{ijkl} or in compact notation

$$c_{IJ} = \begin{pmatrix} A & B & F & 0 & 0 & 0 \\ B & A & F & 0 & 0 & 0 \\ F & F & C & 0 & 0 & 0 \\ 0 & 0 & 0 & D & 0 & 0 \\ 0 & 0 & 0 & 0 & D & 0 \\ 0 & 0 & 0 & 0 & 0 & J \end{pmatrix} \quad (\text{C.5})$$

with $J = 1/2(A - B)$. In the no-flow limit or unrelaxed limit, the elastic moduli are calculated as

$$A_u = \left\langle \frac{4\mu(\lambda + \mu)}{\lambda + 2\mu} \right\rangle + \left\langle \frac{1}{\lambda + 2\mu} \right\rangle^{-1} \left\langle \frac{\lambda}{\lambda + 2\mu} \right\rangle^2, \quad (\text{C.6})$$

$$B_u = \left\langle \frac{2\mu\lambda}{\lambda + 2\mu} \right\rangle + \left\langle \frac{1}{\lambda + 2\mu} \right\rangle^{-1} \left\langle \frac{\lambda}{\lambda + 2\mu} \right\rangle^2, \quad (\text{C.7})$$

$$C_u = \left\langle \frac{1}{\lambda + 2\mu} \right\rangle^{-1}, \quad (\text{C.8})$$

$$F_u = \left\langle \frac{1}{\lambda + 2\mu} \right\rangle^{-1} \left\langle \frac{\lambda}{\lambda + 2\mu} \right\rangle, \quad (\text{C.9})$$

$$D_u = \left\langle \frac{1}{\mu} \right\rangle^{-1}. \quad (\text{C.10})$$

Here, λ and μ are the *undrained* Lamé parameters

$$\lambda = \lambda_u = K_d + \frac{2}{3}G + \alpha^2 M \quad (\text{C.11})$$

$$\mu = G. \quad (\text{C.12})$$

A different set of equations is used to calculate the moduli in the relaxed case with equilibrated pore pressure. Then, one has

$$A_r = \left\langle \frac{4\mu(\lambda + \mu)}{\lambda + 2\mu} \right\rangle + \left\langle \frac{1}{\lambda + 2\mu} \right\rangle^{-1} \left\langle \frac{\lambda}{\lambda + 2\mu} \right\rangle^2 + \frac{X^2}{Z}, \quad (\text{C.13})$$

$$B_r = \left\langle \frac{2\mu\lambda}{\lambda + 2\mu} \right\rangle + \left\langle \frac{1}{\lambda + 2\mu} \right\rangle^{-1} \left\langle \frac{\lambda}{\lambda + 2\mu} \right\rangle^2 + \frac{X^2}{Z}, \quad (\text{C.14})$$

$$C_r = \left\langle \frac{1}{\lambda + 2\mu} \right\rangle^{-1} + \frac{XY}{Z}, \quad (\text{C.15})$$

$$F_r = \left\langle \frac{1}{\lambda + 2\mu} \right\rangle^{-1} \left\langle \frac{\lambda}{\lambda + 2\mu} \right\rangle + \frac{XY}{Z}, \quad (\text{C.16})$$

$$D_r = \left\langle \frac{1}{\mu} \right\rangle^{-1}, \quad (\text{C.17})$$

but now, the *drained* Lamé parameters are used

$$\lambda = \lambda_d = K_d + \frac{2}{3}G. \quad (\text{C.18})$$

X , Y and Z are calculated as

$$X = -Z \left(\left\langle \frac{2\alpha\mu}{\lambda + 2\mu} \right\rangle + \left\langle \frac{\alpha}{\lambda + 2\mu} \right\rangle \left\langle \frac{\lambda}{\lambda + 2\mu} \right\rangle \left\langle \frac{1}{\lambda + 2\mu} \right\rangle^{-1} \right), \quad (\text{C.19})$$

$$Y = -Z \left\langle \frac{\alpha}{\lambda + 2\mu} \right\rangle \left\langle \frac{1}{\lambda + 2\mu} \right\rangle^{-1}, \quad (\text{C.20})$$

$$Z = \left\langle \frac{1}{M} \right\rangle + \left\langle \frac{\alpha^2}{\lambda + 2\mu} \right\rangle - \left\langle \frac{\alpha}{\lambda + 2\mu} \right\rangle \left\langle \frac{\lambda}{\lambda + 2\mu} \right\rangle \left\langle \frac{1}{\lambda + 2\mu} \right\rangle^{-1}. \quad (\text{C.21})$$

Once the coefficients A , B , C , F and D are known, phase velocities are determined straightforward. The three possible modes of propagation in anisotropic media are called quasi-longitudinal (qP), quasi-shear (qSV) and pure shear (SH), respectively. In VTI media, the velocities are a function of angle of incidence θ . Abbreviating

$$Q = [(A - D) \sin^2 \theta - (C - D) \cos^2 \theta]^2 + (F + D)^2 \sin^2 \theta \quad (\text{C.22})$$

they are given by (Mavko et al., 1998)

$$v_{qP} = \sqrt{\frac{A \sin^2 \theta + C \cos^2 \theta + D + \sqrt{Q}}{2\rho^b}}, \quad (\text{C.23})$$

$$v_{qSV} = \sqrt{\frac{A \sin^2 \theta + C \cos^2 \theta + D - \sqrt{Q}}{2\rho^b}}, \quad (\text{C.24})$$

$$v_{SH} = \sqrt{\frac{J \sin^2 \theta + D \cos^2 \theta}{\rho^b}}. \quad (\text{C.25})$$

In the case of zero angle of incidence $\theta = 0^\circ$, i. e. if the wave vector and the symmetry axis are collinear, the expressions simplify to

$$v_{qP}^0 = \sqrt{\frac{C}{\rho^b}}, \quad (\text{C.26})$$

$$v_{qSV}^0 = v_{SH}^0 = \sqrt{\frac{D}{\rho^b}}, \quad (\text{C.27})$$

and for $\theta = 90^\circ$ one obtains

$$v_{qP}^{90} = \sqrt{\frac{A}{\rho^b}}, \quad (\text{C.28})$$

$$v_{qSV}^{90} = \sqrt{\frac{D}{\rho^b}}, \quad (\text{C.29})$$

$$v_{SH}^{90} = \sqrt{\frac{J}{\rho^b}}. \quad (\text{C.30})$$

A convenient notation for weak anisotropy was suggested by Thomsen (1986). According to his work, the angle-dependent phase velocities are written as a product of the qP - and qSV -wave velocities at zero incidence, with combinations of the Thomsen parameters ε , γ and δ (Mavko et al., 1998)

$$v_{qP} \approx v_{qP}^0 (1 + \delta \sin^2 \theta \cos^2 \theta + \varepsilon \sin^4 \theta), \quad (\text{C.31})$$

$$v_{qSV} \approx v_{qSV}^0 \left(1 + \frac{\alpha^2}{\beta^2} (\varepsilon - \delta) \sin^2 \theta \cos^2 \theta \right), \quad (\text{C.32})$$

$$v_{SH} \approx v_{qSV}^0 (1 + \gamma \sin^2 \theta). \quad (\text{C.33})$$

with

$$\varepsilon = \frac{A - C}{2C}, \quad (\text{C.34})$$

$$\gamma = \frac{J - D}{2D}, \quad (\text{C.35})$$

$$\delta = \frac{(F + D)^2 + (C - D)^2}{2C(C - D)}. \quad (\text{C.36})$$

Note that the approximation using the Thomson notation is only valid for small anisotropy, i. e. for $\varepsilon, \gamma, \delta \ll 1$.

C.3 Extended theory of wave-induced flow in layered porous media

In section 5.2, it was shown that in layered porous media, the relaxation tensor can be presented as a product of its low-frequency limit ψ_{IJ}^0 and the normalised relaxation function $\psi^n(t)$ such that

$$\tilde{c}_{IJ}(\omega) = c_{IJ}^u(1 + \mathcal{F}\{\psi^n(t)\})\psi_{IJ}^0 \quad (\text{C.37})$$

Here, the $\psi_{IJ}^0 = c_{(IJ)}^r/c_{(IJ)}^u - 1$ is obtained from the poroelastic Backus average as explained in the preceding section (Gelinsky and Shapiro, 1997) and $\psi^n(t)$ can be calculated from the frequency-dependent solution for the effective P -wave modulus (e. g. Gurevich and Lopatnikov, 1995; Brajanovski et al., 2006). From a practical point of view, this result can be used to derive an estimate of the attenuation of P - SV -waves in layered porous media. Consider the layered double porosity model presented in section 5.2. Limits of compressional and shear wave velocity are shown in Figure C.1a and C.1b, respectively. The shaded areas denote velocity dispersion and this is exactly proportional to attenuation. This is a special case of the more general Kramers-Kronig relations. Consequently, knowing the maximum attenuation of normal incident P -waves, one can calculate frequency-dependent qP - and qSV -wave attenuation as a function of incidence angle according to

$$\Delta_P(\theta) = \frac{v_{qP}^u(\theta) - v_{qP}^r(\theta)}{v_{qP}^u(\theta)}, \quad (\text{C.38})$$

$$\Delta_S(\theta) = \frac{v_{qSV}^u(\theta) - v_{qSV}^r(\theta)}{v_{qSV}^u(\theta)}, \quad (\text{C.39})$$

$$Q_{qP}^{-1}(\omega, \theta) = \frac{Q_{qP}^{-1}(\omega, 0^\circ)}{\Delta_P(0^\circ)} \Delta_P(\theta), \quad (\text{C.40})$$

$$Q_{qSV}^{-1}(\omega, \theta) = \frac{Q_{qP}^{-1}(\omega, 0^\circ)}{\Delta_P(0^\circ)} \Delta_S(\theta). \quad (\text{C.41})$$

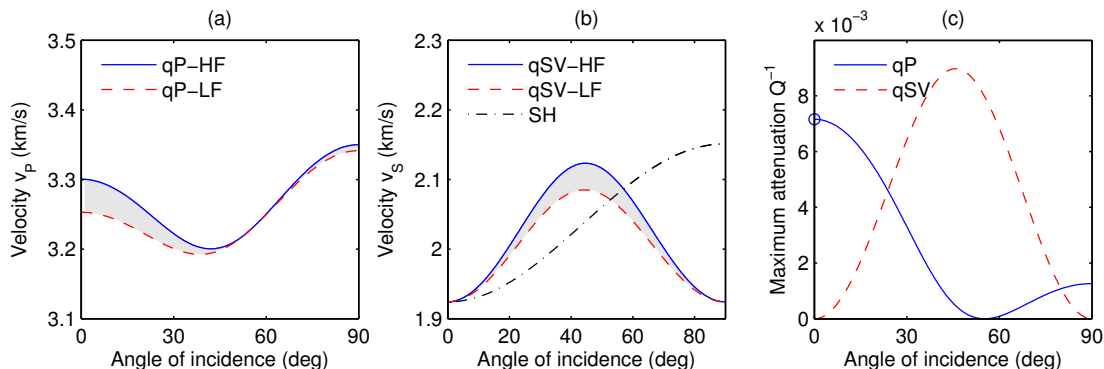


Figure C.1: Velocity limits derived obtained from Backus averaging and corresponding maximum attenuation. The medium consists of thin unconsolidated sanstone layers embedded within a consolidated sandstone, material parameters given in Table 5.1.

The maximum attenuation calculated such is shown in Figure C.1c with a small circle indicating the known reference attenuation $Q_{qP}^{-1}(0^\circ)$. The theoretical results are in perfect agreement with the attenuation estimates obtained from the numerical FE experiments shown in Figure 5.8a.

C.4 White's model for partial saturation

The model of (White, 1975) describes the effective elastic properties of a porous medium with partial gas saturation. The medium is considered as saturated by a liquid with spherical gas inclusions, such that the inner sphere radius a is smaller than radius of the outer shell b . The dry frame moduli are assumed isotropic and interaction between the different inclusions is excluded. Formulas incorporate a correction from Dutta and Seriff (1979) and are taken from Mavko et al. (1998). The effective P -wave modulus of partially saturated porous rock is given by

$$H_{\text{eff}}(\omega) = \frac{K_\infty}{1 - K_\infty W(\omega)} + \frac{4}{3} G, \quad (\text{C.42})$$

where K_∞ is the unrelaxed (high-frequency) limit of the bulk modulus, G is the rock shear modulus and the frequency-dependence is contained in the parameter W . Both parameters depend on the gas saturation

$$S = \frac{a^3}{b^3}. \quad (\text{C.43})$$

Denoting by K_d the bulk modulus of the drained rock frame, by K_g the grain bulk modulus, by K_f that of the fluid, as well as by K_1 and K_2 the undrained

bulk moduli of the gas- and water-saturated phases as obtained from Gassmann's equations, K_∞ is given by

$$K_\infty = \frac{K_2(3K_1 + 4G) + 4G(K_1 - K_2)S}{(3K_1 + 4G) - 3(K_1 - K_2)S}. \quad (\text{C.44})$$

The parameter W is calculated as

$$W = \frac{3a^2(R_1 - R_2)(-Q_1 + Q_2)}{b^3 i \omega (Z_1 + Z_2)}, \quad (\text{C.45})$$

$$R_1 = \frac{K_1 - K_d}{1 - K_d/K_g} \frac{3K_2 + 4G}{K_2(3K_1 + 4G) + 4G(K_1 - K_2)S}, \quad (\text{C.46})$$

$$R_2 = \frac{K_2 - K_d}{1 - K_d/K_g} \frac{3K_1 + 4G}{K_2(3K_1 + 4G) + 4G(K_1 - K_2)S}, \quad (\text{C.47})$$

$$Z_1 = \frac{\eta_1 a}{\kappa} \frac{1 - e^{-2\alpha_1 a}}{(\alpha_1 a - 1) + (\alpha_1 a + 1)e^{-2\alpha_1 a}}, \quad (\text{C.48})$$

$$Z_2 = \frac{\eta_2 a}{\kappa} \frac{(\alpha_2 b + 1) + (\alpha_2 b - 1)e^{2\alpha_2(b-a)}}{(\alpha_2 b + 1)(\alpha_2 a - 1) + (\alpha_2 b - 1)(\alpha_2 a + 1)e^{2\alpha_2(b-a)}}, \quad (\text{C.49})$$

$$\alpha_j = \sqrt{\frac{i \omega \eta_j}{\kappa K_{Ej}}}, \quad (\text{C.50})$$

$$K_{Ej} = \left[1 - \frac{K_{fj}(1 - K_j/K_g)(1 - K_d/K_g)}{\phi K_j(1 - K_{fj}/K_g)} \right] K_{Aj}, \quad (\text{C.51})$$

$$K_{Aj} = \left(\frac{\phi}{K_{fj}} + \frac{1 - \phi}{K_g} - \frac{K_d}{K_g^2} \right)^{-1}, \quad (\text{C.52})$$

$$Q_j = \frac{(1 - K_d/K_g)K_{Aj}}{K_j}. \quad (\text{C.53})$$

As in the whole thesis, ϕ , η and κ refer to porosity, viscosity and permeability, respectively.

For the same spherical geometry, Dutta and Odé (1979) give a rigorous solution for the effective bulk modulus by solving a boundary value problem based directly on the Biot equations. Both formulations, that of White as well as that of Dutta and Odé can be applied to calculate the effective bulk modulus of a partially saturated rock, from which velocity dispersion and attenuation of P -waves are derived.

C.5 Complement on the random fractal media model

The CRM model (Toms et al., 2007; Müller et al., 2008) has been elaborately presented in section 2.8.2. It is complemented here by a summary of the spectra of the von Kármán correlation 1-D, 2-D and 3-D media, a definition of the hypergeometric function and a figure showing the influence of the Hurst coefficient on the dispersion and attenuation signatures in porous media with random fractal saturation.

The von Kármán correlation function was already given in section 2.8 as

$$B^{\text{fractal}}(r) = \sigma_{MM}^2 \frac{2^{1-\nu}}{\Gamma(\nu)} \left(\frac{r}{a}\right)^\nu K_\nu\left(\frac{r}{a}\right), \quad (\text{C.54})$$

where Γ is the Gamma function and K_ν is the modified Bessel function of the second kind (Macdonald function). The parameter ν is called Hurst exponent. For $\nu = 1/2$, B^{fractal} is identical with the exponential correlation function. Its 3-D spectrum is given by

$$\Phi_{3D}^{\text{fractal}}(k) = \sigma_{MM}^2 \frac{a^3 \Gamma(\nu + 3/2)}{\pi^{3/2} \Gamma(\nu) (1 + k^2 a^2)^{\nu+3/2}} \quad (\text{C.55})$$

and for large values of ka the spectrum decays as $(ka)^{-2\nu+3}$. If $\nu = 1/3$, Φ^{fractal} is referred to as the Kolmogorov energy spectrum that describes turbulent flows (Pope, 2000). A distribution with $\nu = 0$ and $a \rightarrow \infty$ is called self-similar, since over the total wavenumber domain, the spectrum follows a power-law. Note that the right hand side of C.55 goes to infinity in this case, due to the pole of the Gamma function. This pole at argument zero can be removed, however, by rescaling Φ^{fractal} with the factor $1/2 \Gamma(\nu)$ (Klimeš, 2002). The 1-D and 2-D spectra of the von Kármán correlation function are given by (Sato and Fehler, 1998; Tittgemeyer, 1999)

$$\Phi_{1D}^{\text{fractal}}(k) = \sigma_{MM}^2 \frac{a \Gamma(\nu + 1/2)}{\sqrt{\pi} \Gamma(\nu) (1 + k^2 a^2)^{\nu+1/2}}, \quad (\text{C.56})$$

$$\Phi_{2D}^{\text{fractal}}(k) = \sigma_{MM}^2 \frac{a^2 \Gamma(\nu + 1)}{\pi \Gamma(\nu) (1 + k^2 a^2)^{\nu+1}}. \quad (\text{C.57})$$

According to Becken and Schmelcher (2000), the definition of the Gaussian hypergeometric function (GHF) is

$${}_2F_1([a, b], c, z) \equiv \sum_{n=0}^{\infty} \frac{(a, n)(b, n)}{(c, n)(1, n)} z^n, \quad (\text{C.58})$$

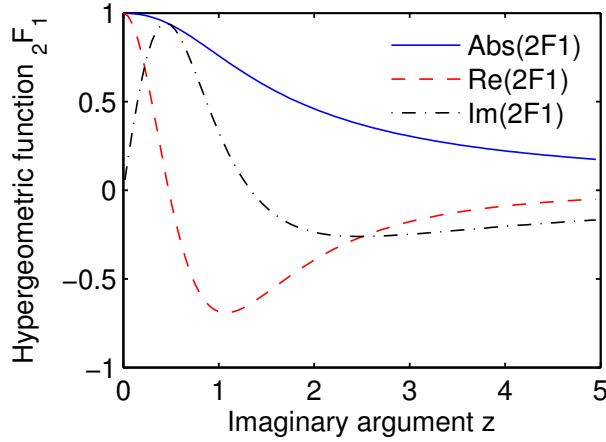


Figure C.2: Absolute values as well as real and imaginary parts of the Gaussian hypergeometric function ${}_2F_1(a, b; c; x)$. The values chosen are $a = 1$, $b = 1.8$, $c = 0.5$ and $x = \imath z$.

where (a, n) is the Pochhammer symbol defined using the Gamma function Γ by

$$(a, n) \equiv \frac{\Gamma(a + n)}{\Gamma(a)}. \quad (\text{C.59})$$

Note that the GHF has convergence radius 1 such that for $|z| \leq 1$ the sum in equation C.58 diverges. The domain of convergence can be extended to the whole complex plane except of two single points by analytic continuation (Becken and Schmelcher, 2000). A plot of the GHF for purely imaginary argument is shown in Figure C.2. The parameters chosen are $a = 1$, $b = 1.8$ and $c = 0.5$.

The functions ${}_2F_1$ and Φ^{fractal} are used to describe the effective behaviour of porous rocks with random partial saturation and a fractal distribution of the fluid phases. Examples of velocity dispersion and attenuation of such a medium are shown in Figure C.4 for varying Hurst exponent ν . Realisations and corresponding correlation functions are shown in Figure C.3. Material parameters are that of a consolidated sandstone with 50% gas and 50% water saturation, see Table 5.1 on page 70. The depicted solutions are for Hurst coefficients 0.9, 0.3 and 0.1. The velocity dispersion shown in Figure C.4a shows a transition from the low-frequency to the high-frequency limit that is the smoother the lower ν is. The smoother velocity dispersion corresponds to a broader peak in the attenuation behaviour as shown in Figure C.4b. In particular, the high-frequency content of the attenuation spectrum is stronger for smaller ν . Analysing the asymptotic scaling of attenuation reveals that at high frequencies

$$Q^{-1} \propto \omega^{-\nu}, \quad (\text{C.60})$$

i. e. the slope of the high-frequency asymptote is the steeper the higher the Hurst exponent ν is. This result is consistent with the observation made by Pride and Masson (2006) using numerical simulation.

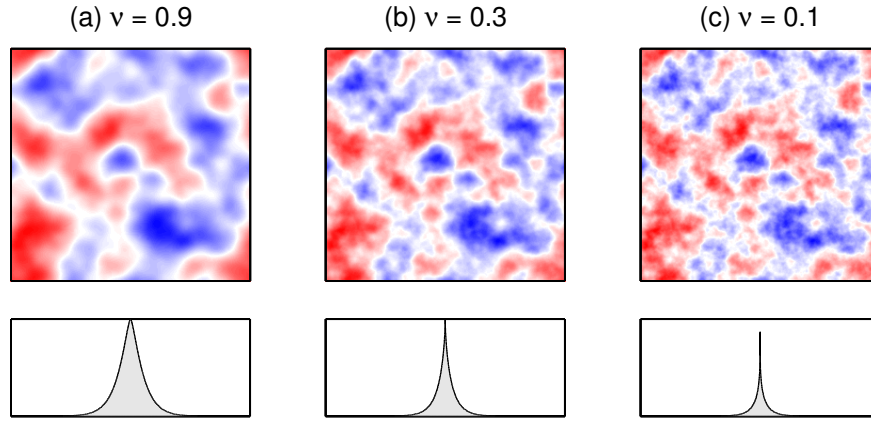


Figure C.3: Fractal CRM realisations and corresponding correlation function for Hurst exponents varying between 0.1 and 0.9.

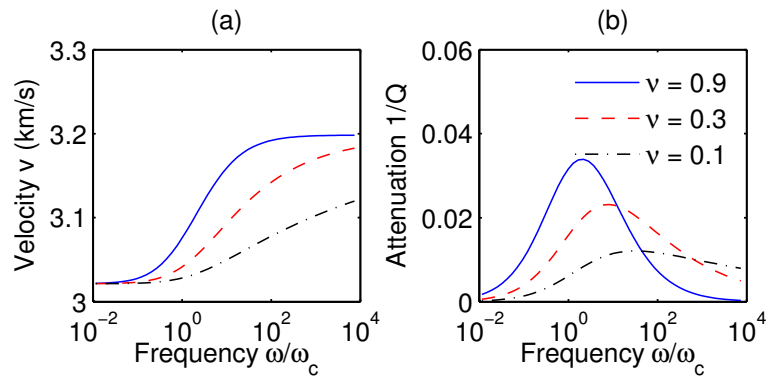


Figure C.4: CRM model for partial saturation with fractal pore fluid distribution. Velocity dispersion and attenuation are given as a function of frequency for three models with different Hurst exponents.

Appendix D

Abaqus porous elastic model

In section 3.2, the finite-element (FE) method for the solution of elastic and poroelastic problems was briefly introduced. This is the basis of the commercial Abaqus package that among other things allows to solve the quasistatic Biot equations in complex 3-D domains (Abaqus, Inc., 1998). Here some properties of the Abaqus “porous elastic” model are presented, focussing not on the technical implementation but on the particularities of the user interface.

First of all, the poroelastic implementation is based on a non-linear rheology. A linear material behaviour is therefore only obtained for small strains. In the small-strain limit, the non-linear models parameters can be converted into their linear asymptotes by neglecting higher-order terms of the constitutive relations. This is shown subsequently.

Instead of the porosity ϕ , the void ratio e is used. It is defined as the ratio of pore volume to solid volume

$$e = \frac{V_\phi}{V - V_\phi} = \frac{\phi}{1 - \phi} \quad \Leftrightarrow \quad \phi = \frac{e}{1 + e}. \quad (\text{D.1})$$

During compression, the void ratio decreases. This behaviour is expressed by the logarithmic bulk modulus

$$\kappa = -\frac{de}{d[\ln(p_s + p_t)]}, \quad (\text{D.2})$$

where $p_s = \sigma_{ii}/3$ is the confining pressure and its lower limit is referred to as tensile strength p_t . Note that the Abaqus model is parameterised with the effective stress

$$\sigma_{ij} = \tau_{ij} + p, \quad (\text{D.3})$$

such that in order to obtain the total stress τ_{ij} the pore pressure p has to be subtracted (The plus sign arises from different sign conventions). From equation

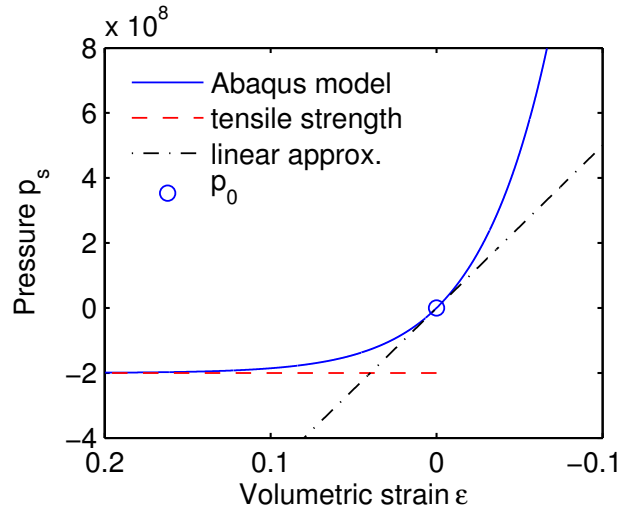


Figure D.1: Stress-strain relation of the Abaqus FE model. Confining pressure is given as a function of volumetric strain. The non-linear behaviour D.4 can be approximated by the linear expansion around zero, as expressed by equation D.5.

D.2, the constitutive relation for isotropic deformation is derived as

$$p_s = -p_t + (p_0 + p_t) \exp \left[\frac{1 + e_0}{\kappa} (1 - \exp \varepsilon) \right], \quad (\text{D.4})$$

where e_0 and p_0 are the initial void ratio and confining pressure, respectively, and ε is the total volumetric strain. This relation is depicted in Figure D.1.

By setting the initial pressure to zero and by using the Taylor expansion for the exponential function $\exp x \approx 1 + x + \mathcal{O}(x^2)$ the relation simplifies to

$$p_s \approx -\frac{p_t(1 + e_0)}{\kappa} \varepsilon = -K_d \varepsilon. \quad (\text{D.5})$$

The proportionality coefficient is easily identified with the linear bulk modulus of the drained rock K_d that describes the linear material behaviour at small strains. Again, note the sign convention for the confining pressure. If one wants to model a particular value of K_d , then the tensile strength p_t and the logarithmic bulk modulus must be chosen such that

$$\kappa = \frac{p_t(1 + e_0)}{K_d}. \quad (\text{D.6})$$

A further difference between the notation used in this thesis and the Abaqus model is the parameterisation of Darcy's law. This is expressed in terms of the piezometric head

$$\phi \equiv z + \frac{p}{g\rho^f}, \quad (\text{D.7})$$

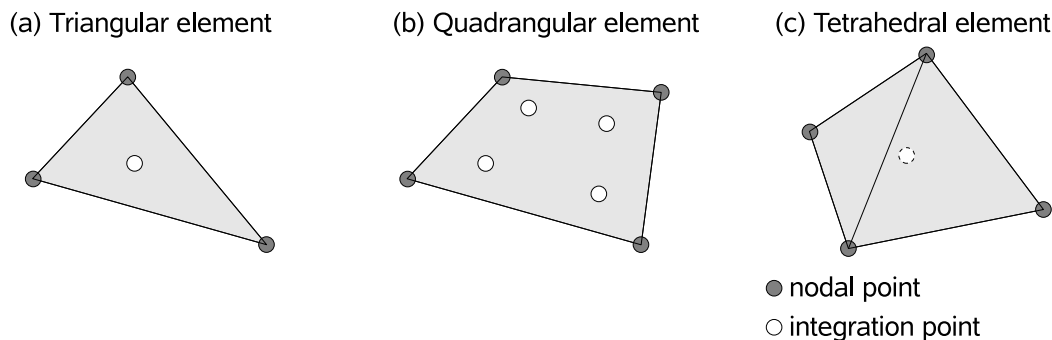


Figure D.2: Triangular, quadrangular and tetrahedral linear elements. While 3-node-triangular and 4-node-tetrahedral elements use only one integration point, the 4-node-quadrangular elements use 4.

where z is vertical position, p is pore pressure, g is gravitational acceleration and ρ^f is fluid density. According to Darcy's law the filtration velocity q_i is then given by

$$\dot{w}_i = -k \partial_i \phi. \quad (\text{D.8})$$

Comparing equations 2.70 and D.8 and neglecting the potential part z in the piezometric head, the fluid conductivity k (units of m/s) and the friction coefficient b (units of Pa s/m²) are related as

$$\frac{1}{b} = \frac{\kappa}{\eta} = \frac{k}{g\rho^f}. \quad (\text{D.9})$$

As in the previous sections, hydraulic permeability is denoted by κ and should not be confused with the logarithmic bulk modulus, η is the dynamic fluid viscosity. Fluid flow, as implemented in the Abaqus package may be modelled as anisotropic and pressure-dependent which is beyond the scope of this work. These features, however, deserve consideration in the future, in particular in the context of non-linear fluid-induced seismicity (Hummel, 2008).

Finally, the output of Abaqus field variables are by default given at different positions. Stresses are usually stored at the integration points, while displacements and pore pressure are stored on the grid nodes, as depicted in Figure D.2. In order to perform an averaging of the stress and pressure fields as required in the quasistatic experiments (see section 5.2), it is therefore necessary to interpolate the stresses to the nodal values during the postprocessing step.

Bibliography

- Abaqus, Inc. (1998). *ABAQUS User's Manual*. Abaqus, Inc.
- Aki, K. and Richards, P. (1980). *Quantitative Seismology: Theory and Methods*. WH Freeman.
- Aldridge, D. F., Bartel, L. C., and Symons, N. P. (2004). Velocity-stress-pressure algorithm for 3D poroelastic wave propagation. In *SEG Technical Program Expanded Abstracts*, pages 1917–1920.
- Attenborough, K. (1982). Acoustical characteristics of porous materials. *Physics Reports*, 82(3):179–227.
- Auld, B. A. (1990). *Acoustic fields and waves in solids*, volume 1&2. Robert E. Krieger Publishing Co., Malabar, Florida, 2nd edition.
- Backus, G. E. (1962). Long-wave elastic anisotropy produced by horizontal layering. *Journal of Geophysical Research*, 67(11):4427–4440.
- Batzle, M. and Wang, Z. (1992). Seismic properties of pore fluids. *Geophysics*, 57(11):1396–1408.
- Becken, W. and Schmelcher, P. (2000). The analytic continuation of the Gaussian hypergeometric function ${}_2F_1(a, b; c; z)$ for arbitrary parameters. *Journal of Computational and Applied Mathematics*, 126(1-2):449–478.
- Berryman, J. G. (2007). Seismic waves in rocks with fluids and fractures. *Geophysical Journal International*, 171:954–974.
- Berryman, J. G. and Milton, G. W. (1991). Exact results for generalized Gassmann's equations in composite porous media with two constituents. *Geophysics*, 56(12):1950–1960.
- Biot, M. A. (1941). General theory of three-dimensional consolidation. *Journal of Applied Physics*, 12:155–164.

- Biot, M. A. (1956a). Theory of propagation of elastic waves in a fluid-saturated porous solid. I. Low frequency range. *Journal of the Acoustical Society of America*, 28(2):168–178.
- Biot, M. A. (1956b). Theory of propagation of elastic waves in a fluid-saturated porous solid. II. Higher frequency range. *Journal of the Acoustical Society of America*, 28(2):179–191.
- Biot, M. A. (1962). Mechanics of deformation and acoustic propagation in porous media. *Journal of Applied Physics*, 33(4):1482–1498.
- Biot, M. A. and Willis, D. G. (1957). The elastic coefficients of the theory of consolidation. *Journal of Applied Mechanics*, 24(4):594–601.
- Bohlen, T. (2002). Parallel 3-D viscoelastic finite difference seismic modelling. *Computers & Geosciences*, 28:887–899.
- Boore, D. M. (1972). Finite difference methods for seismic wave propagation in heterogeneous materials. *Methods in Computational Physics*, 11:1–37.
- Bourbié, T., Coussy, O., and Zinssner, B. (1987). *Acoustics of Porous Media*. Éditions Technip, Paris.
- Brajanovski, M., Gurevich, B., and Schoenberg, M. (2005). A model for P-wave attenuation and dispersion in a porous medium permeated by aligned fractures. *Geophysical Journal International*, 163:372–384.
- Brajanovski, M., Müller, T. M., and Gurevich, B. (2006). Characteristic frequencies of seismic attenuation due to wave-induced fluid flow in fractured porous media. *Geophysical Journal International*, 166:574–578.
- Brown, R. J. S. and Korrington, J. (1975). On the dependence of the elastic properties of a porous rock on the compressibility of the pore fluid. *Geophysics*, 40(4):608–616.
- Burrige, R. and Keller, J. B. (1981). Poroelasticity equations derived from microstructure. *Journal of the Acoustical Society of America*, 70(4):1140–1046.
- Cadoret, T., Marion, D., and Zinszner, B. (1995). Influence of frequency and fluid distribution on elastic wave velocities in partially saturated limestones. *Journal of Geophysical Research*, 100(B6):9789–9803.
- Carcione, J. M. (2001). *Wave Fields in Real Media*. Pergamon, New York.

- Carcione, J. M., Helle, H. B., and Pham, N. H. (2003). White's model for wave propagation in partially saturated rocks: Comparison with poroelastic numerical experiments. *Geophysics*, 68:1389–1398.
- Carcione, J. M. and Quiroga-Goode, G. (1995). Some aspects of the physics and numerical modeling of Biot compressional waves. *Journal of Computational Acoustics*, 4:261–280.
- Cohen, G. C. (2002). *Higher-Order Numerical Methods for Transient Wave Equations*. Springer, Berlin, Heidelberg, New York.
- Coussy, O. (1991). *Mécanique des milieux poreux*. Éditions Technip, Paris.
- Dai, N., Vafidis, A., and Kanasewich, E. R. (1995). Wave propagation in heterogeneous, porous media: A velocity-stress, finite-difference method. *Geophysics*, 60(2):327–340.
- de Beer, F. C., Middleton, M. F., and Hilson, J. (2004). Neutron radiography of porous rocks and iron ore. *Applied Radiation and Isotopes*, 61(4):487–495.
- Deresiewicz, H. and Skalak, R. (1963). On uniqueness in dynamic poroelasticity. *Bulletin of the Seismological Society of America*, 53(4):783–788.
- Dewar, J. and Pickford, S. (2001). Rock physics for the rest of us: An informal discussion. *CSEG Recorder*, 26(5):42–49.
- Dutta, N. C. and Odé, H. (1979). Attenuation and dispersion of compressional waves in fluid-filled porous rocks with partial gas saturation (White model)—Part I: Biot theory. *Geophysics*, 44(11):1777–1788.
- Dutta, N. C. and Odé, H. (1983). Seismic reflections from a gas-water contact. *Geophysics*, 48(2):148–162.
- Dutta, N. C. and Sheriff, A. J. (1979). On White's model of attenuation in rocks with partial gas saturation. *Geophysics*, 44(11):1806–1812.
- Dvorkin, J., Mavko, G., and Nur, A. M. (1995). Squirt flow in fully saturated rocks. *Geophysics*, 60(1):97–107.
- Feder, J. (1988). *Fractals*. Plenum Press, New York.
- Galvin, R. J. and Gurevich, B. (2006). Interaction of an elastic wave with a circular crack in a fluid-saturated porous medium. *Applied Physics Letters*, 88:061918.

- Gassmann, F. (1951). Über die Elastizität poröser Medien. *Vierteljahrsschrift der Naturforschenden Gesellschaft in Zürich*, 96:1–23.
- Gelinsky, S. and Shapiro, S. A. (1997). Poroelastic backus averaging for anisotropic layered fluid- and gas-saturated sediments. *Geophysics*, 62:1867–1878.
- Gelinsky, S., Shapiro, S. A., Müller, T. M., and Gurevich, B. (1998). Dynamic poroelasticity of thinly layered structures. *International Journal of Solids and Structures*, 35:4739–4752.
- Gradshteyn, I. S. and Ryzhik, J. M. (1983). *Table of Integrals, Series and Products*. Academic Press, London.
- Guéguen, Y. and Palciauskas, V. (1994). *Introduction to the Physics of Rocks*. Princeton University Press.
- Gurevich, B. (1996). On: “Wave propagation in heterogeneous, porous media: A velocity-stress, finite difference method,” by N. Dai, A. Vafidis, and E. R. Kanasewich (March-April 1995 *Geophysics*, pp. 327–340). *Geophysics*, 61(4):1230–1232.
- Gurevich, B., Ciz, R., and Dennemann, A. I. M. (2004). Simple expressions for normal-incidence reflection coefficients from an interface between fluid-saturated porous materials. *Geophysics*, 69(6):1372–1377.
- Gurevich, B., Galvin, R. J., Brajanovski, M., Müller, T. M., and Lambert, G. (2007). Fluid substitution, dispersion and attenuation in fractured and porous reservoirs – insights from new rock physics models. *The Leading Edge*, 26:1162–1168.
- Gurevich, B. and Lopatnikov, S. L. (1995). Velocity and attenuation of elastic waves in finely layered porous rocks. *Geophysical Journal International*, 121:933–947.
- Hassanzadeh, S. (1991). Acoustic modeling in fluid-saturated porous media. *Geophysics*, 56(4):424–435.
- Helle, H. B., Pham, N. H., and Carcione, J. M. (2003). Velocity and attenuation in partially saturated rocks: poroelastic numerical experiments. *Geophysical Prospecting*, 51:551–566.
- Hill, R. (1963). Elastic properties of reinforced solids: Some theoretical principles. *Journal of the Mechanics and Physics of Solids*, 11(5):357–372.

- Hummel, N. (2008). Fluid induced microseismicity in non-linear porous media. Master's thesis, Geophysikalisches Institut, Karlsruhe, Germany.
- Ishimaru, A. (1978). *Wave propagation and scattering in random media*. Academic Press, New York.
- Jianfeng, Z. (1999). Quadrangle-grid velocity-stress finite-difference method for poroelastic wave equations. *Geophysical Journal International*, 139:171–182.
- Johnson, D. L. (2001). Theory of frequency dependent acoustics in patchy-saturated porous media. *Journal of the Acoustical Society of America*, 110:682–694.
- Johnson, D. L., Koplik, J., and Dashen, R. (1987). Theory of dynamic permeability and tortuosity in fluid-saturated porous media. *Journal of Fluid Mechanics*, 176:379–402.
- Johnson, P. A., Zinszner, B., and Rasolofosaon, P. N. J. (1996). Resonance and elastic nonlinear phenomena in rock. *Journal of geophysical research*, 101(B5):11553–11564.
- Karpfinger, F. (2006). Green's functions and seismic wave radiation in poroelastic continua. Master's thesis, Freie Universität Berlin, Berlin.
- Klimeš, L. (2002). Correlation functions of random media. *Pure and Applied Geophysics*, 159(7):1811–1831.
- Klobes, P., Riesemeier, H., Meyer, K., Goebbels, J., and Hellmuth, K. (1997). Rock porosity determination by combination of X-ray computerized tomography with mercury porosimetry. *Fresenius' Journal of Analytical Chemistry*, 357(5):543–547.
- Lebedev, M., Toms-Stewart, J., Clennell, B., Pervukhina, M., Shulakova, V., Paterson, L., Müller, T. M., Gurevich, B., and Wenzlau, F. (2009). Direct laboratory observation of patchy saturation and its effects on ultrasonic velocities. *The Leading Edge*, 28(1).
- Levander, A. R. (1988). Fourth-order finite-difference PS-V seismograms. *Geophysics*, 53(11):1425–1436.
- Lévy, T. (1979). Propagation of waves in a fluid-saturated porous elastic solid. *International Journal of Engineering Science*, 17(9):1005–1014.
- Masson, Y. J. and Pride, S. R. (2007). Poroelastic finite difference modeling of seismic attenuation and dispersion due to mesoscopic-scale heterogeneity. *Journal of Geophysical Research*, 112:B03204.

- Masson, Y. J., Pride, S. R., and Nihei, K. T. (2006). Finite difference modeling of Biot's poroelastic equations at seismic frequencies. *Journal of Geophysical Research*, 111:B10305.
- Mavko, G. and Jizba, D. (1991). Estimating grain-scale fluid effects on velocity dispersion in rocks. *Geophysics*, 56(12):1940–1949.
- Mavko, G., Mukerji, T., and Dvorkin, J. (1998). *The Rock Physics Handbook: Tools for Seismic Analysis of Porous Media*. Cambridge University Press.
- Monsen, K. and Johnstad, S. E. (2005). Improved understanding of velocity-saturation relationships using 4D computer-tomography acoustic measurements. *Geophysical Prospecting*, 53(2):173–181.
- Müller, T. M. and Gurevich, B. (2004). One-dimensional random patchy saturation model for velocity and attenuation in porous rocks. *Geophysics*, 69(5):1166–1172.
- Müller, T. M. and Gurevich, B. (2005a). A first-order statistical smoothing approximation for the coherent wave field in random porous media. *Journal of the Acoustical Society of America*, 117(4):1796–1805.
- Müller, T. M. and Gurevich, B. (2005b). Wave-induced fluid flow in random porous media: Attenuation and dispersion of elastic waves. *Journal of the Acoustical Society of America*, 117(5):2732–2741.
- Müller, T. M. and Shapiro, S. A. (2001). Most probable seismic pulses in single realizations of 2-D and 3-D random media. *Geophysical Journal International*, 144:83–95.
- Müller, T. M. and Shapiro, S. A. (2004). Scattering attenuation in randomly layered structures with finite lateral extent: A hybrid Q model. *Geophysics*, 69:1530–1534.
- Müller, T. M., Toms-Stewart, J., and Wenzlau, F. (2008). Velocity-saturation relation for partially saturated rocks with fractal pore fluid distribution. *Geophysical Research Letters*, 35:L09306.
- Murphy, W. F. (1982). Effects of partial water saturation on attenuation in massilon sandstone and vycor porous glass. *Journal of the Acoustical Society of America*, 71:1458–1468.
- Norris, A. N. (1985). Radiation from a point source and scattering theory in a fluid-saturated porous solid. *Journal of the Acoustical Society of America*, 77:2012–2023.

- Norris, A. N. (1992). On the correspondence between poroelasticity and thermoelasticity. *Journal of Applied Physics*, 71(3):1138–1141.
- Norris, A. N. (1993). Low-frequency dispersion and attenuation in partially saturated rocks. *Journal of the Acoustical Society of America*, 94:359–370.
- O’Doherty, R. F. and Anstey, N. A. (1971). Reflections on amplitudes. *Geophysical Prospecting*, 19:430–458.
- Picotti, S., Carcione, J. M., Rubino, J. G., and Santos, J. E. (2007). P-wave seismic attenuation by slow-wave diffusion: Numerical experiments in partially saturated rocks. *Geophysics*, 72:N11–N21.
- Plona, T. J. (1980). Observation of a second bulk compressional wave in a porous medium at ultrasonic frequencies. *Applied Physics Letters*, 36(4):259–261.
- Pope, S. B. (2000). *Turbulent Flows*. Cambridge University Press.
- Pride, S. R., Gangi, A. F., and Dale Morgan, F. (1992). Deriving the equations of motion for porous isotropic media. *Journal of the Acoustical Society of America*, 92(6).
- Pride, S. R., Harris, J. M., Johnson, D. L., Mateeva, A., Nihel, K. T., Nowack, R. L., Rector, J. W., Spetzler, H., Wu, R., Yamamoto, T., Berryman, J. G., and Fehler, M. (2003). Acquisition/Processing—Permeability dependence of seismic amplitudes. *The Leading Edge*, 22:518–525.
- Pride, S. R. and Masson, Y. J. (2006). Acoustic attenuation in self-affine porous structures. *Physical Review Letters*, 97(18):184301.
- Quiroga-Goode, G. and Carcione, J. M. (1997). Heterogeneous modelling behaviour at an interface in porous media. *Computational Geosciences*, 1(2):109–125.
- Reiner, M. (1964). The Deborah number. *Physics Today*, 17(1):62.
- Rubino, J. G., Santos, J. E., Picotti, S., and Carcione, J. M. (2007). Simulation of upscaling effects due to wave-induced fluid flow in Biot media using the finite-element method. *Journal of Applied Geophysics*, 62(3):193–203.
- Rudnicki, J. W. (1986). Fluid mass sources and point forces in linear elastic diffusive solids. *Mechanics of Materials*, 5:383–393.
- Rytov, S., Kravcov, J., and Tatarskij, V. (1989). *Principles of statistical radiophysics, vol. IV: Wave propagation through random media*. Springer, New York.

- Saenger, E. H., Ciz, R., Krüger, O. S., Schmalholz, S. M., Gurevich, B., and Shapiro, S. A. (2007). Finite-difference modeling of wave propagation on microscale: A snapshot of the work in progress. *Geophysics*, 72(5):SM293–SM300.
- Saenger, E. H., Gold, N., and Shapiro, S. A. (2000). Modeling the propagation of elastic waves using a modified finite-difference grid. *Wave Motion*, 31:77–92.
- Sams, M. S., Neep, J. P., Worthington, M. H., and King, M. S. (1997). The measurement of velocity dispersion and frequency-dependent intrinsic attenuation in sedimentary rocks. *Geophysics*, 62(5):1456–1464.
- Samuelides, Y. (1998). Velocity shift using the Rytov approximation. *Journal of the Acoustical Society of America*, 104(5):2596–2603.
- Sato, H. and Fehler, M. (1998). *Seismic Wave Propagation and Scattering in the Heterogeneous Earth*. Springer, New York.
- Shapiro, S. A. and Hubral, P. (1999). *Elastic Waves in Random Media*. Springer, Heidelberg.
- Sheen, D.-H., Tuncay, K., Baag, C.-E., and Ortoleva, P. J. (2006). Parallel implementation of a velocity-stress staggered-grid finite-differences method for 2-D poroelastic wave propagation. *Computers & Geosciences*, 32:1182–1191.
- Smith, W. D. (1975). The application of finite element analysis to body wave propagation problems. *Geophysical Journal International*, 42(2):747–768.
- Terzaghi, K. and Fröhlich, O. K. (1936). *Theorie der Setzung von Tonschichten*. Deuticke, Leipzig, Wien.
- Thomsen, L. (1986). Weak elastic anisotropy. *Geophysics*, 51(10):1954–1966.
- Tittgemeyer, M. (1999). *Streuung elastischer Wellen im oberen Erdmantel*. Logos, Berlin.
- Toms, J., Müller, T. M., Ciz, R., and Gurevich, B. (2006). Comparative review of theoretical models for elastic wave attenuation and dispersion in partially saturated rocks. 26(6-7):548–565.
- Toms, J., Müller, T. M., and Gurevich, B. (2007). Seismic attenuation in porous rocks with random patchy saturation. *Geophysical Prospecting*, 55:671–678.
- Uscinski, B. J. (1977). *The elements of wave propagation in random media*. McGraw-Hill, London.

- Virieux, J. (1986). P-SV wave propagation in heterogeneous media: Velocity-stress finite-difference method. *Geophysics*, 51(4):889–901.
- Wang, H. F. (2000). *Theory of Linear Poroelasticity with Applications to Geomechanics and Hydrogeology*. Princeton University Press.
- Wang, H. F. and Anderson, M. P. (1982). *Introduction to Groundwater Modeling—Finite Element and Finite Difference Methods*. Academic Press, New York.
- Wenzlau, F., Altmann, J. B., and Müller, T. M. (2008). Estimating effective elastic properties of heterogeneous porous media using time-domain finite element modelling. In *Symposium on the Acoustics of Poro-Elastic Materials, December 17-18-19, 2008, Bradford (UK)*.
- Wenzlau, F. and Müller, T. M. (2008). Finite-difference modeling of wave propagation and diffusion in poroelastic media. *submitted to Geophysics*.
- Wenzlau, F., Xia, T., and Müller, T. M. (2007). Modeling elastic and poroelastic wave propagation in complex geological structures. In *High Performance Computing in Science and Engineering '07*, pages 587–601, Heidelberg. Springer.
- White, J. E. (1975). Computed seismic speeds and attenuation in rocks with partial gas saturation. *Geophysics*, 40:224–232.
- White, J. E., Mikhaylova, N. G., and Lyakhovitskiy, F. M. (1975). Low-frequency seismic waves in fluid saturated layered rocks. *Physics of the Solid Earth*, 11:654–659.
- Wood, A. B. (1955). *A textbook of sound*. The MacMillan Co., New York, 3rd revised edition.
- Wu, R.-S. and Aki, K. (1988). Introduction: Seismic wave scattering in three-dimensionally heterogeneous earth. *Pure and Applied Geophysics*, 128(1):1–6.
- Zhu, X. and McMechan, G. A. (1991). Numerical simulation of seismic responses of poroelastic reservoirs using Biot theory. *Geophysics*, 56(3):328–339.
- Zienkiewicz, O. C. (1977). *The Finite Element Method*. McGraw-Hill, London, 3., expanded and rev. ed. edition.

Author index

- Abaqus, Inc. (1998), 54, 56, 123
Aki and Richards (1980), 7, 48, 73, 105
Aldridge et al. (2004), 42
Attenborough (1982), 15
Auld (1990), 32
Backus (1962), 31, 114
Batzle and Wang (1992), 26
Becken and Schmelcher (2000), 120, 121
Berryman and Milton (1991), 31
Berryman (2007), 70
Biot and Willis (1957), 21
Biot (1941), 4, 15
Biot (1956a), 1, 4, 5, 15, 19
Biot (1956b), 4, 18, 113
Biot (1962), 18
Bohlen (2002), 41, 46, 49, 83
Boore (1972), 41
Bourbié et al. (1987), 2, 10, 15, 39, 64
Brajanovski et al. (2005), 34, 77
Brajanovski et al. (2006), 70, 79, 117
Brown and Korranga (1975), 21, 31
Burrige and Keller (1981), 15
Cadoret et al. (1995), 11
Carcione and Quiroga-Goode (1995), 42, 51, 68
Carcione et al. (2003), 13, 72
Carcione (2001), 15, 18, 20, 39, 76
Cohen (2002), 41, 83
Coussy (1991), 15
Dai et al. (1995), 12, 42
Deresiewicz and Skalak (1963), 25
Dewar and Pickford (2001), 1
Dutta and Odé (1979), 34, 41, 119
Dutta and Odé (1983), 25, 62, 63, 65
Dutta and Seriff (1979), 118
Dvorkin et al. (1995), 6
Feder (1988), 37
Galvin and Gurevich (2006), 34, 77
Gassmann (1951), 4, 15, 21, 31
Gelinsky and Shapiro (1997), 31, 79, 114, 117
Gelinsky et al. (1998), 34
Gradshteyn and Ryzhik (1983), 38
Gurevich and Lopatnikov (1995), 34, 35, 117
Gurevich et al. (2004), 25
Gurevich et al. (2007), 70
Gurevich (1996), 12, 42
Guéguen and Palciauskas (1994), 2
Hassanzadeh (1991), 42
Helle et al. (2003), 13
Hill (1963), 30
Hummel (2008), 125
Ishimaru (1978), 110
Jianfeng (1999), 12
Johnson et al. (1987), 18
Johnson et al. (1996), 39
Johnson (2001), 34
Karpfinger (2006), 29, 39
Klimeš (2002), 120
Klobes et al. (1997), 11
Lebedev et al. (2009), 12, 13, 70, 96
Levander (1988), 46

- Lévy (1979), 15
Masson and Pride (2007), 13, 42, 73, 94
Masson et al. (2006), 50, 51
Mavko and Jizba (1991), 6, 38
Mavko et al. (1998), 7, 8, 34, 108, 113, 116, 118
Monsen and Johnstad (2005), 11
Murphy (1982), 9, 11
Müller and Gurevich (2004), 34, 36
Müller and Gurevich (2005a), 34, 35
Müller and Gurevich (2005b), 6, 33, 35
Müller and Shapiro (2001), 9, 82, 83
Müller and Shapiro (2004), 81, 82
Müller et al. (2008), 12, 34, 36, 38, 94, 95, 120
Norris (1985), 59–61
Norris (1992), 5
Norris (1993), 30, 33, 34, 77, 79
O’Doherty and Anstey (1971), 8
Picotti et al. (2007), 13
Plona (1980), 9, 10
Pope (2000), 120
Pride and Masson (2006), 121
Pride et al. (1992), 15
Pride et al. (2003), 5, 6
Quiroga-Goode and Carcione (1997), 65
Reiner (1964), 52
Rubino et al. (2007), 73
Rudnicki (1986), 27
Rytov et al. (1989), 110
Saenger et al. (2000), 13, 46, 48, 58
Saenger et al. (2007), 103
Sams et al. (1997), 5
Samuelides (1998), 95
Sato and Fehler (1998), 8, 37, 110, 120
Shapiro and Hubral (1999), 9, 82
Sheen et al. (2006), 42
Smith (1975), 41
Terzaghi and Fröhlich (1936), 4, 15
Thomsen (1986), 116
Tittgemeyer (1999), 120
Toms et al. (2006), 35
Toms et al. (2007), 34, 38, 120
Uscinski (1977), 110
Virieux (1986), 41, 42, 46
Wang and Anderson (1982), 53
Wang (2000), 26, 27, 53, 56
Wenzlau and Müller (2008), 42, 70
Wenzlau et al. (2007), 42, 70
Wenzlau et al. (2008), 70
White et al. (1975), 33, 34, 72, 74
White (1975), 34, 118, 119
Wood (1955), 30
Wu and Aki (1988), 8
Zhu and McMechan (1991), 12, 42
Zienkiewicz (1977), 53, 55
de Beer et al. (2004), 11

Subject Index

- Abaqus package, 42, 123
- attenuation, 4–7
 - apparent, 7, 82
 - due to induced flow, 33
 - in layered media, 117
 - intrinsic, 4
- attenuation coefficient, 108
- backscattering, 82, 88
- Backus average, 31, 114
- Biot global flow, 5
- Biot theory, 18
 - assumptions, 18
 - boundary conditions, 24
 - constitutive relations, 19
 - critical frequency, 19
 - momentum equations, 18
 - quasistatic approximation, 28
 - wave equations, 22
- boundary conditions, 24, 48, 56
- causality, 105
- conjugate gradient method, 57
- convolution theorem, 105
- correlation function, 37, 81, 110, 120
- correlation length, 37, 110
- CT imaging, 11, 97
- Darcy's law, 26, 124, 125
- diffraction, 82, 88
- diffusion equation, 27
- diffusion length, 30
- diffusivity, 27
- digital core technology, 12
- Dirac distribution, 17, 27
- dispersion relation, 23, 28
 - diffusion wave, 28
- domain decomposition, 52
- double porosity, 29, 98
 - experiments, 76
- dynamic permeability, 18
- effective fluid density, 19
- effective fluid model, 30
- effective medium, 8, 29, 31
- effective stress coefficient, 20
- elasticity tensor, 20, 75
- exponential correlation function, 36
- fast path effect, 95
- finite-difference method, 41–45, 47
 - coefficients, 46
 - operator, 44, 45, 47
- finite-element method, 41, 53–55
 - basis functions, 55
- Fourier transform, 17
- fractal saturation, 120
- friction coefficient, 19, 26
- Gassmann equations, 21, 31
- Gassmann-Hill bound, 30
- Gassmann-Wood bound, 30
- Gaussian correlation function, 36, 110
- global flow, 5
- Heaviside step function, 17, 27, 105
- Helmholtz theorem, 22
- Hill's theorem, 30, 74

- homogenisation theory, 15
Hurst exponent, 37, 120
hypergeometric function, 121
increment of fluid content, 18
initial conditions, 24
Kramers-Kronig relations, 108, 117
Kronecker symbol, 17
Lamé parameters, 20, 115
Levi-Civita-symbol, 17
local flow, 6
logarithmic wavefield amplitude, 81
mesoscale, 3, 6, 33
method of statistical smoothing, 35
numerical dispersion, 60, 67
numerical stiffness, 51, 98
parallelisation, 52
partial saturation, 9, 29, 30
permeability, 3
pore space modulus, 20
poroelastic moduli, 20
porosity, 3
principle of limited memory, 105
principle of virtual work, 54
quality factor, 24, 81, 106
quasistatic approximation, 28
random medium, 35, 81, 88
relaxation experiment, 73, 75
relaxation function, 73, 105, 117
relaxation tensor, 76, 117
relaxed modulus, 73, 106
representative elementary volume, 73, 77, 109
resonance, 89
Ritz ansatz, 55
rock physics, 1
Rytov transformation, 82
scalability, 53
scattering, 7–9, 69–72, 81, 82, 99
scattering coefficient, 81
self-similarity, 120
slow P -wave, 9, 15
soft porosity, 6
source distribution, 48, 89
spectral ratio method, 73, 91
squirt flow, 6
staggered grid, 45, 58
 rotated, 46
 standard, 46
stiffness, 42
stiffness tensor, 77
tensor notation, 16
Thomsen parameters, 116
tortuosity, 3, 19
unrelaxed modulus, 73, 106
upscaling, 3
velocity-saturation relation, 96
velocity-stress formulation, 42
vertical transverse isotropy, 75
viscodynamic operator, 18, 113
von Kármán correlation function, 36, 120
wave equation
 acoustic, 65
 elastic, 28
 poroelastic, 22
 stochastic, 81
 viscoacoustic, 108
wave-induced fluid flow, 6, 32, 33, 88
 critical frequency, 31
 CRM model, 35, 121
 White's model, 33, 118